Spectrometer-Related Hyperion Papers included in the 2013 IEEE/JSTARS EO-1 Special Issue

Stephen G. Ungar
Senior Research Scientist
Biospheric Sciences Laboratory
NASA GSFC/**USRA-GESTAR**

David R. Landis
EO-1 Mission Analyst
Biospheric Sciences Laboratory
NASA GSFC/**Sigma Space Inc.**

HyspIRI Symposium, Pasadena, CA
October 15, 2013

Earth Observing-1 (EO-1) Mission

Mission Scientist, Dr. Elizabeth Middleton (NASA/GSFC Code 618)
Mission Manager, Mr. Daniel Mandl (NASA/GSFC Code 581)

EO-1 was designed to flight validate technologies and operational approaches applicable to future Earth observing missions. Launched on November 21, 2000, it is currently in its 13th year, with more than 120,000 scenes in archive.

http://eo1.gsfc.nasa.gov/

ALI		**Hyperion**
Band Designations	**Band Names (wavelength, µm)**	
Pan	Pan (0.48 – 0.69)	Continuous Spectra 0.4 – 2.4 µm 242 Bands Bandwidth: 10nm
Blue	MS-1p (0.433 – 0.453)	
	MS-1 (0.450 – 0.515)	
Green	MS-2 (0.525 – 0.605)	
Red	MS-3 (0.633 – 0.690)	
NIR	MS-4 (0.775 – 0.805)	
	MS-4p (0.845 – 0.890)	
SWIR	MS-5p (1.20 – 1.30)	
	MS-5 (1.55 – 1.75)	
	MS-7 (2.08 – 2.35)	
Spatial Resolution	Pan: 10m, MS: 30m	30m
Swath Width	37km	7.7km

Applications of Hyperion Data

Hyperion data have been used in a substantial number of well documented scientific studies which demonstrate the efficacy of the use of space-borne imaging spectroscopy in the following application areas:

* Mineral Mapping

* Hot targets: Fires, Volcanoes

* Vegetation: Forests, Agriculture

* Canopy Water & Surface Water

What does imaging spectroscopy provide beyond multi-spectral?

Quantitative vegetation and
NPV cover in arid regions

Tropical forest canopy chemistry

Logging damage in tropical forests

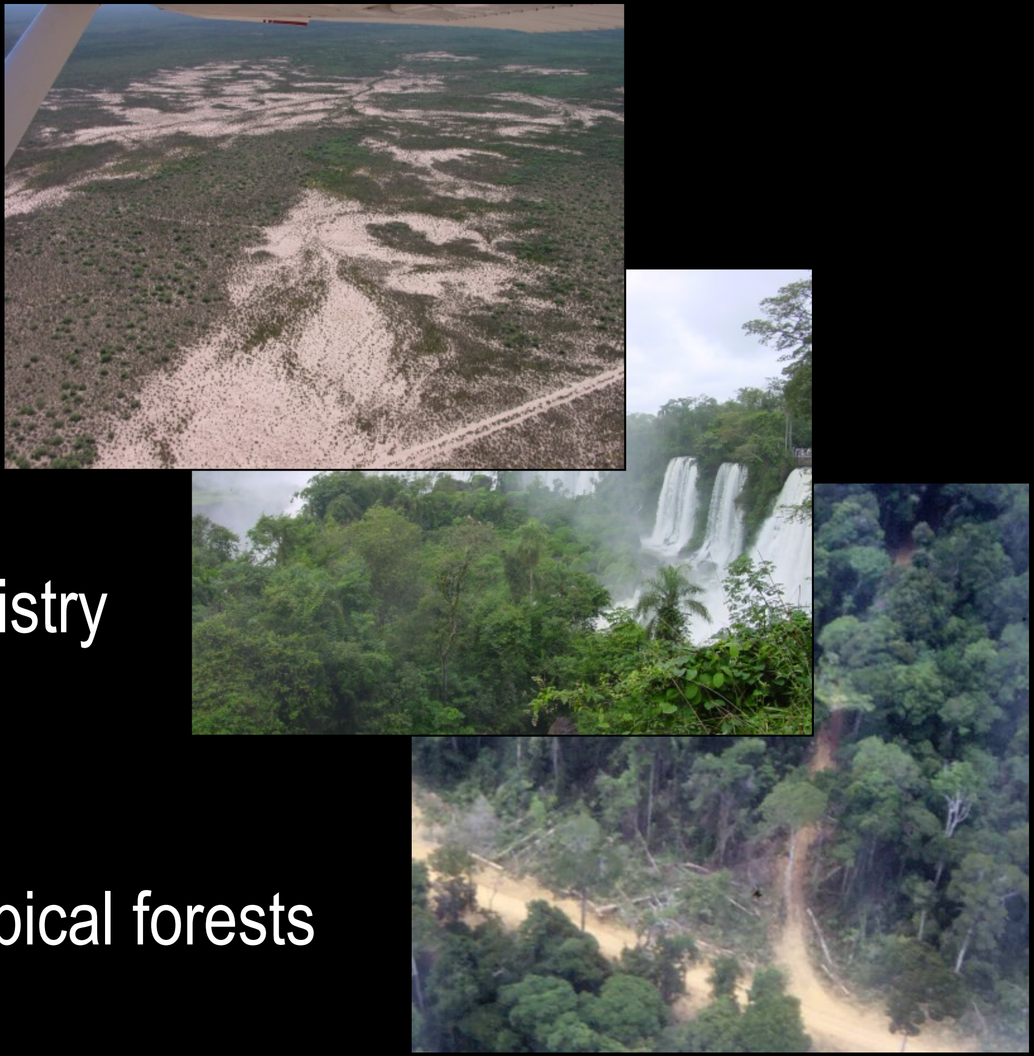

IEEE JSTARS EO-1 Special Issue 2013

This publication includes 20 papers on *"current"* work with ALI and Hyperion data.

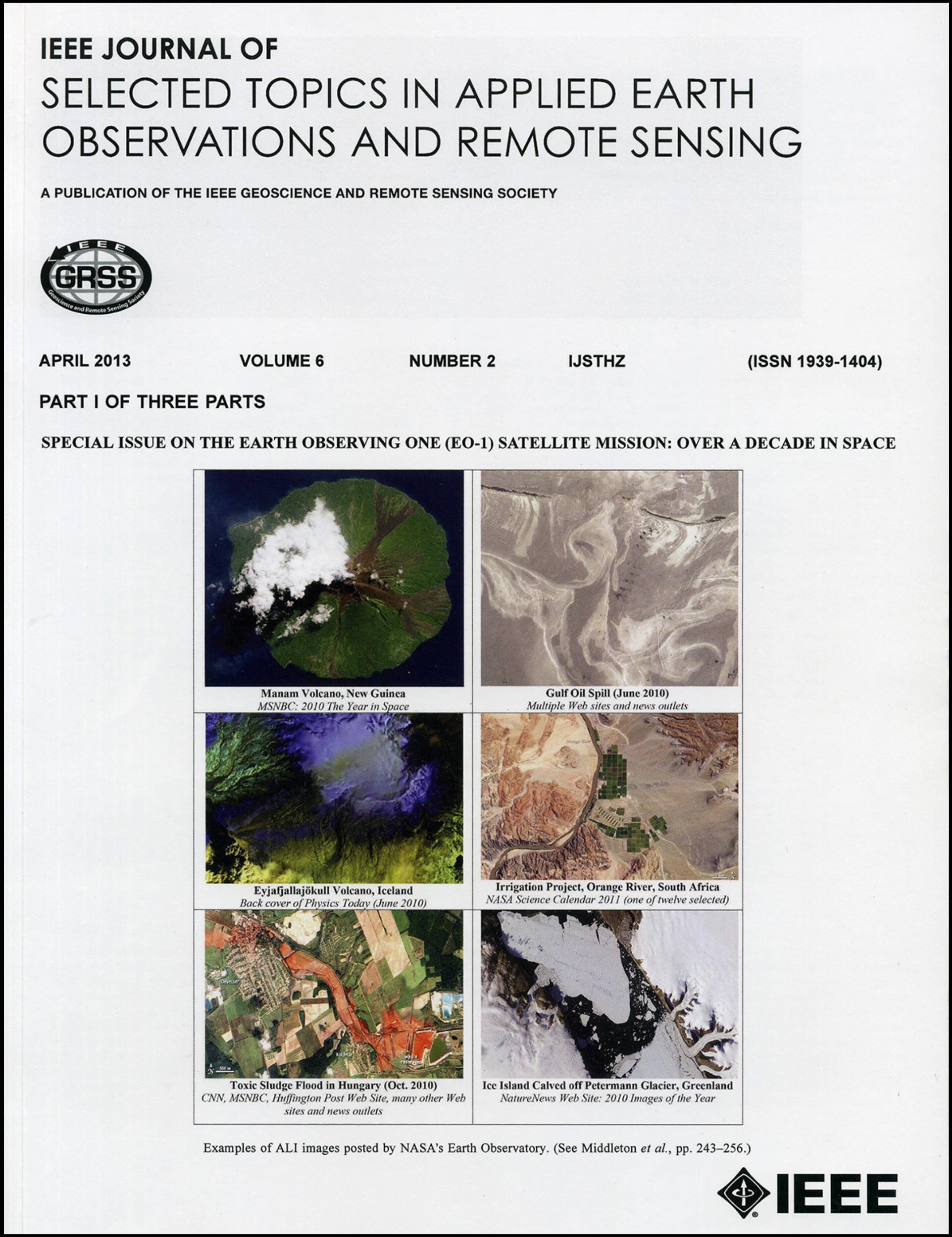

IEEE JOURNAL OF
SELECTED TOPICS IN APPLIED EARTH OBSERVATIONS AND REMOTE SENSING

A PUBLICATION OF THE IEEE GEOSCIENCE AND REMOTE SENSING SOCIETY

APRIL 2013 VOLUME 6 NUMBER 2 IJSTHZ (ISSN 1939-1404)

PART I OF THREE PARTS

SPECIAL ISSUE ON THE EARTH OBSERVING ONE (EO-1) SATELLITE MISSION: OVER A DECADE IN SPACE

Manam Volcano, New Guinea
MSNBC: 2010 The Year in Space

Gulf Oil Spill (June 2010)
Multiple Web sites and news outlets

Eyjafjallajökull Volcano, Iceland
Back cover of Physics Today (June 2010)

Irrigation Project, Orange River, South Africa
NASA Science Calendar 2011 (one of twelve selected)

Toxic Sludge Flood in Hungary (Oct. 2010)
CNN, MSNBC, Huffington Post Web Site, many other Web sites and news outlets

Ice Island Calved off Petermann Glacier, Greenland
NatureNews Web Site: 2010 Images of the Year

Examples of ALI images posted by NASA's Earth Observatory. (See Middleton *et al.*, pp. 243–256.)

IEEE

2013 IEEE/JSTARS EO-1 Special Issue

Special Issue Editor

Betsy Middleton, *NASA/GSFC*

Associate Editors

Melba Crawford, *Purdue University*
Jay Pearlman, *IEEE Fellow, Retired*
Steve Ungar, *NASA/GESTAR-USRA*
Robert Wright, *University of Hawaii*

JSTARS EO-1 Special Issue

Middleton, et al.	The Earth Observing One (EO 1) Satellite Mission: Over a Decade in Space	EO-1 Overview
Chien, et al.	Onboard Product Generation on Earth Observing One: A Pathfinder for the Proposed HyspIRI Mission Intelligent Payload Module	Hyperion Simulating HyspIRI
Huemmrich, et al.	Arctic Tundra Vegetation Functional Types Based on Photosynthetic Physiology and Optical Properties	Hyperion for Vegetation
Campbell, et al.	EO-1 Hyperion Reflectance Time Series at Calibration and Validation Sites: Stability and Sensitivity to Seasonal Dynamics	Hyperion Calibration
Chien, et al.	Monitoring Flooding in Thailand Using Earth Observing One in a Sensorweb	EO-1 for Flooding
Mandl, et al.	Use of the Earth Observing One (EO 1) Satellite for the Namibia SensorWeb Flood Early Warning Pilot	EO-1 for Flooding
Hill, et al.	Use of Vegetation Index ΦFingerprintsX From Hyperion Data to Characterize Vegetation States Within Land Cover/Land Use Types in an Australian Tropical Savanna	Hyperion for Vegetation
Sims, et al.	Towards the Operational Use of Satellite Hyperspectral Image Data for Mapping Nutrient Status and Fertilizer Requirements in Australian Plantation Forests	Hyperion for Vegetation
Goenaga, et al.	Unmixing Analysis of a Time Series of Hyperion Images Over the Gu‡nica Dry Forest in Puerto Rico	Hyperion for Vegetation
Papeş, et al.	Seasonal Variation in Spectral Signatures of Five Genera Rainforest Trees	Hyperion for Vegetation
Somers, et al.	Invasive Species Mapping in Hawaiian Rainforests Using Multi-Temporal Hyperion Spaceborne Imaging Spectroscopy	Hyperion for Invasive Species
Pahlevan, et al.	Leveraging EO-1 to Evaluate Capability of New Generation of Landsat Sensors for Coastal/Inland Water Studies	EO-1 and Landsat
Abrams, et al.	Using EO-1 Hyperion Data as HyspIRI Preparatory Data Sets for Volcanology Applied to Mt Etna, Italy	Hyperion for Volcanology
Chander, et al.	Radiometric Cross Calibration of EO-1 ALI With L7 ETM+ and Terra MODIS Sensors Using Near Simultaneous Desert Observations	EO-1 Cross-Calibration
McCorkel, et al.	Vicarious Calibration of EO 1 Hyperion	Hyperion Calibration
Cappelaere, et al.	Cloud Implementation of a Full Hyperspectral Unmixing Chain within the NASA Web Coverage Processing Service for EO-1	Cloud Processing of Hyperion Data
Yokoya, et al.	Cross-Calibration for Data Fusion of EO-1/Hyperion and Terra/ASTER	Hyperion Cross-Calibration
Thenkabail, et al.	Selection of Hyperspectral Narrowbands (HNBs) and Composition of Hyperspectral Twoband Vegetation Indices (HVIs) for Biophysical Characterization and Discrimination of Crop Types Using Field Reflectance and Hyperion/EO-1 Data	Hyperion for Vegetation
Gartley, et al.	Serendipitous Imaging of Space Objects With the Advanced Land Imager	EO-1 for Space Objects
Galloza, et al.	Crop Residue Modeling and Mapping Using Landsat, ALI, Hyperion and Airborne Remote Sensing Data	Hyperion for Crop Redidue

JSTARS EO-1 Special Issue

Middleton, et al.	The Earth Observing One (EO 1) Satellite Mission: Over a Decade in Space
Chien, et al.	Onboard Product Generation on Earth Observing One: A Pathfinder for the Proposed HyspIRI Mission Intelligent Payload Module
Huemmrich, et al.	Arctic Tundra Vegetation Functional Types Based on Photosynthetic Physiology and Optical Properties
Campbell, et al.	EO-1 Hyperion Reflectance Time Series at Calibration and Validation Sites: Stability and Sensitivity to Seasonal Dynamics
Chien, et al.	Monitoring Flooding in Thailand Using Earth Observing One in a Sensorweb
Mandl, et al.	Use of the Earth Observing One (EO 1) Satellite for the Namibia SensorWeb Flood Early Warning Pilot
Hill, et al.	Use of Vegetation Index ‘Fingerprints’ From Hyperion Data to Characterize Vegetation States Within Land Cover/Land Use Types in an Australian Tropical Savanna
Sims, et al.	Towards the Operational Use of Satellite Hyperspectral Image Data for Mapping Nutrient Status and Fertilizer Requirements in Australian Plantation Forests
Goenaga, et al.	Unmixing Analysis of a Time Series of Hyperion Images Over the Guánica Dry Forest in Puerto Rico
Papeş, et al.	Seasonal Variation in Spectral Signatures of Five Genera Rainforest Trees

JSTARS EO-1 Special Issue

Somers, et al.	Invasive Species Mapping in Hawaiian Rainforests Using Multi-Temporal Hyperion Spaceborne Imaging Spectroscopy
Pahlevan, et al.	Leveraging EO-1 to Evaluate Capability of New Generation of Landsat Sensors for Coastal/Inland Water Studies
Abrams, et al.	Using EO-1 Hyperion Data as HyspIRI Preparatory Data Sets for Volcanology Applied to Mt Etna, Italy
Chander, et al.	Radiometric Cross Calibration of EO-1 ALI with L7 ETM+ and Terra MODIS Sensors Using Near Simultaneous Desert Observations
McCorkel, et al.	Vicarious Calibration of EO 1 Hyperion
Cappelaere, et al.	Cloud Implementation of a Full Hyperspectral Unmixing Chain within the NASA Web Coverage Processing Service for EO-1
Yokoya, et al.	Cross-Calibration for Data Fusion of EO-1/Hyperion and Terra/ASTER
Thenkabail, et al.	Selection of Hyperspectral Narrowbands (HNBs) and Composition of Hyperspectral Twoband Vegetation Indices (HVIs) for Biophysical Characterization and Discrimination of Crop Types Using Field Reflectance and Hyperion/EO-1 Data
Gartley, et al.	Serendipitous Imaging of Space Objects With the Advanced Land Imager
Galloza, et al.	Crop Residue Modeling and Mapping Using Landsat, ALI, Hyperion and Airborne Remote Sensing Data

JSTARS EO-1 Special Issue

Onboard Product Generation on Earth Observing One: A Pathfinder for the Proposed HyspIRI Mission Intelligent Payload Module

Steve Chien, David Mclaren, Daniel Tran, Ashley Gerard Davies, Joshua Doubleday, and Daniel Mandl

Abstract —The proposed HyspIRI mission is evaluating a X-band Direct Broadcast capability that would enable data to be delivered to ground stations virtually as it is acquired. However the HyspIRI VSWIR and TIR instruments are expected to produce over 800 x 10 bits per second of data while the Direct Broad- cast capability is approximately 10 x 10 bits per second for a 80x oversubscription. In order to address this data throughput mismatch a Direct Broadcast concept called the Intelligent Payload Module (IPM) has been developed to determine which data to downlink based on both the type of surface the spacecraft is overlying and onboard processing of the data to detect events. For example, when the spacecraft is overlying polar regions it might downlink a snow/ice product. Additionally the onboard software would search for thermal signatures indicative of a volcanic event or wild fire and downlink summary information (extent, spectra) when detected.

Earth Observing One (EO-1) has served as a test bed and pathfinder for this type of onboard product generation. As part of the Autonomous Sciencecraft (ASE), EO-1 implemented in flight software the ability to analyze and develop products for a limited swath of the Hyperion hyperspectral instrument onboard the spacecraft. In a series of technology demonstrations that became part of the operational EO-1 system over 5000 science products have been generated onboard EO-1 and down linked via engineering S-band contacts, a routine automated process that continues to this day. We describe the onboard products demonstrated in EO-1 operations and show how they have paved the way for the HyspIRI Intelligent Payload Module concept.

Chien, et al. JSTARS 2013

On the left, hot and extreme pixel classification maps developed onboard from Hyperion data. On the right, level one full data downlinked and processed on ground. Both acquired of the Mount Erebus volcano in Antarctica on the 7th May 2004 on two over-flights.

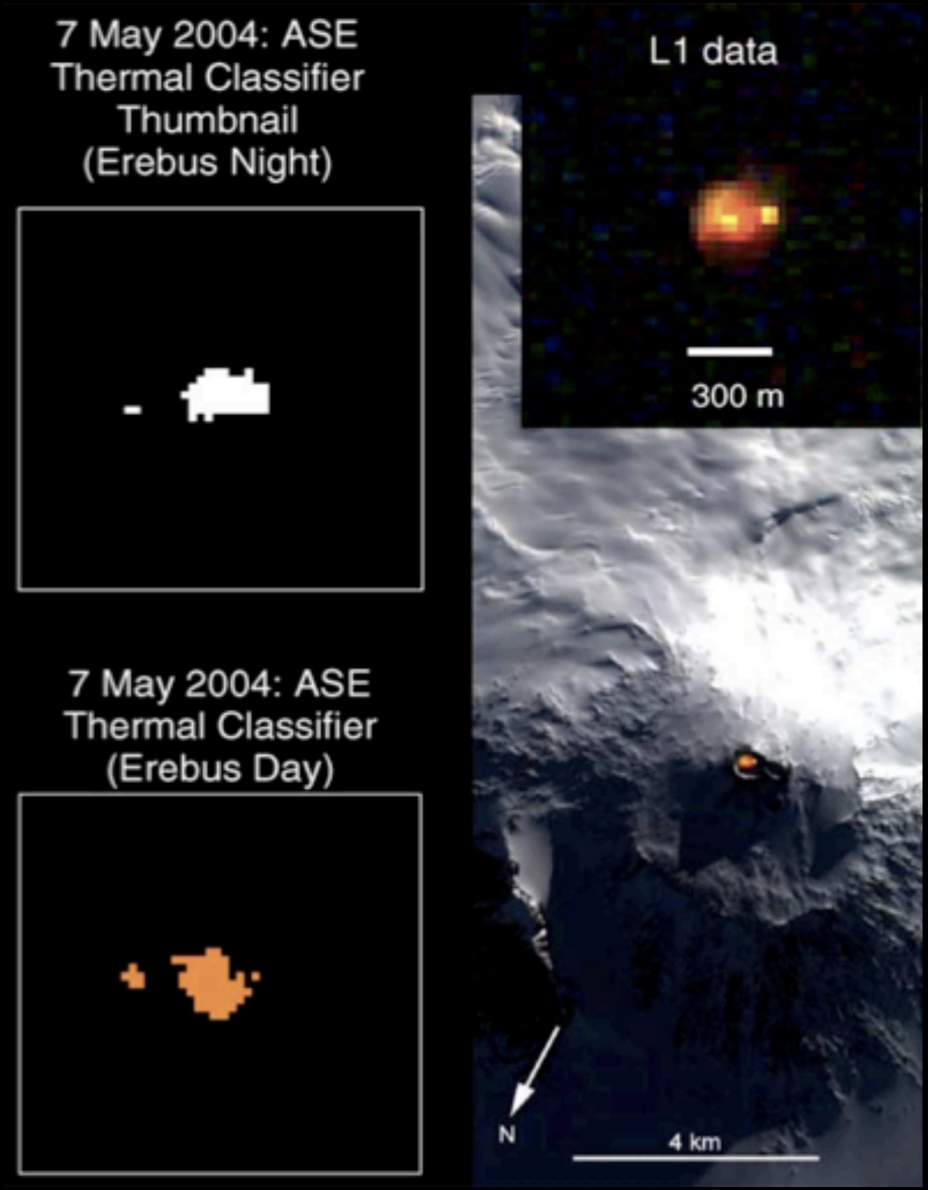

Chien, et al. JSTARS 2013

Sequence of Hyperion flood scenes with the corresponding derived classification maps taken of the Diamantina River in Australia in 2004.

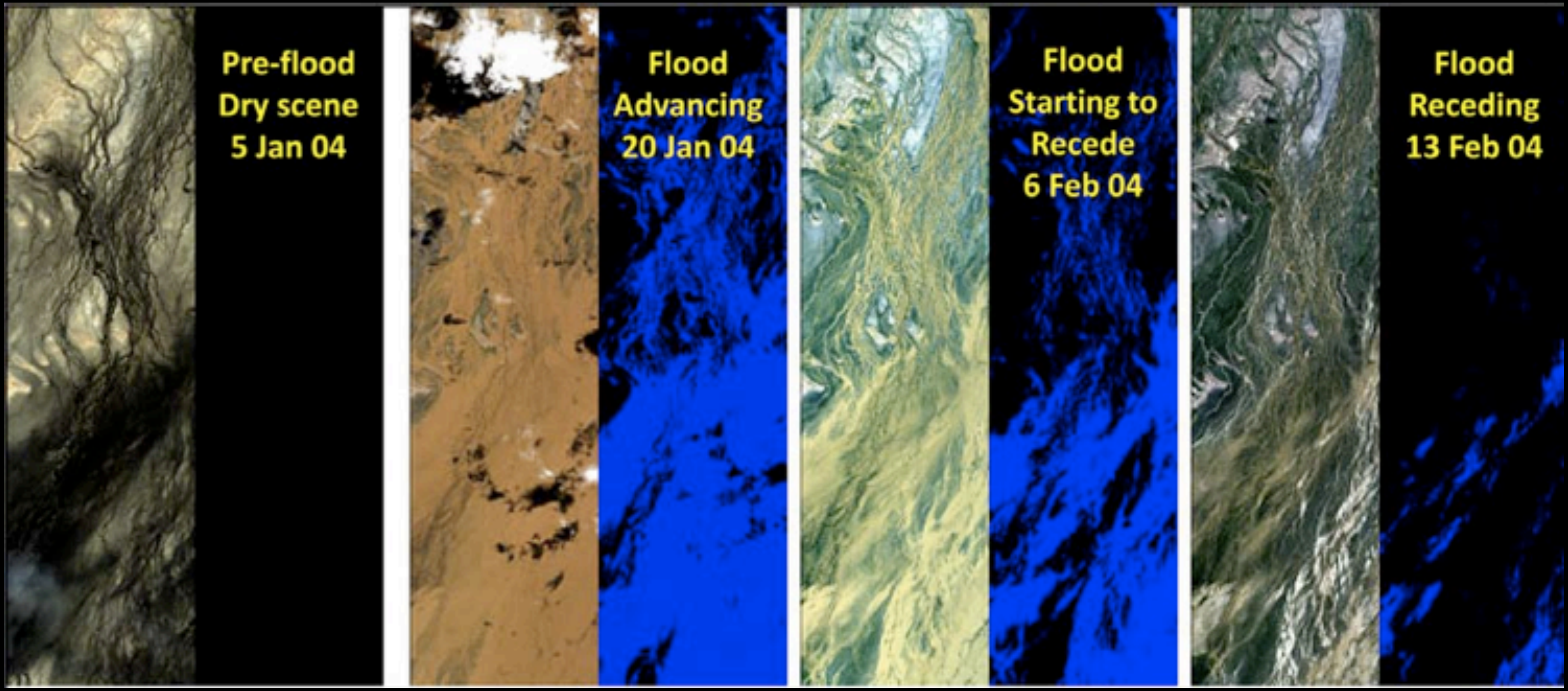

Chien, et al. JSTARS 2013

Hyperion-derived cryosphere classifie,Prudhoe Bay, Alaska.

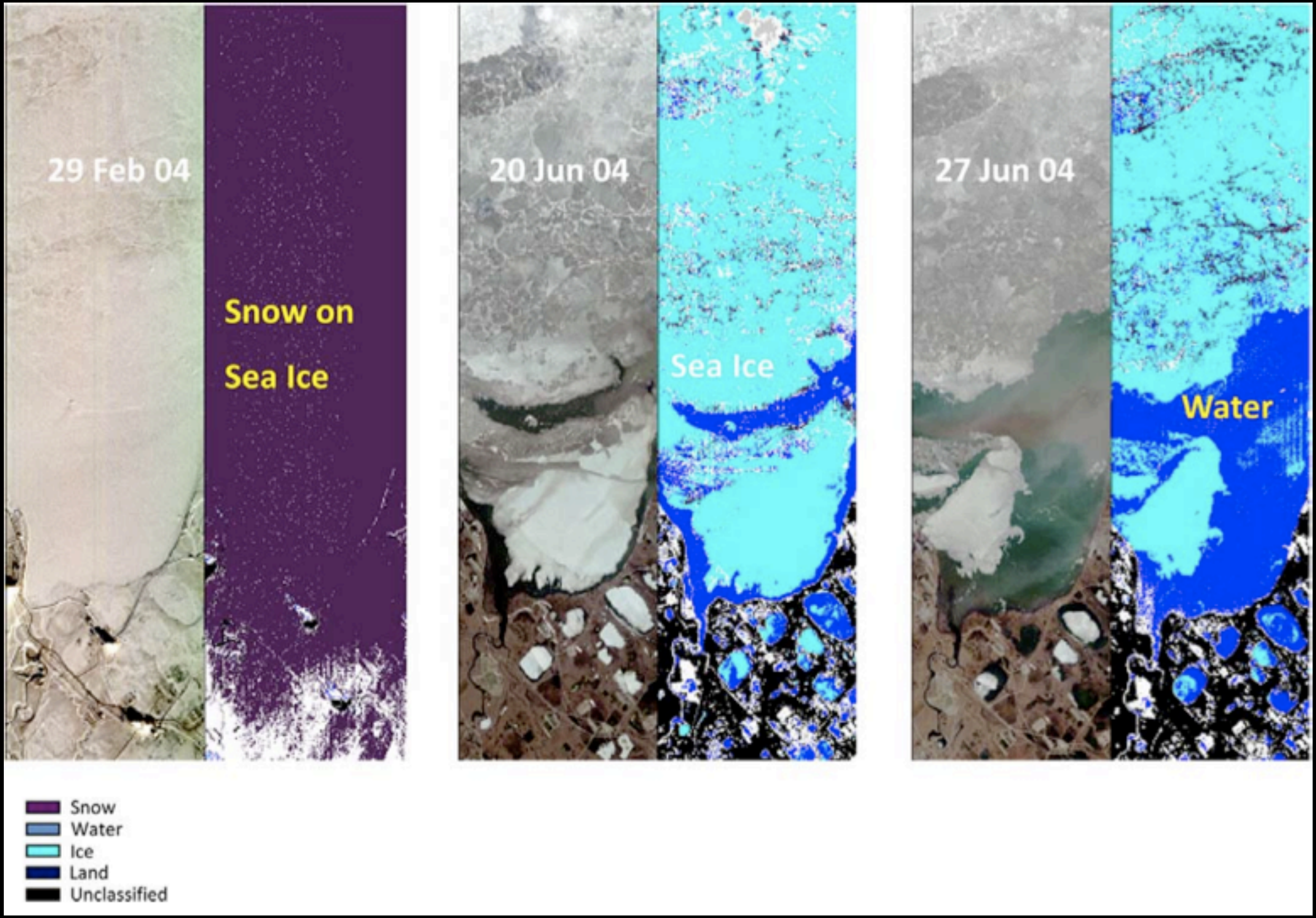

Chien, et al. JSTARS 2013

High interest HyspIRI Intelligent Payload Module products

Discipline	Products	Heritage
Cryosphere	Snow, Water, Ice, Land	Hyperion (onboard) MODIS, ASTER, AVHRR, Landsat (ground)
Volcanology	Thermal Emission	Hyperion (onboard) AVHRR, MODIS (ground)
Hydrology	Surface Water Extent	Hyperion (onboard) MODIS (ground)
Wildfire	Thermal Mapping	Hyperion (onboard) MODIS (ground)
Wildfire	Burn Scar	Hyperion, ALI, ASTER, Landsat, AVHRR, Aviris (ground)

Chien, et al. JSTARS 2013

Moderate interest HyspIRI Intelligent Payload Module products

Discipline	Products	Heritage	Challenge
Aerosols	Overwater Dust, Overland Dust	MODIS, ASTER, MISR, CERES, AVHRR, GMS-SEVIRI, CALIPSO (ground)	Technical challenge
Ecosystem	Vegetation Stress Indicies	AVIRIS, Hyperion, AVHRR (ground)	Limited timeliness driver
Ecosystem	TIR Evapotranspiration	Landsat, MODIS, GOES (ground)	Limited coverage
Disease	Vegetation Disease Risk	AVHRR (ground)	Technical challenge, requires long historical baseline
Oceanography	Ocean Color	MODIS, AVHRR, MERIS, SeaWifs, ASTER, Landsat, VIIRS, Hyperion, CZCS, OCTS (ground)	Technical challenge, low signal strength
Oceanography	Sea Surface Temperature	MODIS	Technical challenge, small temperature differentials, calibration
Volcanology, Wildfire	Smoke Plume	ASTER, MODIS (ground)	Technical challenge, limited coverage

JSTARS EO-1 Special Issue

Arctic Tundra Vegetation Functional Types Based on Photosynthetic Physiology and Optical Properties

Karl Fred Huemmrich, John A. Gamon, Craig E. Tweedie, Petya K. Entcheva Campbell, David R. Landis, and Elizabeth M. Middleton

Abstract — Non-vascular plants (lichens and mosses) are significant components of tundra landscapes and may respond to climate change differently from vascular plants affecting ecosystem carbon balance. Remote sensing provides critical tools for monitoring plant cover types, as optical signals provide a way to scale from plot measurements to regional estimates of biophysical properties. Gas exchange measurements were collected for pure patches of key vegetation functional types (lichens, mosses, and vascular plants) in sedge tundra at Barrow AK. Discriminant analysis of the spectra reflectance of these patches identified five spectral bands that separated each of these vegetation functional types as well as nongreen material (bare soil, standing water, and dead leaves). These results were tested along a 100 m transect where midsummer spectral reflectance and vegetation coverage were measured at one meter intervals.

Along the transect, area-averaged canopy LUE estimated from coverage fractions of the three functional types varied widely, even over short distances. The patch-level statistical discriminant functions applied to in situ hyperspectral reflectance data collected along the transect successfully unmixed cover fractions of the vegetation functional types. The unmixing functions, developed from the transect data, were applied to 30 m spatial resolution Earth Observing-1 Hyperion imaging spectrometer data to examine variability in distribution of the vegetation functional types for an area near Barrow, AK. Spatial variability of LUE was derived from the observed functional type distributions. Across this landscape, a fivefold variation in tundra LUE was observed. LUE calculated from the functional type cover fractions was also correlated to a spectral vegetation index developed to detect vegetation chlorophyll content. The concurrence of these alternate methods suggest that hyperspectral remote sensing can distinguish functionally distinct vegetation types and can be used to develop regional estimates of photosynthetic LUE in tundra landscapes.

Huemmrich, et al. JSTARS 2013

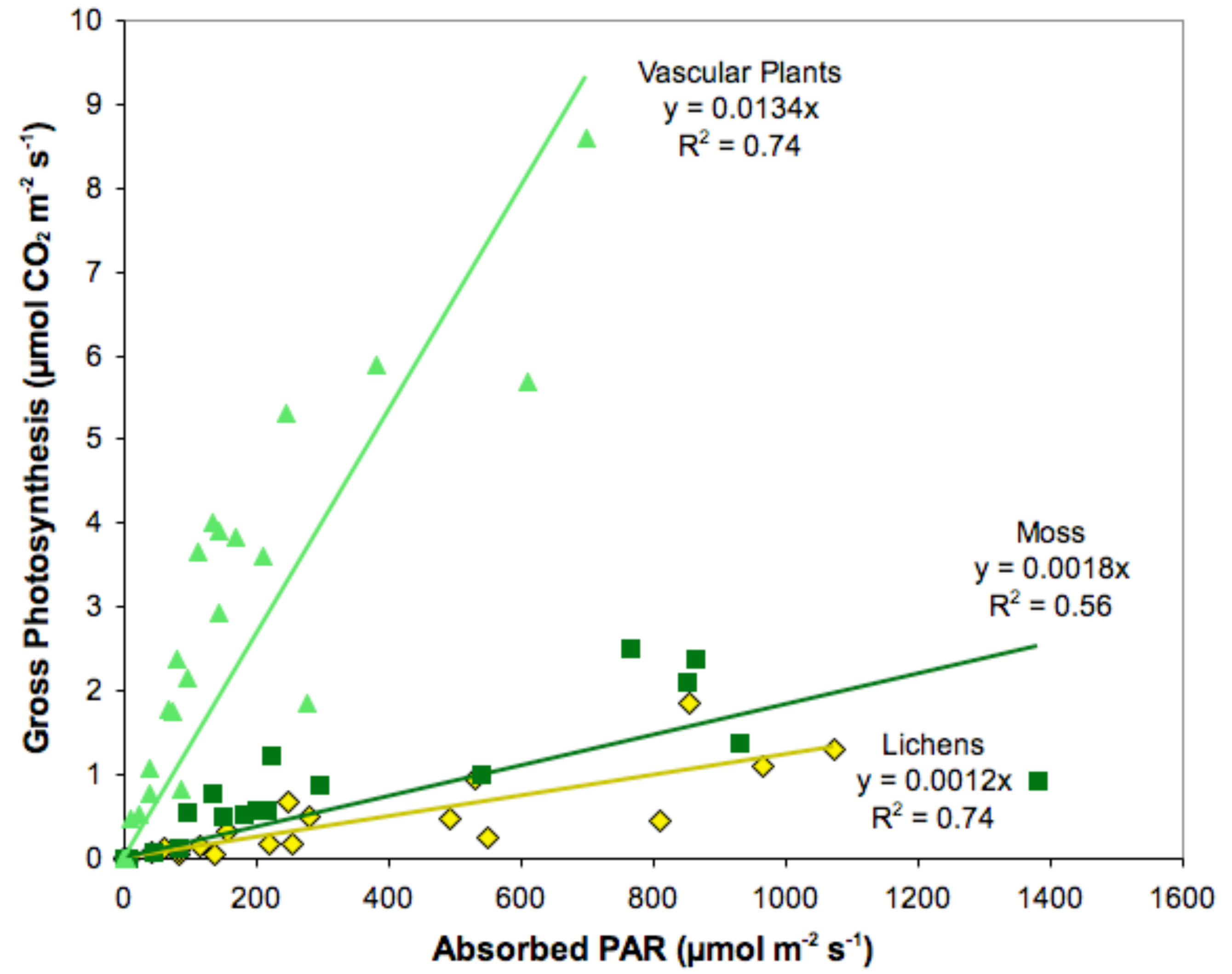

Absorbed PAR and gross photosynthesis for the three vegetation functional types from plot data collected July 20 and August 5, 2001. Light use efficiency for each functional type was calculated from these data as the slope forced through the origin.

Huemmrich, et al. JSTARS 2013

Comparison between observed vegetation functional type coverage normalized to 100% for vascular plants, mosses, and lichens along the Barrow AK transect and cover fractions estimated from spectral reflectance. Line is 1 to 1 line. The absolute error in visual estimates is approximately 9%.

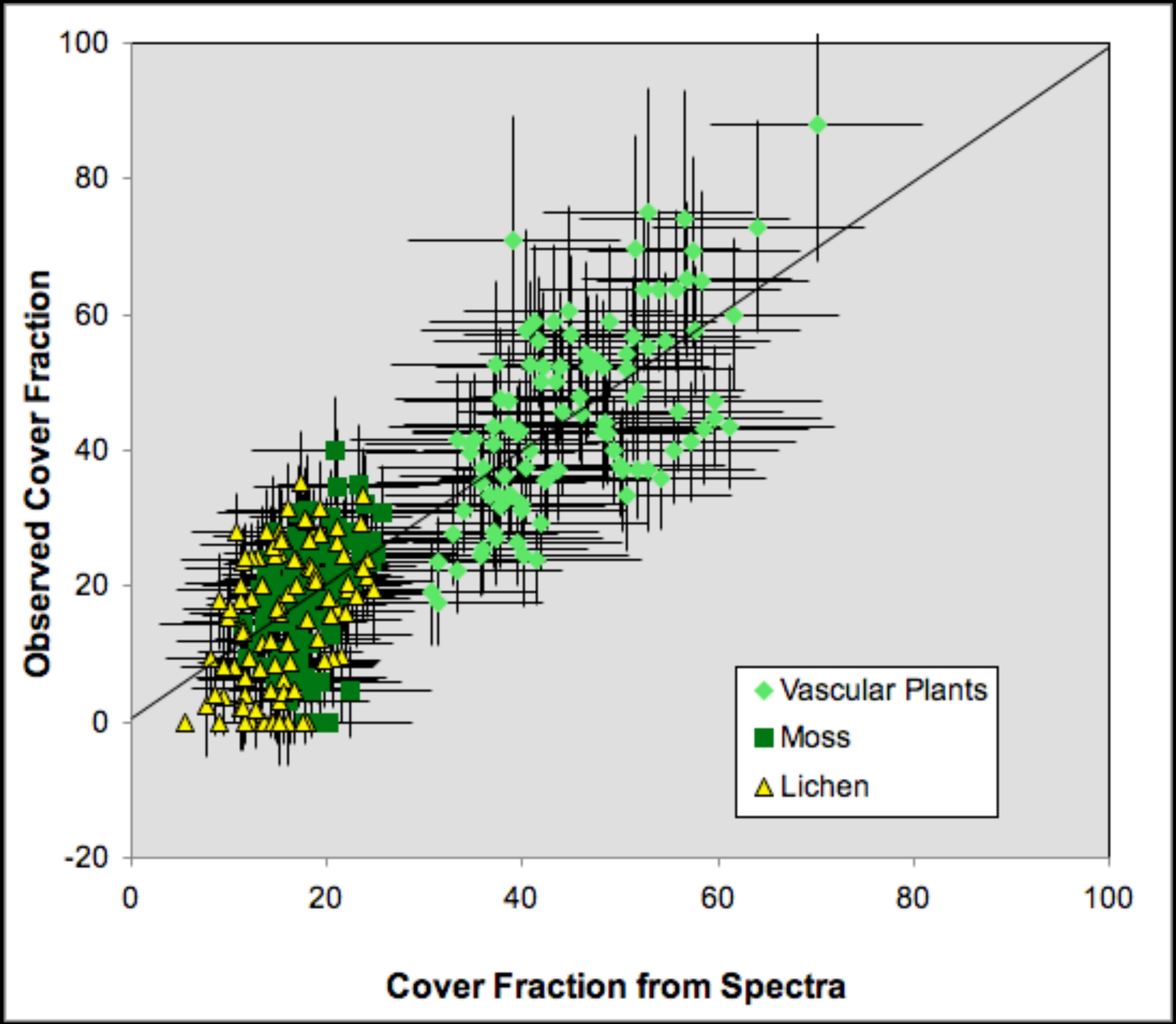

Hyperion Image of Barrow, Alaska

acquired on July 20, 2009

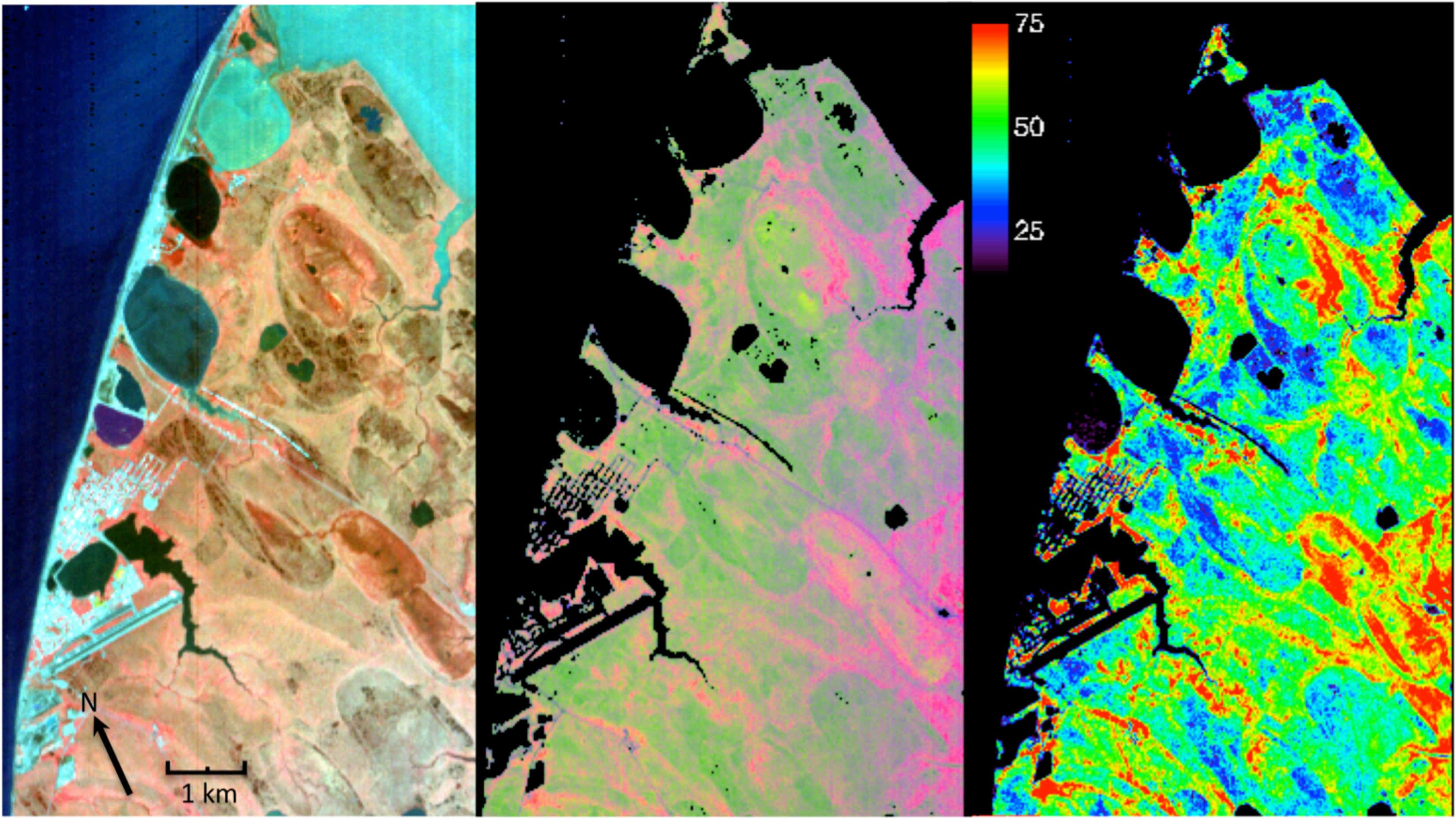

Left: 3-band (RGB=834, 671, and 549 nm) composite image of surface reflectance. The grid of light blue lines on the lower left is the city of Barrow. The straight blue line along the shore near the top of the image is the old airport runway. The oblong features scattered around the region are drained thermokarst lakes and the dark red ones are now marshes.

Middle: Three band RGB continuous fields of estimated coverage of vegetation types derived from spectral unmixing and scaled between 0 and 50% coverage. R = Vascular Plant Cover, G = Moss Cover, B = Lichen Cover

Right: Map of LUE spatial patterns (mol C mol^{-1} quanta x1000) based on coverage estimates.

Huemmrich et al. JSTARS 2013

Huemmrich, et al. JSTARS 2013

Scatter plot of chlorophyll index (x-axis) versus LUE (mol C mol^{-1} quanta x1000) based on normalized cover fractions (y-axis). Both variables were retrieved from the Hyperion image.

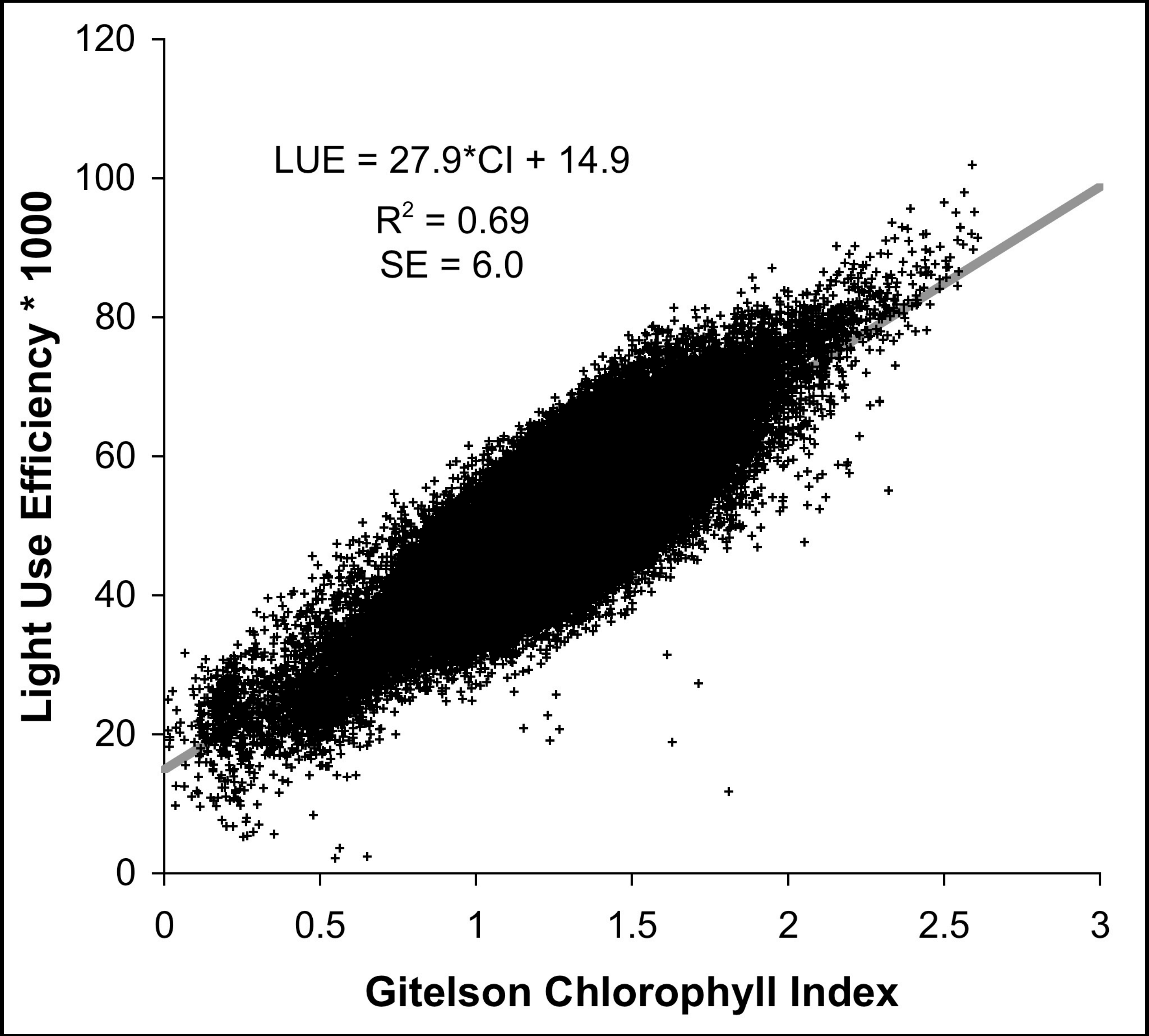

JSTARS EO-1 Special Issue

EO-1 Hyperion Reflectance Time Series at Calibration and Validation Sites: Stability and Sensitivity to Seasonal Dynamics

Petya K. Entcheva Campbell, Elizabeth M. Middleton, Kurt J. Thome, Raymond F. Kokaly, Karl Fred Huemmrich,
David Lagomasino, Kimberly A. Novick, and Nathaniel A. Brunsell

Abstract — This study evaluated Earth Observing 1 (EO-1) Hyperion reflectance time series at established calibration sites to assess the instrument stability and suitability for monitoring vegetation functional parameters. Our analysis using three pseudo-invariant calibration sites in North America indicated that the reflectance time series are devoid of apparent spectral trends and their stability consistently is within 2.5–5 percent throughout most of the spectral range spanning the 12+ year data record. Using three vegetated sites instrumented with eddy covariance towers, the Hyperion reflectance time series were evaluated for their ability to determine important variables of ecosystem function. A number of narrowband and derivative vegetation indices (VI) closely described the seasonal profiles in vegetation function and ecosystem carbon exchange (e.g., net and gross ecosystem productivity) in three very different ecosystems, including a hardwood forest and tallgrass prairie in North America, and a Miombo woodland in Africa. Our results demonstrate the potential for scaling the carbon flux tower measurements to local and regional landscape levels. The VIs with stronger relationships to the CO parameters were derived using continuous reflectance spectra and included wavelengths associated with chlorophyll content and/or chlorophyll fluorescence. Since these indices cannot be calculated from broadband multispectral instrument data, the opportunity to exploit these spectrometer-based VIs in the future will depend on the launch of satellites such as EnMAP and HyspIRI. This study highlights the practical utility of space-borne spectrometers for characterization of the spectral stability and uniformity of the calibration sites in support of sensor cross-comparisons, and demonstrates the potential of narrowband VIs to track and spatially extend ecosystem functional status as well as carbon processes measured at flux towers.

Campbell, et al. JSTARS 2013

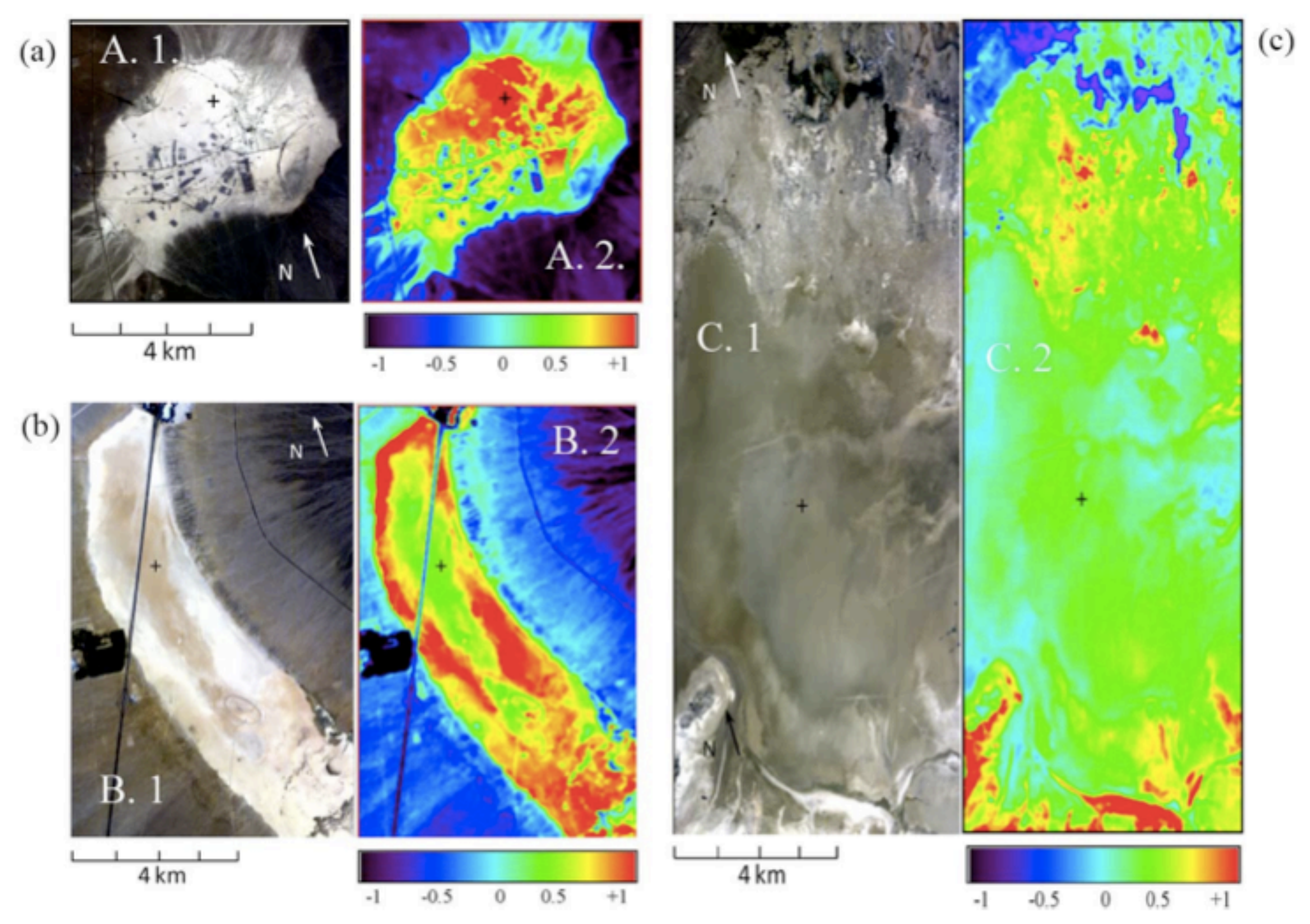

Pseudo invariant calibration sites (PICS): (a) Frenchman Flat (FMF), (b) Ivanpah Playa (IP), and (c) Railroad Valley (RRVP). The center of the region (30–40 pixels) of reflectance extraction is marked with a cross. Two portrayals are shown for each site from a summer acquisition: natural color composites (fig. (a)1, (b)1, (c)1; RGB: 651,549,447 nm), and the Getis G_i statistics calculated to indicate homogeneous pixel clusters (fig. (a)2, (b)2, (c)2).

Campbell, et al. JSTARS 2013

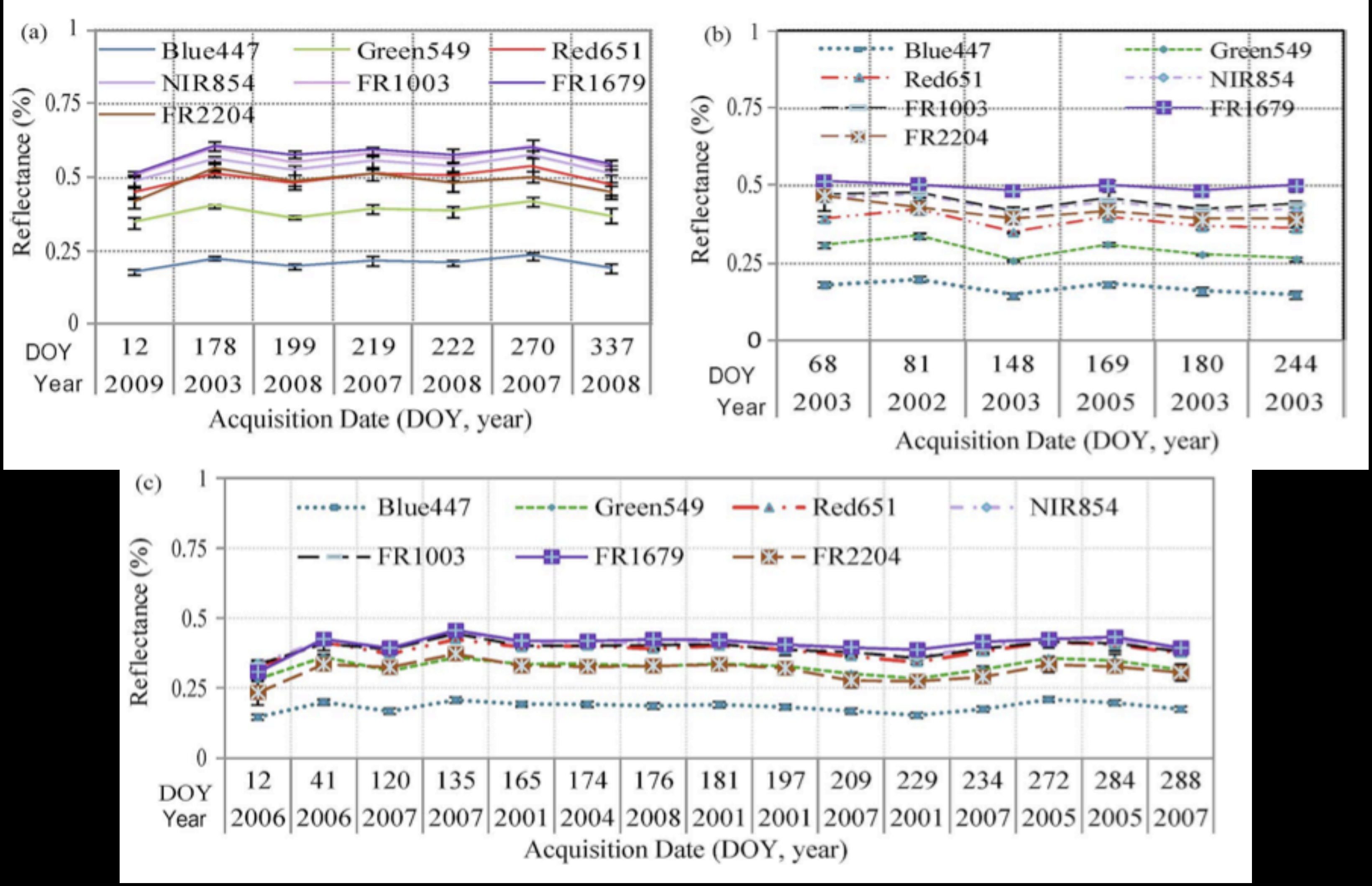

Temporal variation (X±SD) in the Hyperion reflectance at select wavelengths: (a) Frenchman Flat (FMF, 7 images acquired in 2005–2008), (b) Ivanpah (IP, 6 images acquired in 2003–2005) and (c) Railroad Valley (RRVP, 15 images acquired in 2001–2008). The seven Hyperion bands selected to represent the seasonal reflectance trends are centered at: 447, 549, 651, 854, 1003, 1679 and 2204 nm.

Campbell, et al. JSTARS 2013

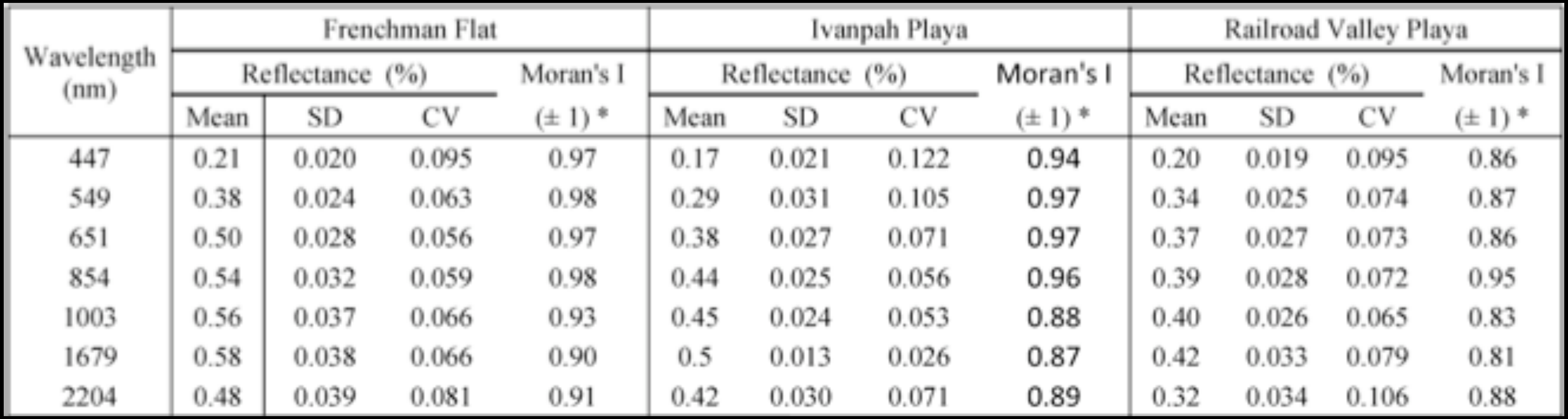

Wavelength (nm)	Frenchman Flat				Ivanpah Playa				Railroad Valley Playa			
	Reflectance (%)			Moran's I	Reflectance (%)			Moran's I	Reflectance (%)			Moran's I
	Mean	SD	CV	(± 1) *	Mean	SD	CV	(± 1) *	Mean	SD	CV	(± 1) *
447	0.21	0.020	0.095	0.97	0.17	0.021	0.122	0.94	0.20	0.019	0.095	0.86
549	0.38	0.024	0.063	0.98	0.29	0.031	0.105	0.97	0.34	0.025	0.074	0.87
651	0.50	0.028	0.056	0.97	0.38	0.027	0.071	0.97	0.37	0.027	0.073	0.86
854	0.54	0.032	0.059	0.98	0.44	0.025	0.056	0.96	0.39	0.028	0.072	0.95
1003	0.56	0.037	0.066	0.93	0.45	0.024	0.053	0.88	0.40	0.026	0.065	0.83
1679	0.58	0.038	0.066	0.90	0.5	0.013	0.026	0.87	0.42	0.033	0.079	0.81
2204	0.48	0.039	0.081	0.91	0.42	0.030	0.071	0.89	0.32	0.034	0.106	0.88

Hyperion reflectance and Moran I statistics for seven wavelengths at these pseudo invariant calibration sites (pics).

Campbell, et al. JSTARS 2013

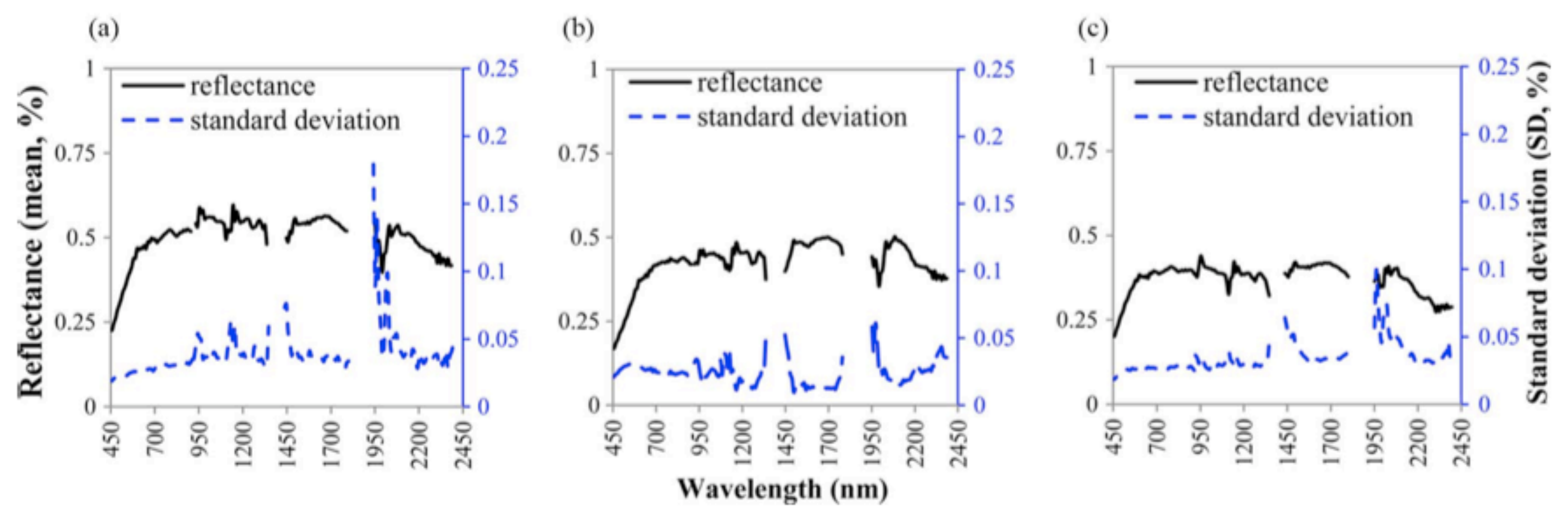

Mean reflectance (%, solid line) and standard deviation (%, dashed line) for time series for: (a) Frenchman Flat (FMF, n=7), (b) Ivanpah Playa (IP, n=6), and (c) Railroad Valley Playa (RRVP, n=15).

Campbell, et al. JSTARS 2013

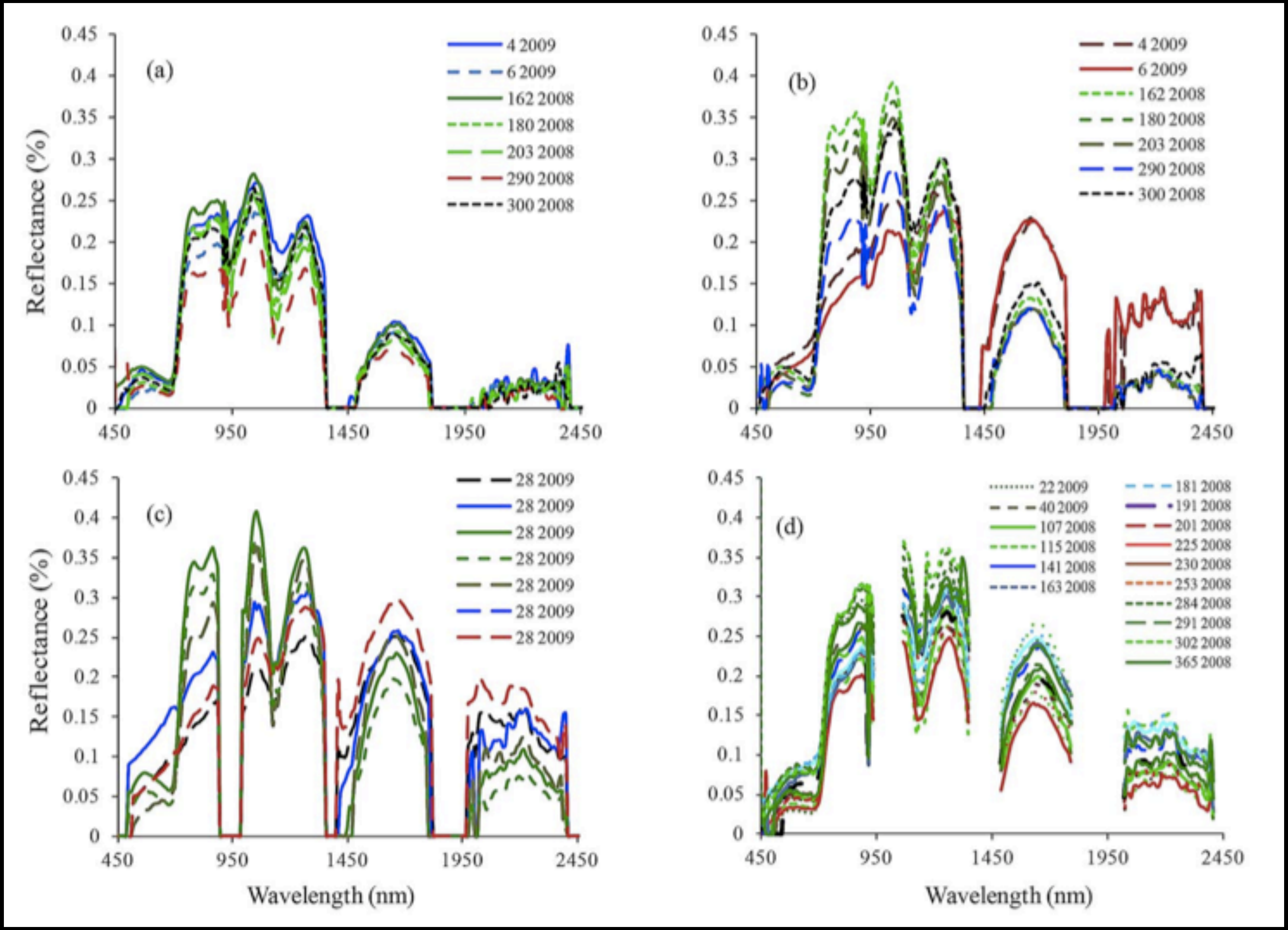

Temporal variation in the Hyperion reflectance acquired over the validation sites: (a) Duke (loblolly pine, LP), (b) Duke (hardwoods, HW), (c) Konza (tallgrass, TG), and (d) Mongu (Miombo woodland, MW). Each line represents the mean site reflectance from a single day, designated in the labels as “DOY year”.

Campbell, et al. JSTARS 2013

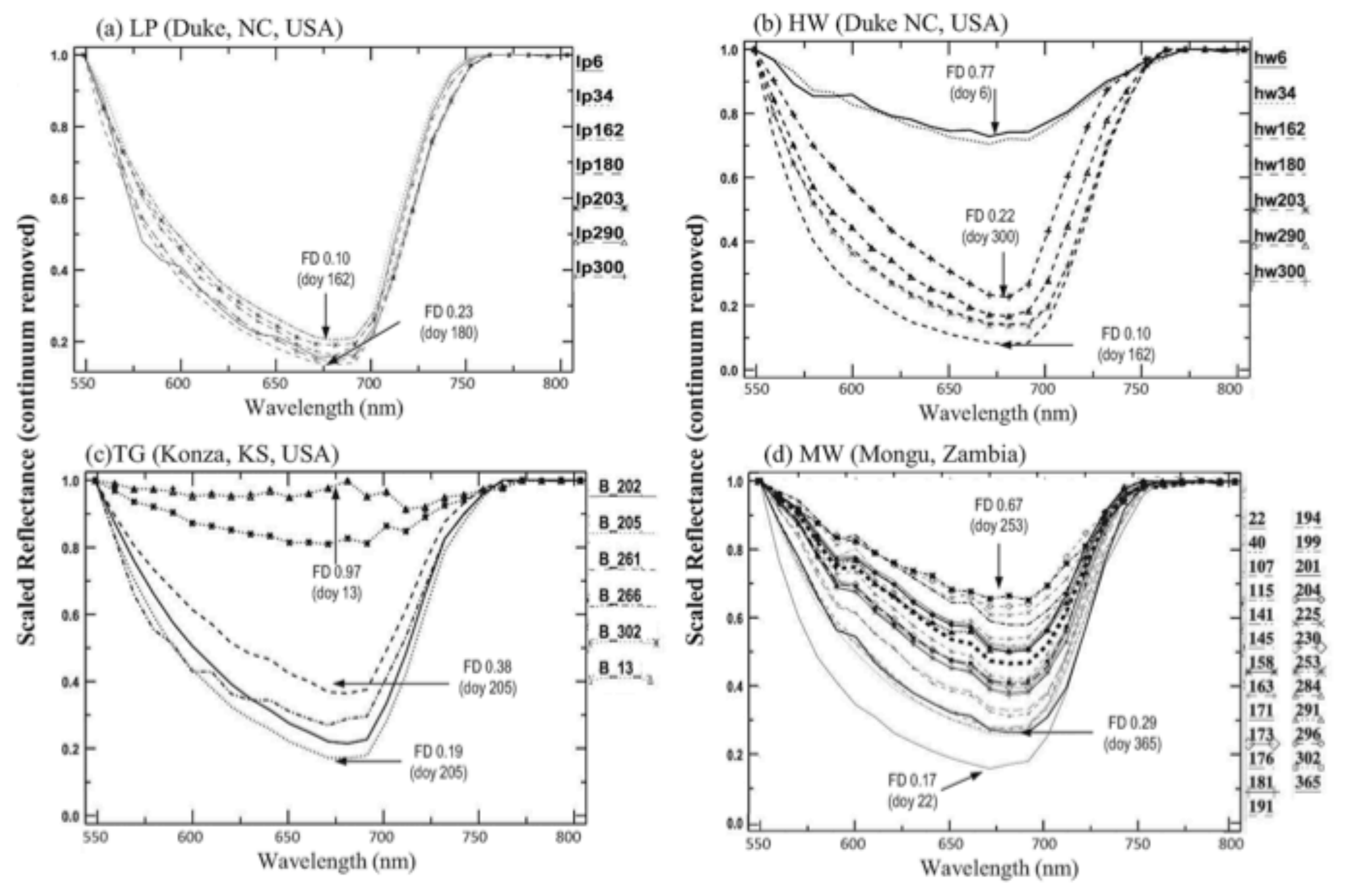

Temporal variation in the mean normalized reflectance (continuum removed) from the chlorophyll absorption feature, (550–750 nm) illustrating the spectral dynamics at each validation site by DOY: (a) Duke LP (n=6 days), (b) Duke HW (n=6 days), (c) Konza TG (n=6 days, each line is an average of spectra from areas under 1 and 4 year burn), and (d) Mongu MW (n=15 days).

Campbell, et al. JSTARS 2013

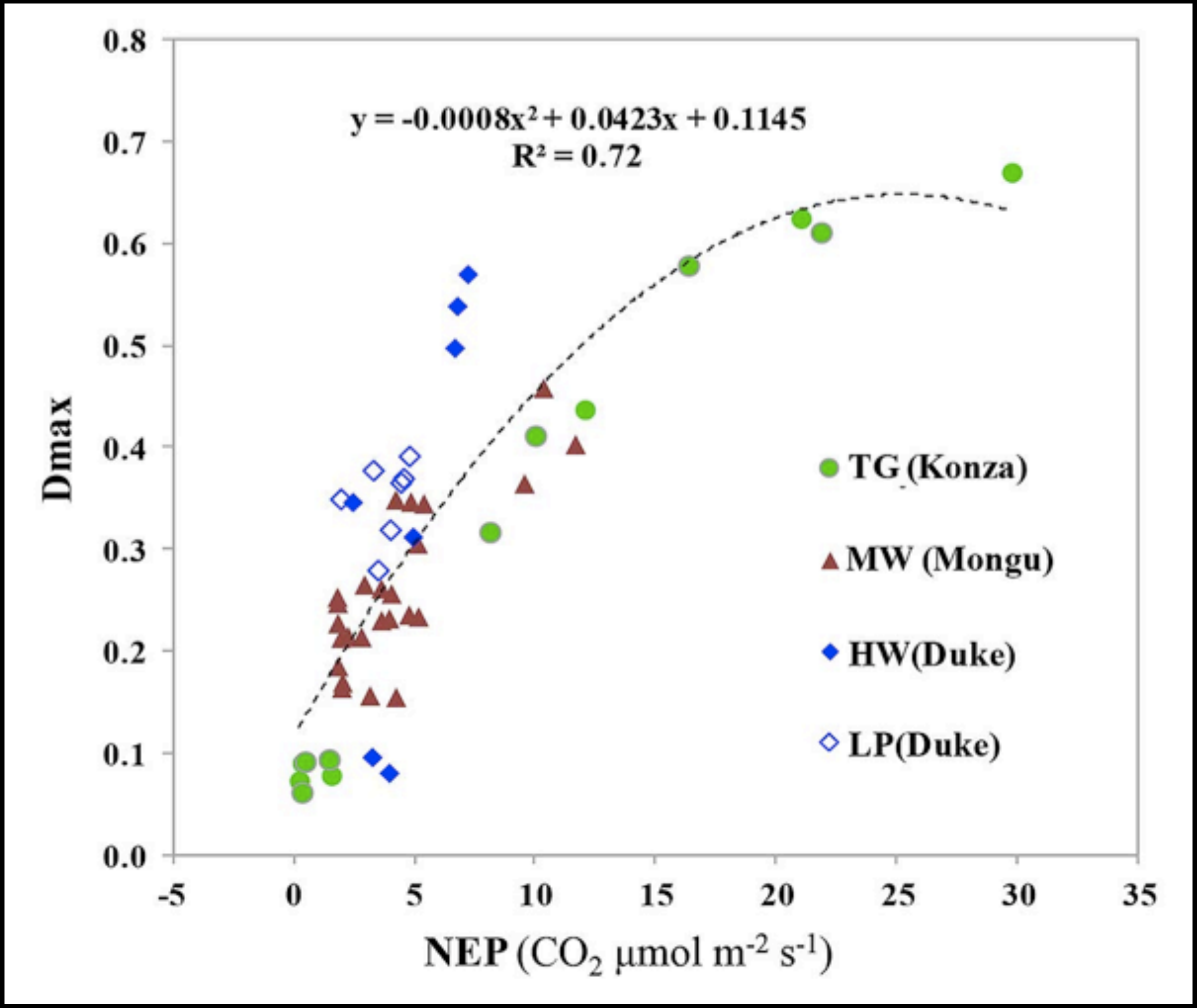

Relationship of Hyperion's derivative index Dmax (the maximum amount of the first derivative in the 650–750 nm region) to the CO_2 assimilation (NEP, µmol m^{-2} s^{-1}) across the three VFS. Dmax had closest relationship when using the combined data set ($n=52$, $p<0.01$). However, this parameter saturated at Dmax > 0.65, precluding the separation of NEP > 20 µmol m^{-2} s^{-1}.

JSTARS EO-1 Special Issue

Use of Vegetation Index "Fingerprints" From Hyperion Data to Characterize Vegetation States Within Land Cover/Land Use Types in an Australian Tropical Savanna

Michael J. Hill, Luigi J. Renzullo, Juan-Pablo Guerschman, Alan S. Marks, and Damian J. Barrett

Abstract — Suites of spectral indices may be derived from hyperspectral sensors such as Hyperion on EO-1. Spectral indices linked to vegetation and landscape function that are scalable to multi-spectral global sensors, could provide "fingerprints" for vegetation states in tropical savannas. In this study, Hyperion images were acquired on three occasions throughout the dry season over each of two consecutive years in the tropical savanna near Darwin, Northern Territory, Australia during 2005 and 2006. This paper examines the changes in fractional cover of photosynthetic and non-photosynthetic vegetation and bare soil and key diagnostic narrow band vegetation indices for major land cover/land use (LCLU) types over two contrasting post-monsoon seasons. The fractional cover proportions and vegetation indices responded strongly to the additional month of full monsoon rains in 2006 versus 2005. There were differences in vegetation indices sensitive to pigments, canopy water and cellulose between LU and LC classes, but within class variation was very high for large sized sample areas. When fine scale variation in vegetation indices and fractional cover were examined as "fingerprints" for small, more uniform areas of specific LC, distinct differences were evident. Vegetation indices and derived vegetation properties can be used to characterize vegetation states at the scale of natural and management-induced variation. The vegetation indices and fractional cover methods used here can be translated and scaled-up to current and new global sensors to improve description of vegetation structure and function in savannas.

Hill, et al. JSTARS 2013

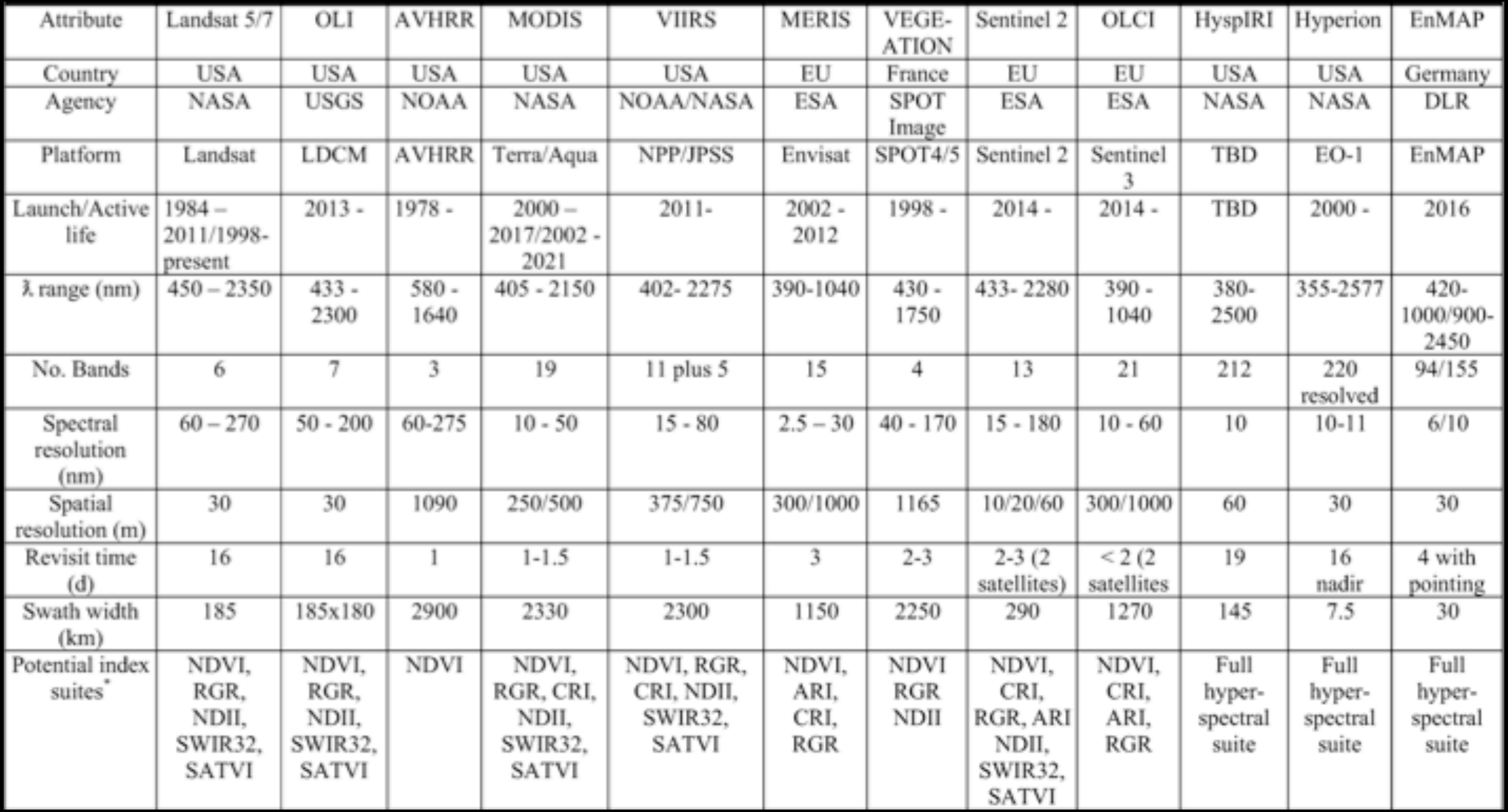

Attribute	Landsat 5/7	OLI	AVHRR	MODIS	VIIRS	MERIS	VEGE-ATION	Sentinel 2	OLCI	HyspIRI	Hyperion	EnMAP
Country	USA	USA	USA	USA	USA	EU	France	EU	EU	USA	USA	Germany
Agency	NASA	USGS	NOAA	NASA	NOAA/NASA	ESA	SPOT Image	ESA	ESA	NASA	NASA	DLR
Platform	Landsat	LDCM	AVHRR	Terra/Aqua	NPP/JPSS	Envisat	SPOT4/5	Sentinel 2	Sentinel 3	TBD	EO-1	EnMAP
Launch/Active life	1984 – 2011/1998-present	2013 -	1978 -	2000 – 2017/2002 - 2021	2011-	2002 - 2012	1998 -	2014 -	2014 -	TBD	2000 -	2016
λ range (nm)	450 – 2350	433 - 2300	580 - 1640	405 - 2150	402- 2275	390-1040	430 - 1750	433- 2280	390 - 1040	380-2500	355-2577	420-1000/900-2450
No. Bands	6	7	3	19	11 plus 5	15	4	13	21	212	220 resolved	94/155
Spectral resolution (nm)	60 – 270	50 - 200	60-275	10 - 50	15 - 80	2.5 – 30	40 - 170	15 - 180	10 - 60	10	10-11	6/10
Spatial resolution (m)	30	30	1090	250/500	375/750	300/1000	1165	10/20/60	300/1000	60	30	30
Revisit time (d)	16	16	1	1-1.5	1-1.5	3	2-3	2-3 (2 satellites)	< 2 (2 satellites	19	16 nadir	4 with pointing
Swath width (km)	185	185x180	2900	2330	2300	1150	2250	290	1270	145	7.5	30
Potential index suites*	NDVI, RGR, NDII, SWIR32, SATVI	NDVI, RGR, NDII, SWIR32, SATVI	NDVI	NDVI, RGR, CRI, NDII, SWIR32, SATVI	NDVI, RGR, CRI, NDII, SWIR32, SATVI	NDVI, ARI, CRI, RGR	NDVI RGR NDII	NDVI, CRI, RGR, ARI NDII, SWIR32, SATVI	NDVI, CRI, ARI, RGR	Full hyper-spectral suite	Full hyper-spectral suite	Full hyper-spectral suite

Characteristics of legacy, current, and planned satellites with global coverage providing operational capacity for optical monitoring of savannas (data for VNIR/SWIR detectors only). Current and future narrow swath hyperspectral sensors are shown for comparison.

Hill, et al. JSTARS 2013

a) The Hyperion swath (2005/2006) showing the two study areas – Northern Region and Southern Region - used here. The lines indicate the boundaries of land use classes. The inset map shows the Australian savanna zone and the location of the Hyperion swath.

b) The Northern 12 Region showing tree canopy cover classes – land use boundaries are shown in outline inside the Hyperion swath.

c) The Southern Region showing tree canopy cover classes – land use boundaries are shown in outline inside the Hyperion swath.

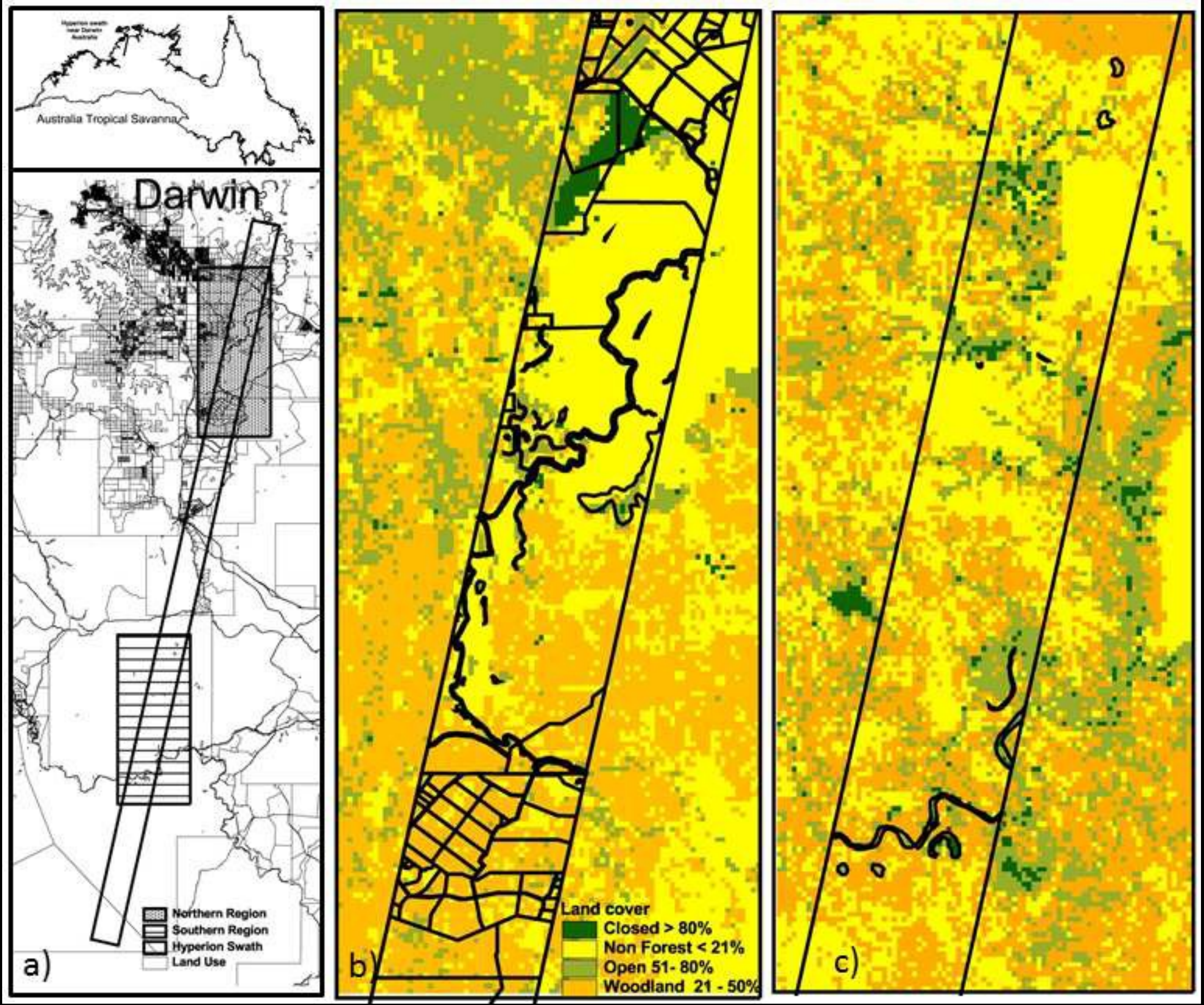

Hill, et al. JSTARS 2013

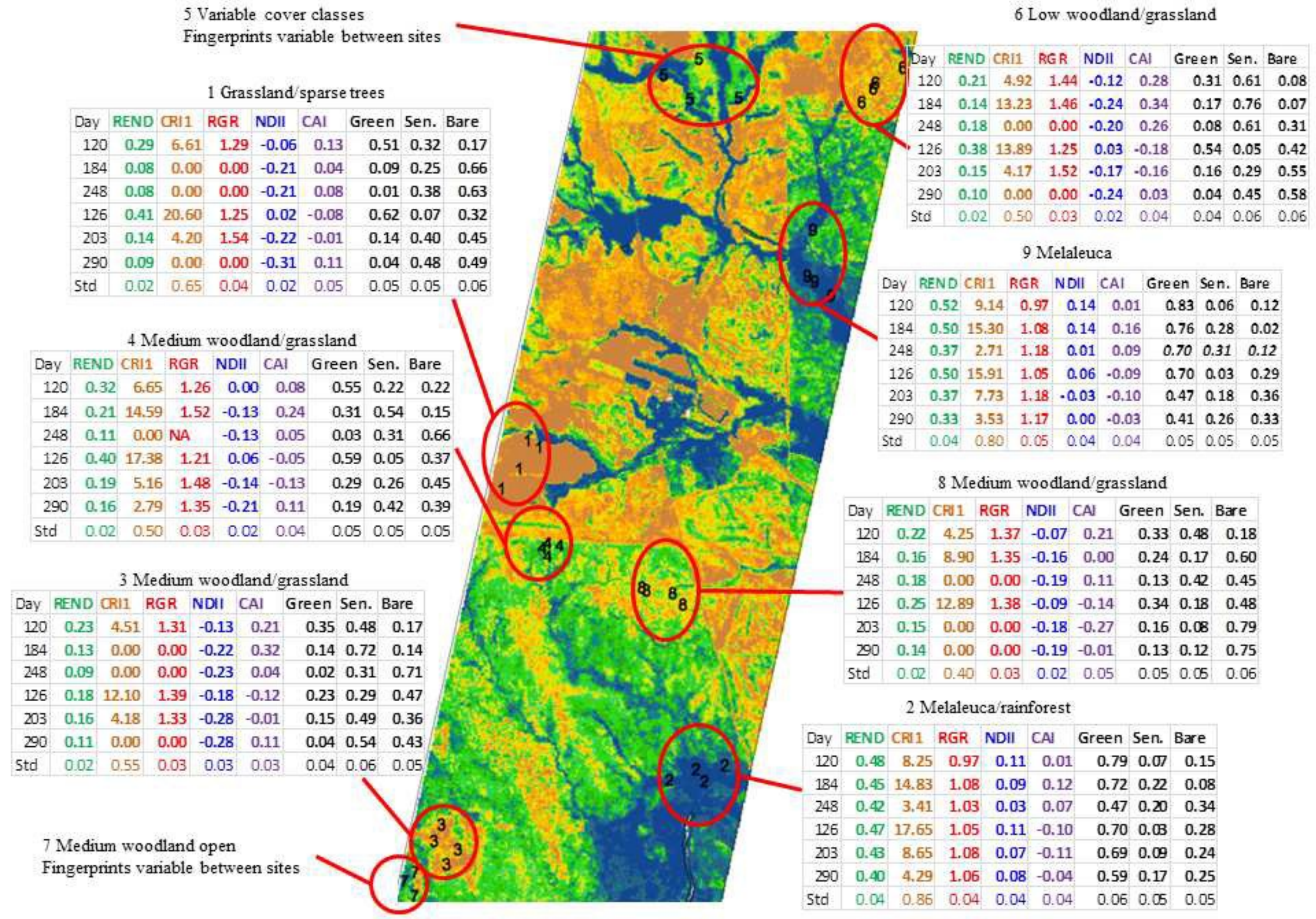

5 Variable cover classes
Fingerprints variable between sites

1 Grassland/sparse trees

Day	REND	CRI1	RGR	NDII	CAI	Green	Sen.	Bare
120	0.29	6.61	1.29	-0.06	0.13	0.51	0.32	0.17
184	0.08	0.00	0.00	-0.21	0.04	0.09	0.25	0.66
248	0.08	0.00	0.00	-0.21	0.08	0.01	0.38	0.63
126	0.41	20.60	1.25	0.02	-0.08	0.62	0.07	0.32
203	0.14	4.20	1.54	-0.22	-0.01	0.14	0.40	0.45
290	0.09	0.00	0.00	-0.31	0.11	0.04	0.48	0.49
Std	0.02	0.65	0.04	0.02	0.05	0.05	0.05	0.06

4 Medium woodland/grassland

Day	REND	CRI1	RGR	NDII	CAI	Green	Sen.	Bare
120	0.32	6.65	1.26	0.00	0.08	0.55	0.22	0.22
184	0.21	14.59	1.52	-0.13	0.24	0.31	0.54	0.15
248	0.11	0.00	NA	-0.13	0.05	0.03	0.31	0.66
126	0.40	17.38	1.21	0.06	-0.05	0.59	0.05	0.37
203	0.19	5.16	1.48	-0.14	-0.13	0.29	0.26	0.45
290	0.16	2.79	1.35	-0.21	0.11	0.19	0.42	0.39
Std	0.02	0.50	0.03	0.02	0.04	0.05	0.05	0.05

3 Medium woodland/grassland

Day	REND	CRI1	RGR	NDII	CAI	Green	Sen.	Bare
120	0.23	4.51	1.31	-0.13	0.21	0.35	0.48	0.17
184	0.13	0.00	0.00	-0.22	0.32	0.14	0.72	0.14
248	0.09	0.00	0.00	-0.23	0.04	0.02	0.31	0.71
126	0.18	12.10	1.39	-0.18	-0.12	0.23	0.29	0.47
203	0.16	4.18	1.33	-0.28	-0.01	0.15	0.49	0.36
290	0.11	0.00	0.00	-0.28	0.11	0.04	0.54	0.43
Std	0.02	0.55	0.03	0.03	0.03	0.04	0.06	0.05

7 Medium woodland open
Fingerprints variable between sites

6 Low woodland/grassland

Day	REND	CRI1	RGR	NDII	CAI	Green	Sen.	Bare
120	0.21	4.92	1.44	-0.12	0.28	0.31	0.61	0.08
184	0.14	13.23	1.46	-0.24	0.34	0.17	0.76	0.07
248	0.18	0.00	0.00	-0.20	0.26	0.08	0.61	0.31
126	0.38	13.89	1.25	0.03	-0.18	0.54	0.05	0.42
203	0.15	4.17	1.52	-0.17	-0.16	0.16	0.29	0.55
290	0.10	0.00	0.00	-0.24	0.03	0.04	0.45	0.58
Std	0.02	0.50	0.03	0.02	0.04	0.04	0.06	0.06

9 Melaleuca

Day	REND	CRI1	RGR	NDII	CAI	Green	Sen.	Bare
120	0.52	9.14	0.97	0.14	0.01	0.83	0.06	0.12
184	0.50	15.30	1.08	0.14	0.16	0.76	0.28	0.02
248	0.37	2.71	1.18	0.01	0.09	*0.70*	*0.31*	*0.12*
126	0.50	15.91	1.05	0.06	-0.09	0.70	0.03	0.29
203	0.37	7.73	1.18	-0.03	-0.10	0.47	0.18	0.36
290	0.33	3.53	1.17	0.00	-0.03	0.41	0.26	0.33
Std	0.04	0.80	0.05	0.04	0.04	0.05	0.05	0.05

8 Medium woodland/grassland

Day	REND	CRI1	RGR	NDII	CAI	Green	Sen.	Bare
120	0.22	4.25	1.37	-0.07	0.21	0.33	0.48	0.18
184	0.16	8.90	1.35	-0.16	0.00	0.24	0.17	0.60
248	0.18	0.00	0.00	-0.19	0.11	0.13	0.42	0.45
126	0.25	12.89	1.38	-0.09	-0.14	0.34	0.18	0.48
203	0.15	0.00	0.00	-0.18	-0.27	0.16	0.08	0.79
290	0.14	0.00	0.00	-0.19	-0.01	0.13	0.12	0.75
Std	0.02	0.40	0.03	0.02	0.05	0.05	0.05	0.06

2 Melaleuca/rainforest

Day	REND	CRI1	RGR	NDII	CAI	Green	Sen.	Bare
120	0.48	8.25	0.97	0.11	0.01	0.79	0.07	0.15
184	0.45	14.83	1.08	0.09	0.12	0.72	0.22	0.08
248	0.42	3.41	1.03	0.03	0.07	0.47	0.20	0.34
126	0.47	17.65	1.05	0.11	-0.10	0.70	0.03	0.28
203	0.43	8.65	1.08	0.07	-0.11	0.69	0.09	0.24
290	0.40	4.29	1.06	0.08	-0.04	0.59	0.17	0.25
Std	0.04	0.86	0.04	0.04	0.04	0.06	0.05	0.05

Characterization of vegetation states with vegetation index fingerprints for selected areas within land cover types for region 2 where natural savanna vegetation and grazing land use predominate. Fingerprints are shown as tables with day of year for 2005 and 2006 shown in the first column. Fractional cover values in the last three columns are in decimal proportions. Values represent the average for the sites shown. The last row shows the average standard deviation over the six image dates.

JSTARS EO-1 Special Issue

Towards the Operational Use of Satellite Hyperspectral Image Data for Mapping Nutrient Status and Fertilizer Requirements in Australian Plantation Forests

Neil C. Sims, Darius Culvenor, Glenn Newnham, Nicholas C. Coops, and Peter Hopmans

Abstract — EO-1/Hyperion data can potentially reduce the cost of nutrition assessments in plantation forests, supplementing standard point-based measurements with comprehensive and repeated broad-acre coverage. We present a synopsis of studies using EO-1/ Hyperion data for foliar nutrition assessments in Australia. The earliest study compared modeling methods and calculated models in the order of for Nitrogen, Phosphorus and Boron in Eucalyptus and Pinus species. Several recommendations of that work were adopted in a subsequent project which concluded that observing stand structure may improve nutrient prediction models calibrated from image data over those calibrated from laboratory spectra. The most recent study examined the range of age classes over which nutrients could be accurately predicted in P. radiata from Hyperion images. Canopy cover fraction, calculated using spectral mixture analysis, ranged from 69% in unthinned 5 year old stands to 43% and 41% in stands 10 to 20 years old that had been thinned once or twice respectively. The value when predicting Nitrogen across all age classes was 0.45 increasing to 0.87 when calibrated on only the 5 year old trees. Collectively, these studies demonstrate that several important nutrients can be accurately mapped from Hyperion data at ages that are critical for the management of plantation forests. However, some of Hyperion's spatial and radiometric characteristics limit its practical operational application. This manuscript discusses potential improvements that might be provided by the HyspIRI mission, and the key challenges in developing hyperspectral image data as an operational tool for forest nutrition assessments in Australia.

Sims, et al. JSTARS 2013

Mosaic of three Hyperion images captured on 24 Jun (Primary scene), 25 July and 10 August (secondary scenes 2 and 1 respectively) in 2005 showing a south-east Queensland exotic pine estate. Three images were required to provide coverage of EW extent of the estate. Circles identify sampling plot locations.

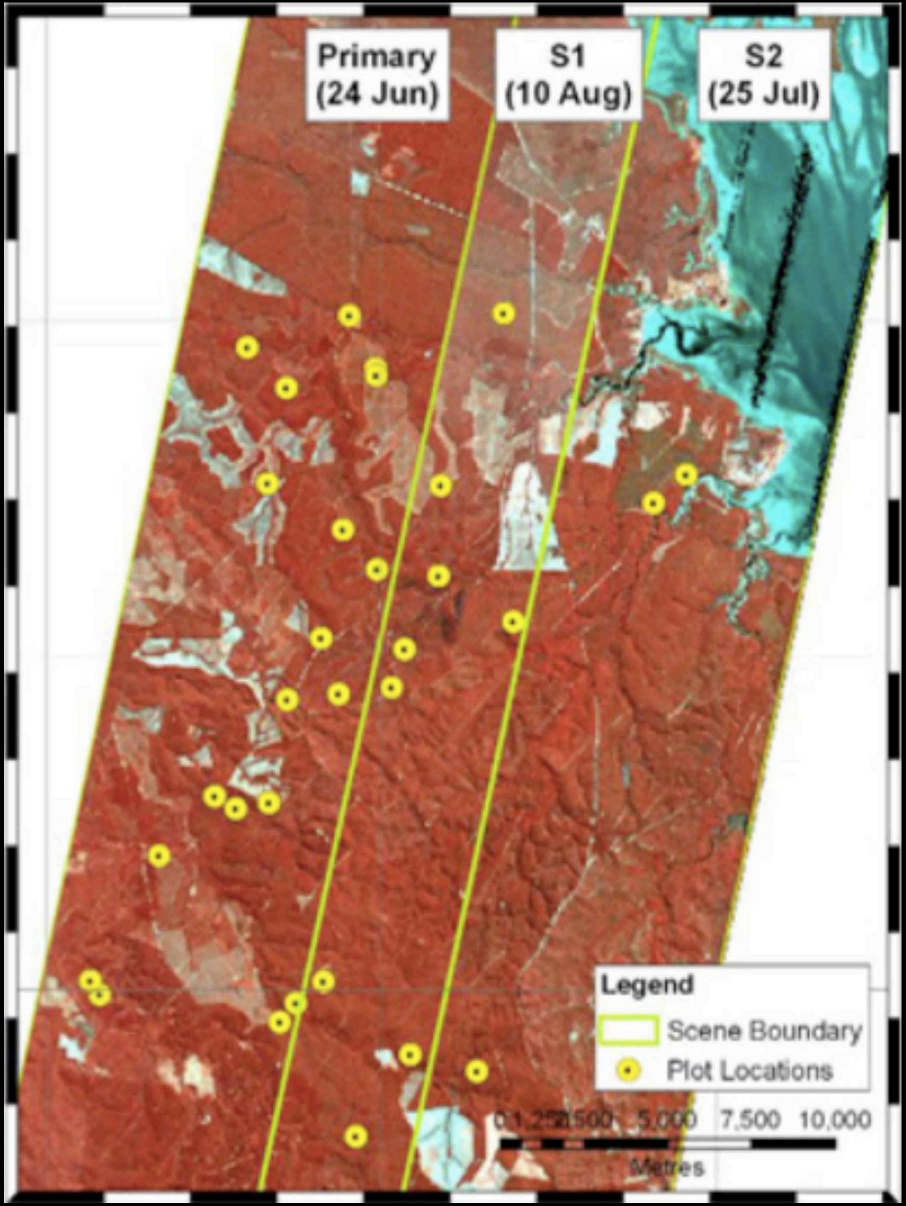

Sims, et al. JSTARS 2013

Examples of noise characteristics in Hyperion images showing (a) band dropouts, (b) streaking and (c) along-track change in brightness due to 'spectral smile'.

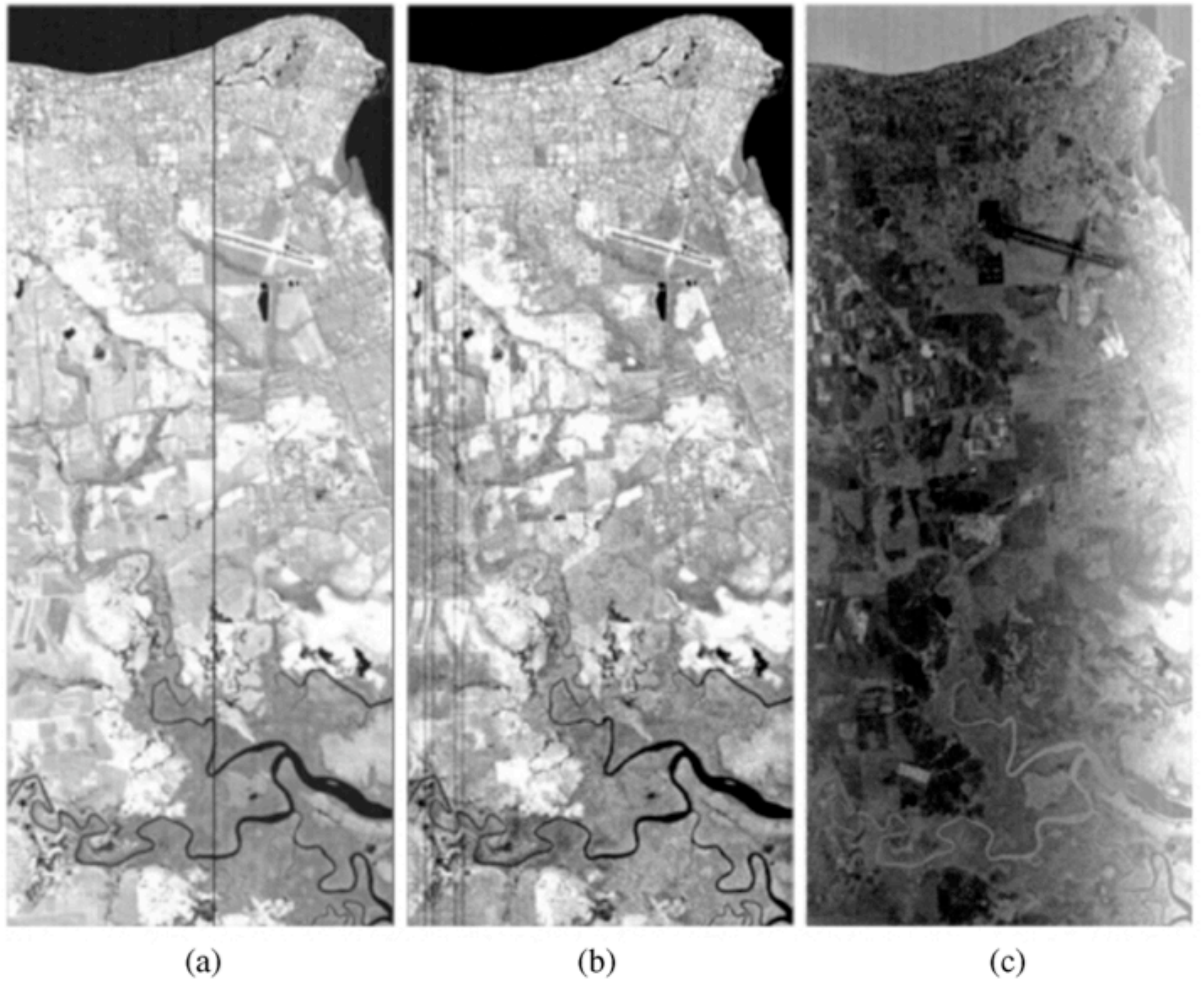

(a) (b) (c)

Sims, et al. JSTARS 2013

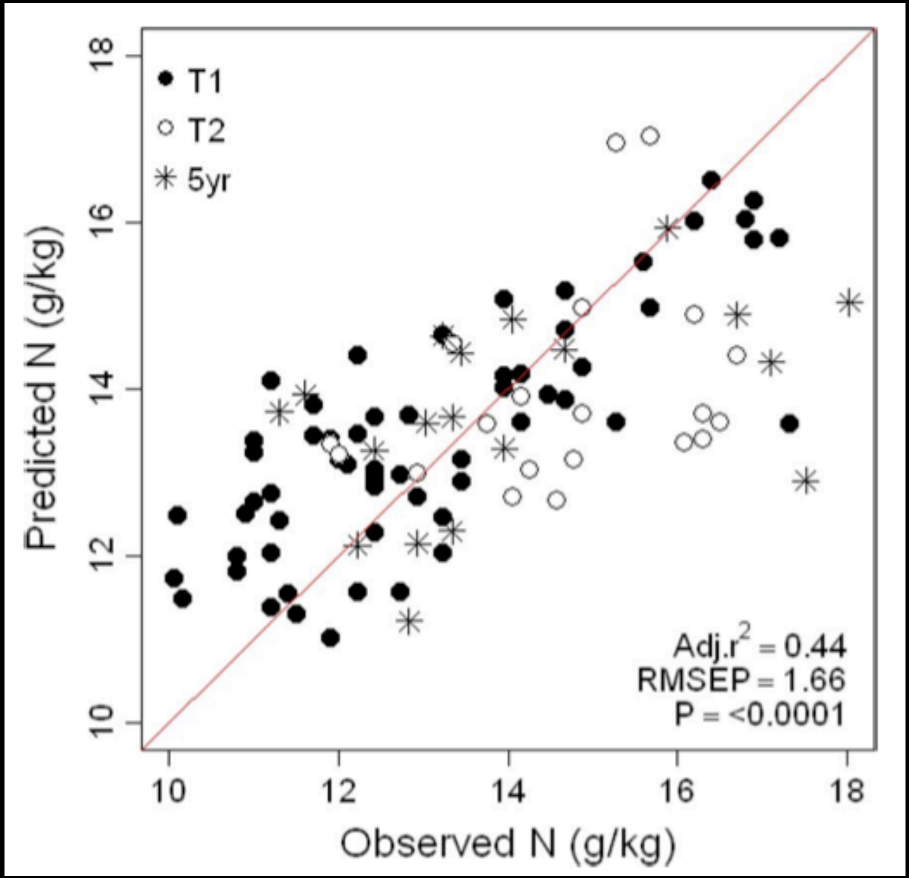

Predicted versus observed N concentration over all plots from Sims et al., showing cross validated model fit statistics.

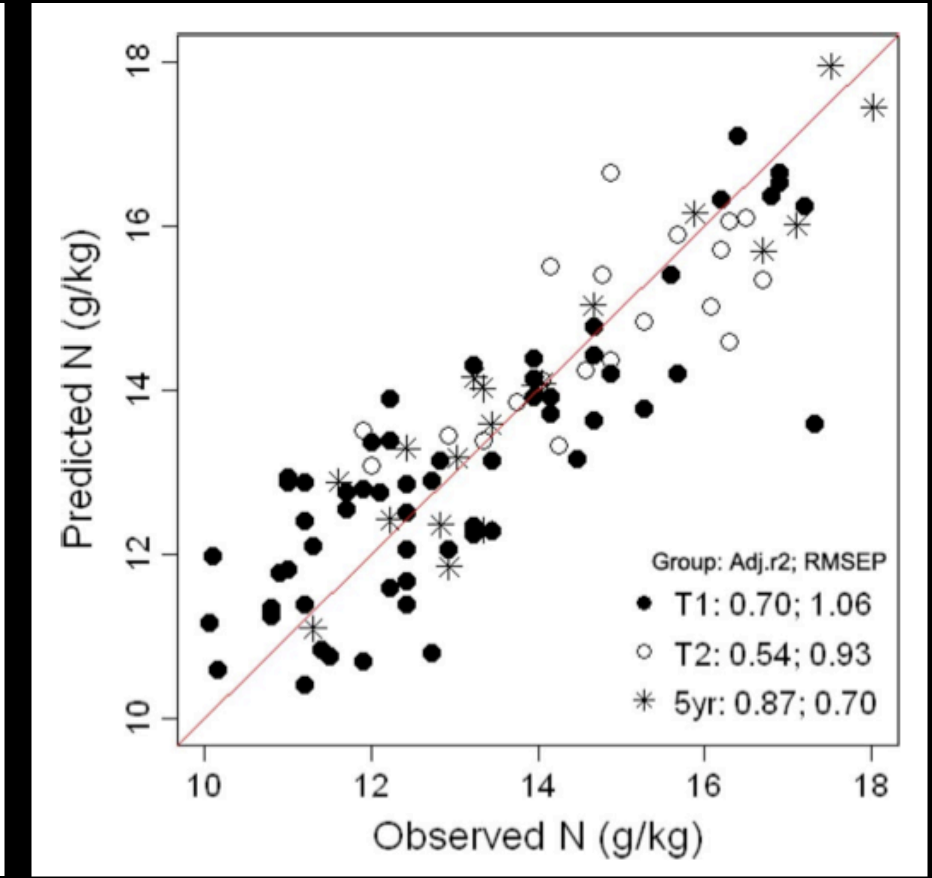

Predicted versus observed N concentration for models calibrated and validated on individual age class plot groups (T1, T2 and 5 yr). Cross validated model fit statistics for each age class are shown. All models are significant at $P < 0.001$.

Sims, et al. JSTARS 2013

Predicted Nitrogen concentration levels in South Australian P. radiata trees. Extrapolating the model across the estate provided predictions for N concentrations between 8 g/kg and 22 g/kg with defined spatial regions of high and low concentration levels. This map supported the field data and indicated that N was frequently marginal or deficient throughout the estate.

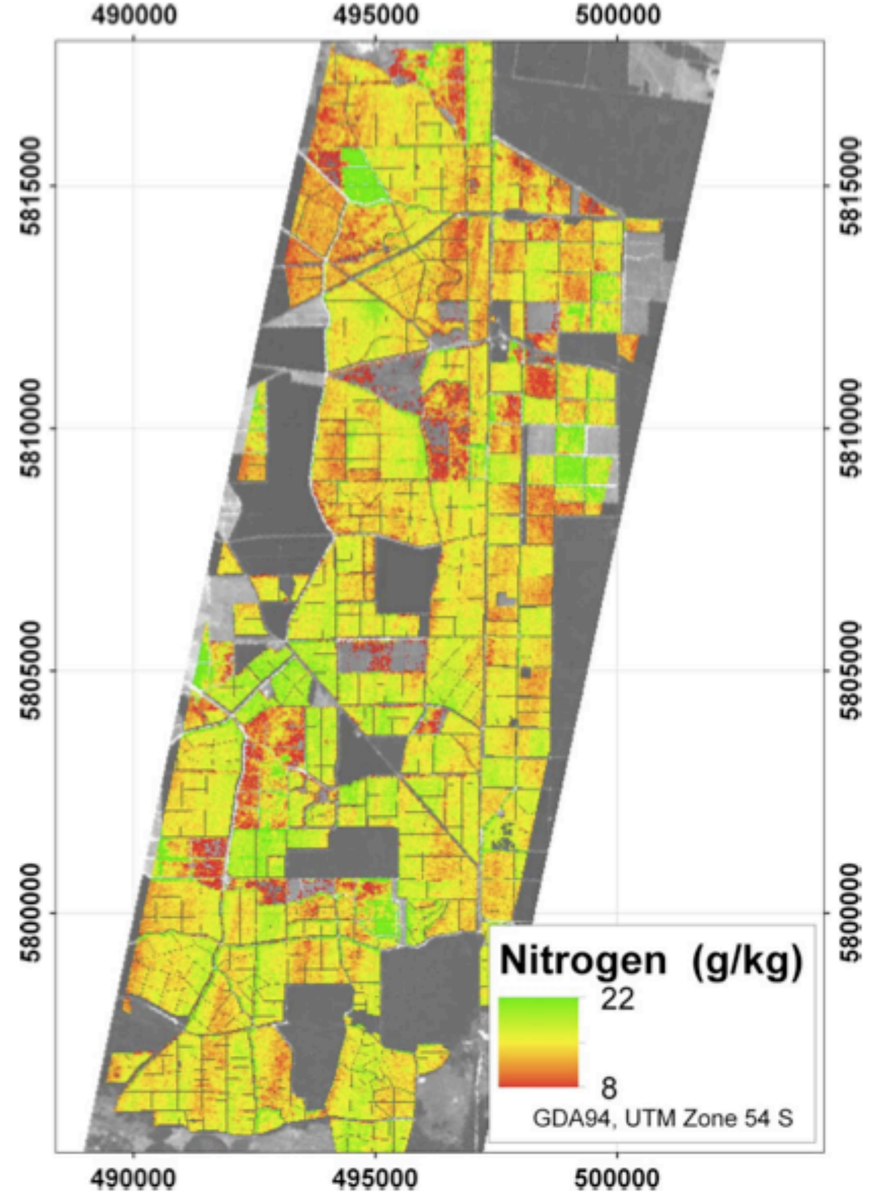

JSTARS EO-1 Special Issue

Unmixing Analysis of a Time Series of Hyperion Images Over the Guánica Dry Forest in Puerto Rico

Miguel A. Goenaga, Maria C. Torres-Madronero, Miguel Velez-Reyes, Skip J. Van Bloem, and Jesus D. Chinea

Abstract — This paper presents the analysis of a time series of hyperspectral images collected with the Hyperion sensor on board EO-1 to demonstrate how hyperspectral imaging can be used for studying seasonal variations of vegetation cover over the Guánica Dry Forest in Puerto Rico. The approach is based on a local unmixing procedure that splits the hyperspectral scene into tiles and performs endmember extraction on each tile. The main assumption is that within a tile, a single spectral signature is an adequate representation of an endmember. Local endmember signatures from each tile are then clustered to extract endmember classes that better account for endmember spectral variability across the scene and provide a better global description of the full forest scene. Within a scene, abundances are computed using all extracted spectral endmembers and the abundance of an endmember class is computed as the sum of the abundances for the spectral endmembers belonging to that class. Variations in abundance maps are used to understand seasonal changes in forest cover. The procedure was performed using eleven near-cloud-free Hyperion images collected in different months in 2008. Results from the analysis agreed with published knowledge of the phenological changes for this forest. Correlation analyses with NDVI and rainfall time series are used to understand variations in coverage of certain endmember classes with weather. Mangrove was shown to be uncorrelated with rainfall, whereas the upland forest endmember was highly correlated with rain. This study shows the potential for unmixing methods to exploit hyperspectral data for temporal analysis.

Goenaga, et al. JSTARS 2013

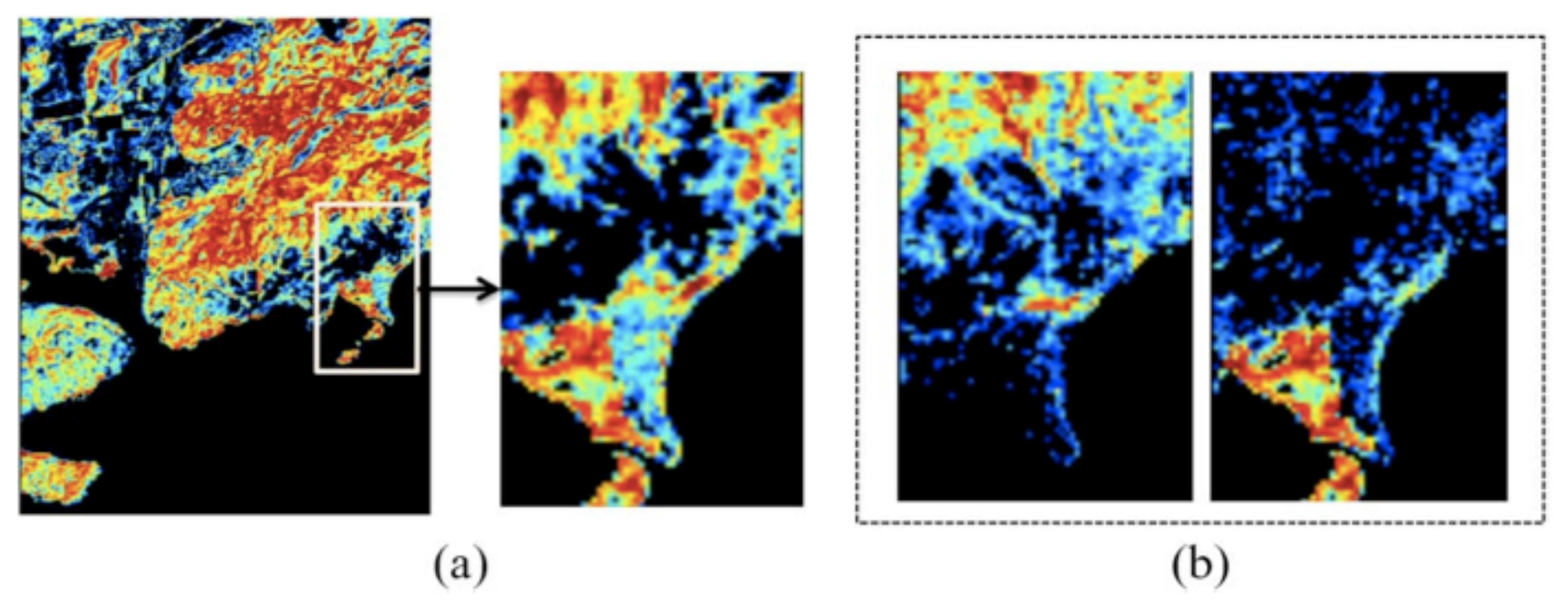

Estimated abundances for forest vegetation and mangrove using (a) a global approach, and (b) a local approach (which separates the two classes).

Goenaga, et al. JSTARS 2013

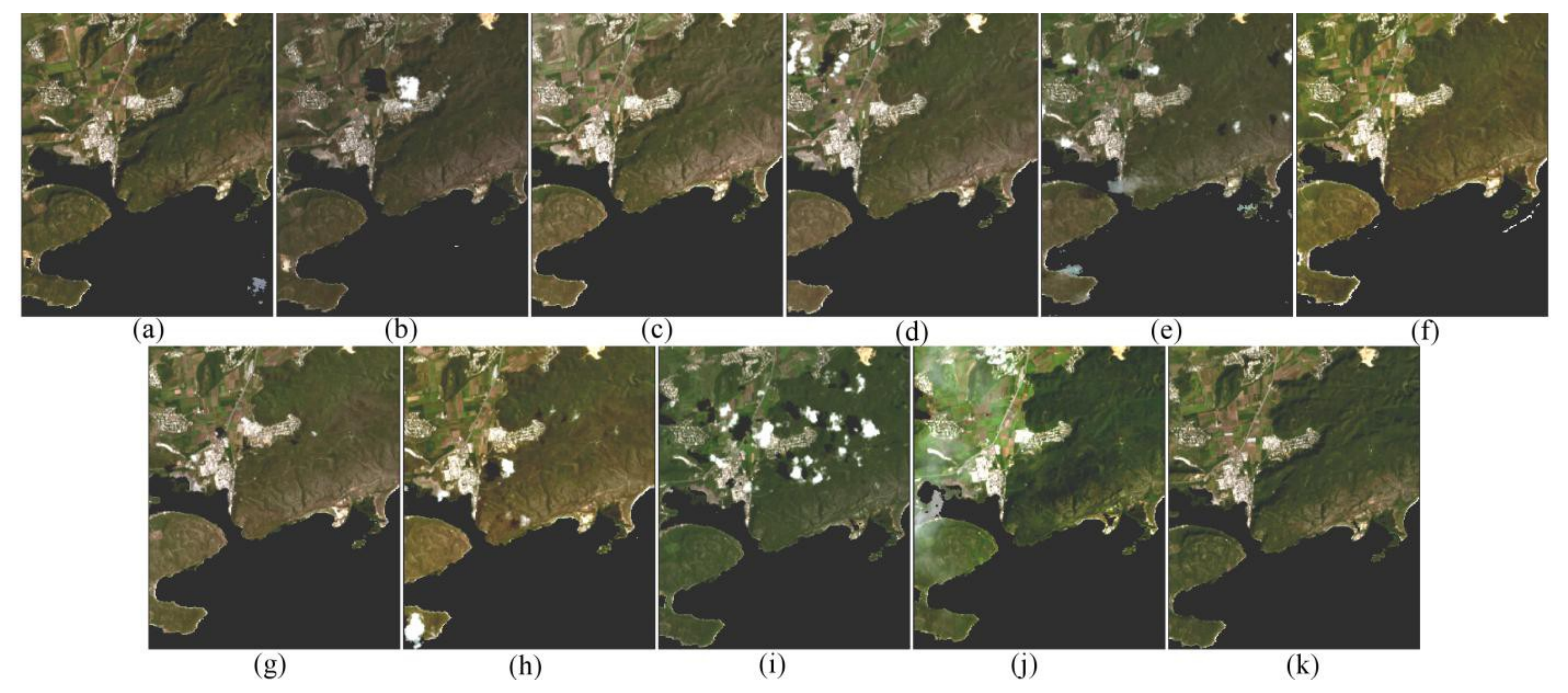

Hyperion collected 63 images with minimal cloud cover over some portion of Guánica Forest from 2004 to 2010. The scenes were subset to 256 x 308 pixels images corresponding to the area over the Guánica Forest. These true color composites were collected in 2008: (a) Feb.4 (b) Mar.21 (c) Mar.26 (d) Apr.18 (e) May 6 (f) Jun.21 (g) Jul.14 (h) Aug.6 (i) Sep.16 (j) Oct.9 (k) Dec. 12. The color composites were created using bands 29 (640.5nm), 20 (548.9nm), and 14 (487.87nm).

Goenaga, et al. JSTARS 2013

Forest vegetation class abundances tracked seasonal changes in rainfall – decreasing from February to March, increasing from April to May, and decreasing from June to August.

These changes are shown in NDVI and abundance maps for endmember classes: forest vegetation, mangroves, rocky outcrops, crops (vegetation), crops (soil), and buildings.

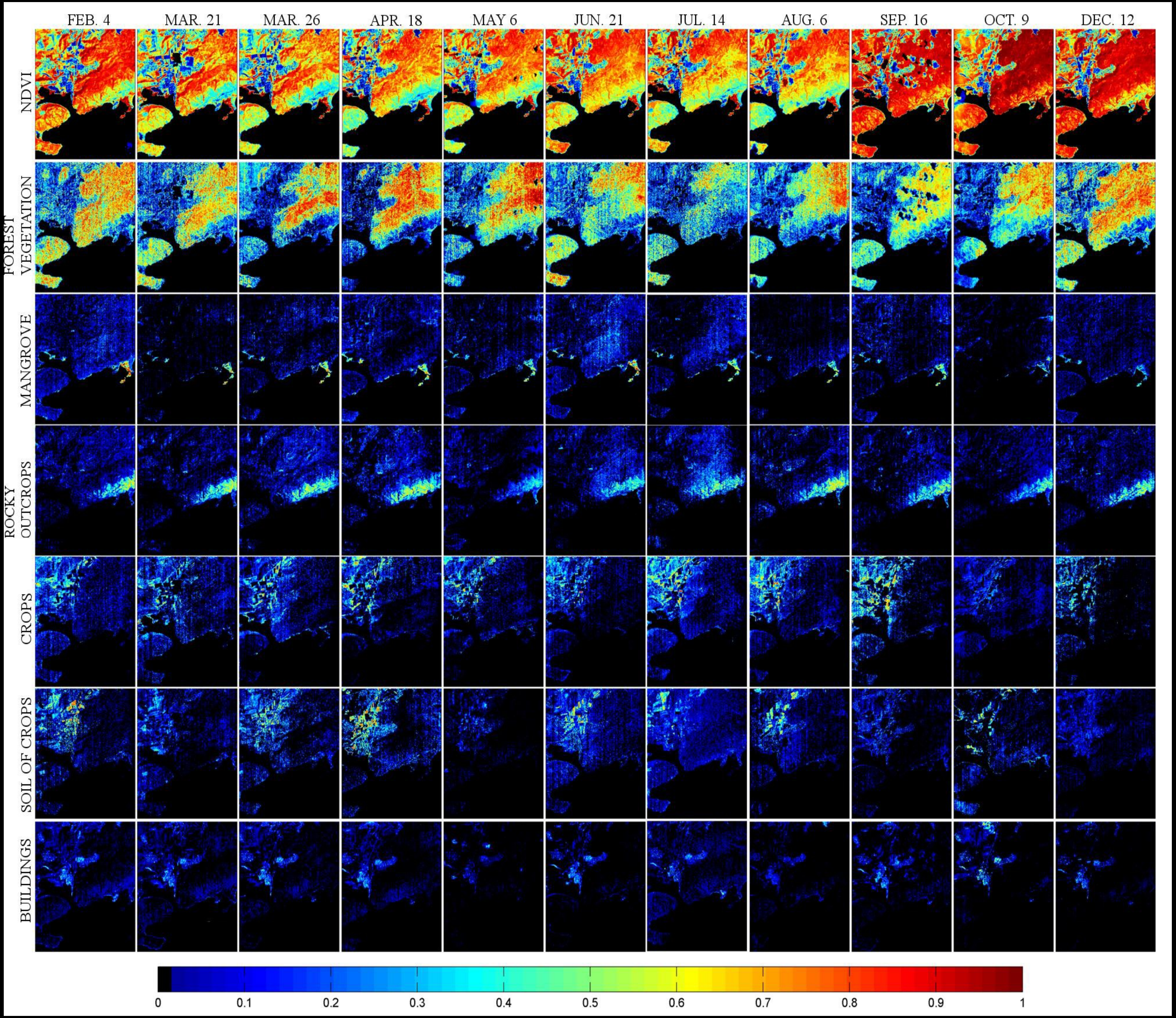

Goenaga, et al. JSTARS 2013

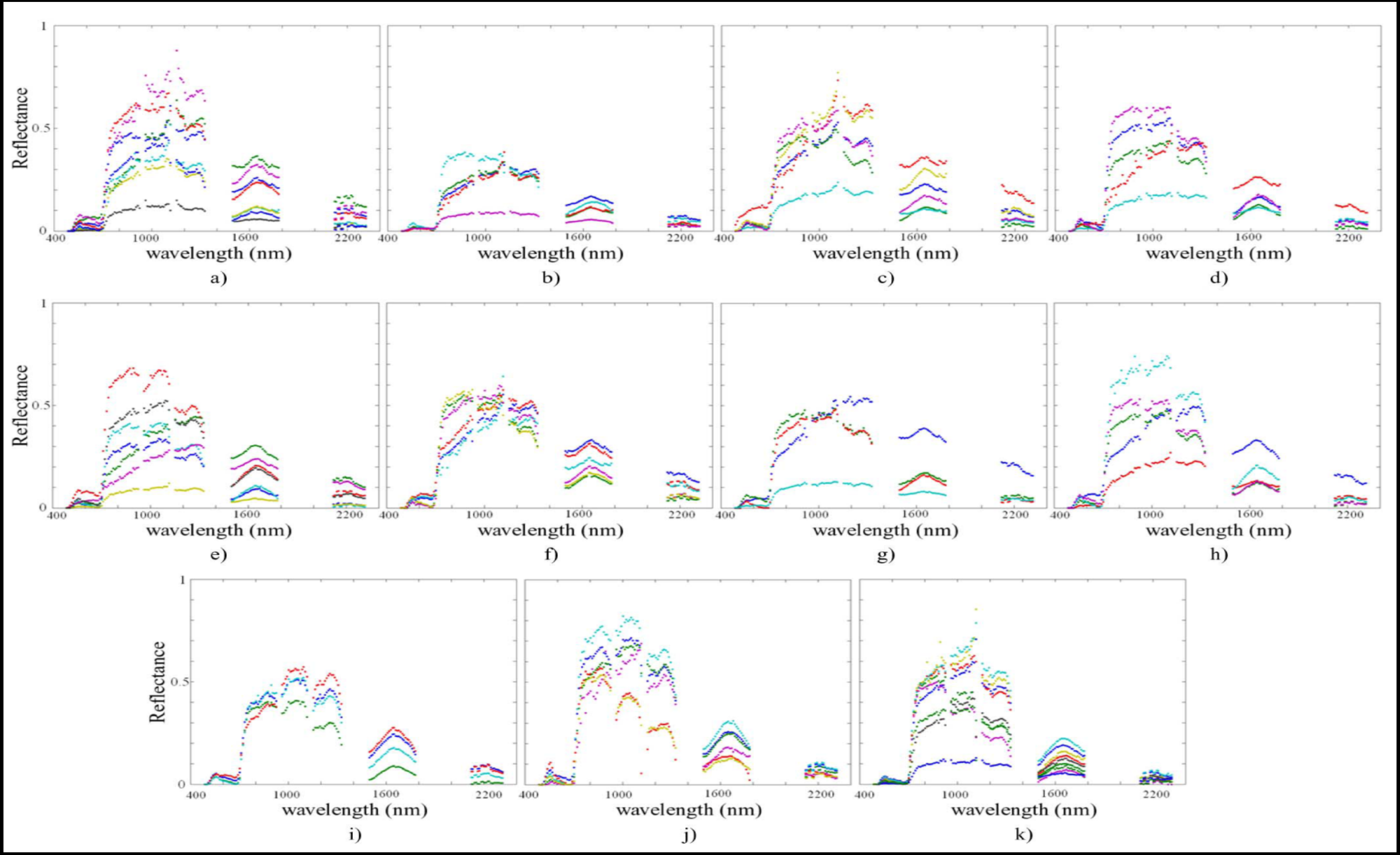

Spectra from Hyperion of the forest vegetation endmember class for the eleven 2008 dates: (a) Feb. 4 (b) Mar. 21 (c) Mar. 26 (d) Apr. 18 (e) May 6 (f) Jun. 21 (g) Jul. 14 (h) Aug. 6 (i) Sep. 16 (j) Oct. 9 (k) Dec. 12.

Goenaga, et al. JSTARS 2013

Top: Hyperion spectra of mangrove endmember classes for different dates for 11 days in 2008. [Note: b next to the dates means that another sample was acquired later that day].

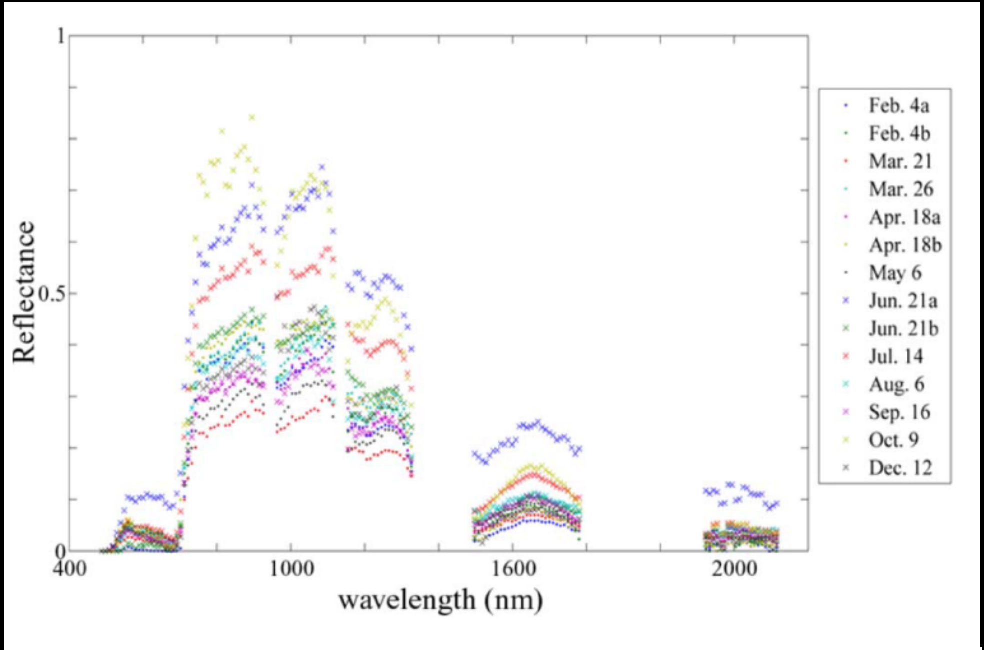

Bottom: Hyperion spectra of the rocky outcrop endmember class for the eleven dates in 2008.

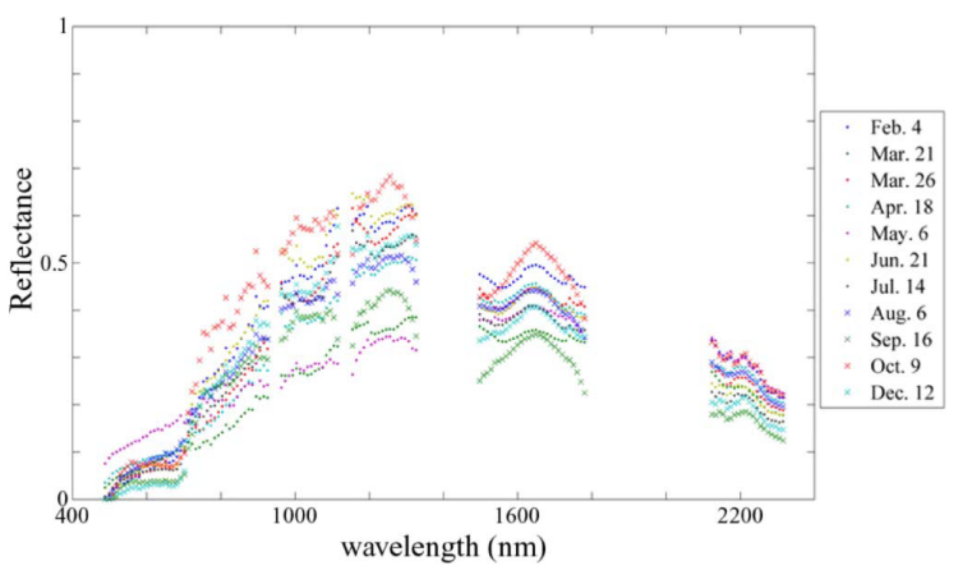

Goenaga, et al. JSTARS 2013

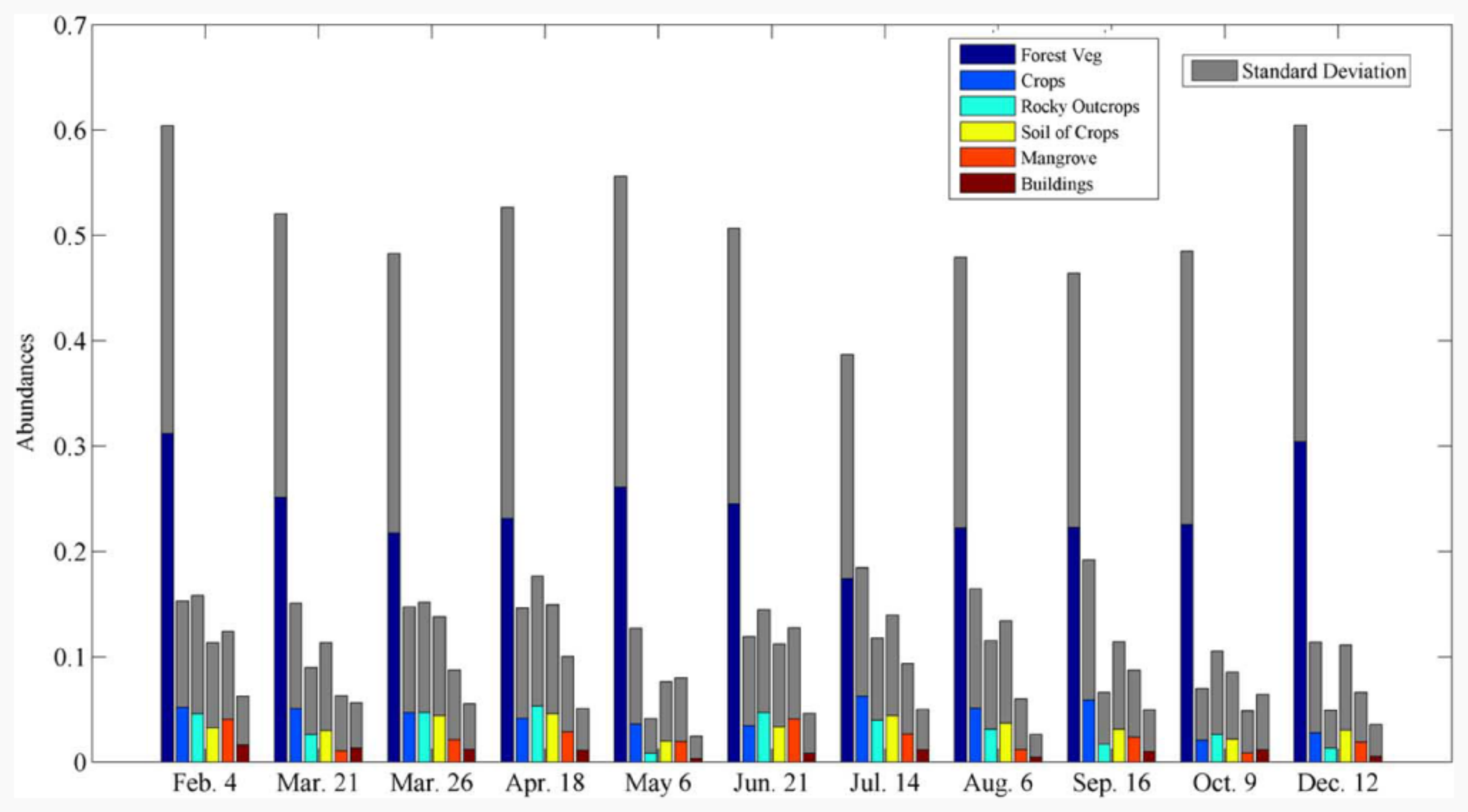

Global mean and standard deviation for the six endmember classes. Color bars correspond to the mean abundances and gray bars show the standard deviations.

Goenaga, et al. JSTARS 2013

Correlation between the forest endmember (a-c) and mangrove (d-f) classes abundance time-series for each pixel and (a,d) 7 days rainfall average before acquisition date; (b,e) 30 days rainfall average before acquisition date; and (c,d) NDVI value for each pixel.

Unlike NDVI, the abundance maps are able to provide more temporal variability information in the different regions. Mangrove behavior appears to be independent of the seasonal rainfall. Spectral signatures of rocky outcrops, mangrove, and buildings showed very little annual variation. We would expect major changes to mangrove signatures only after major storm (e.g., hurricane) or drought events.

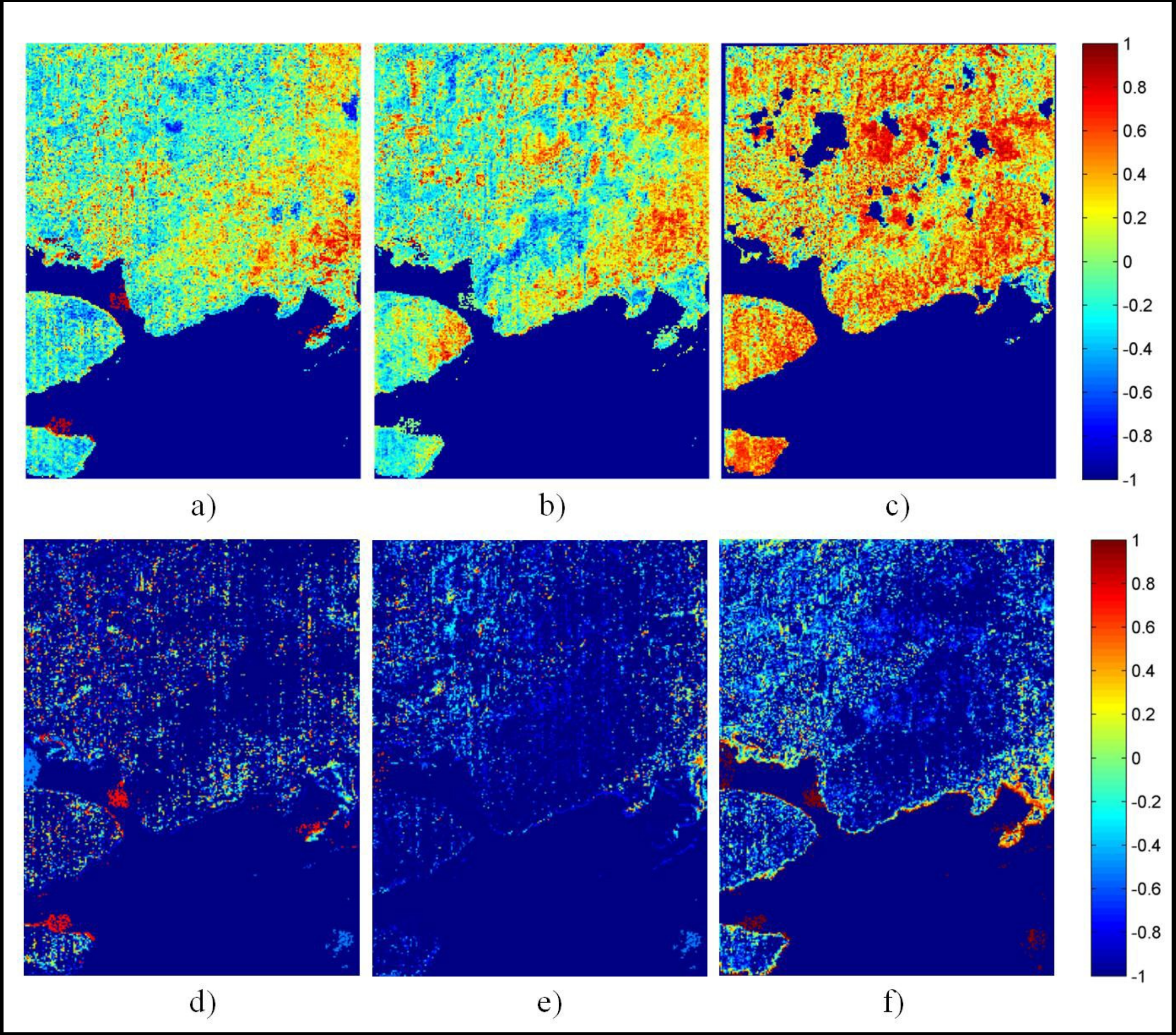

a) b) c)

d) e) f)

JSTARS EO-1 Special Issue

Seasonal Variation in Spectral Signatures of Five Genera of Rainforest Trees

Monica Papes, Raul Tupayachi, Paola Martínez, A. Townsend Peterson, Gregory P. Asner, and George V. N. Powell

Abstract — Recent technological and methodological advances in the field of imaging spectroscopy (or hyperspectral imaging) make possible new approaches to studying regional ecosystem processes and structure. We use Earth Observing-1 Hyperion satellite hyperspectral imagery to test our ability to identify tree species in a lowland Peruvian Amazon forest, and to investigate seasonal variation in species detections related to phenology. We obtained four images from 2006–2008, and used them to spectrally differentiate crowns of 42 individual trees of 5 taxa using linear discriminant analysis. Temporal variation of tree spectra was assessed using three methods, based on 1) position of spectra in a two-dimensional canonical variable space, 2) a broadband, multispectral dataset derived from sets of narrow bands identified as informative to spectrally separate taxa, and 3) narrow band vegetation indices (photochemical reflectance index and anthocyanin reflectance index) sensitive to leaf pigments. We obtained high classification success with a reduced set of trees (28 individuals) whose crowns were well represented on Hyperion 30 m resolution pixels. Temporal variability of spectra was confirmed by each of the three methods employed. Understanding seasonality of spectral characteristics of tropical tree crowns has implications in spectral based multi-seasonal species mapping and studying ecosystem processes.

Papes, et al. JSTARS 2013

The location of the study area in southeastern Peru (12.544S, 0.0611W) and the area where trees were sampled along a trail system (displayed with a Quickbird image) are shown. The four Hyperion datasets analyzed are inserted as composite images (R:650 nm, G:847 nm, and B:548 nm bands). The four datasets are: t1 = 20 July 2006; t2 = 19 Nov 2007; t3 = 29 Dec 2006; and t4 = 21 May 2008.

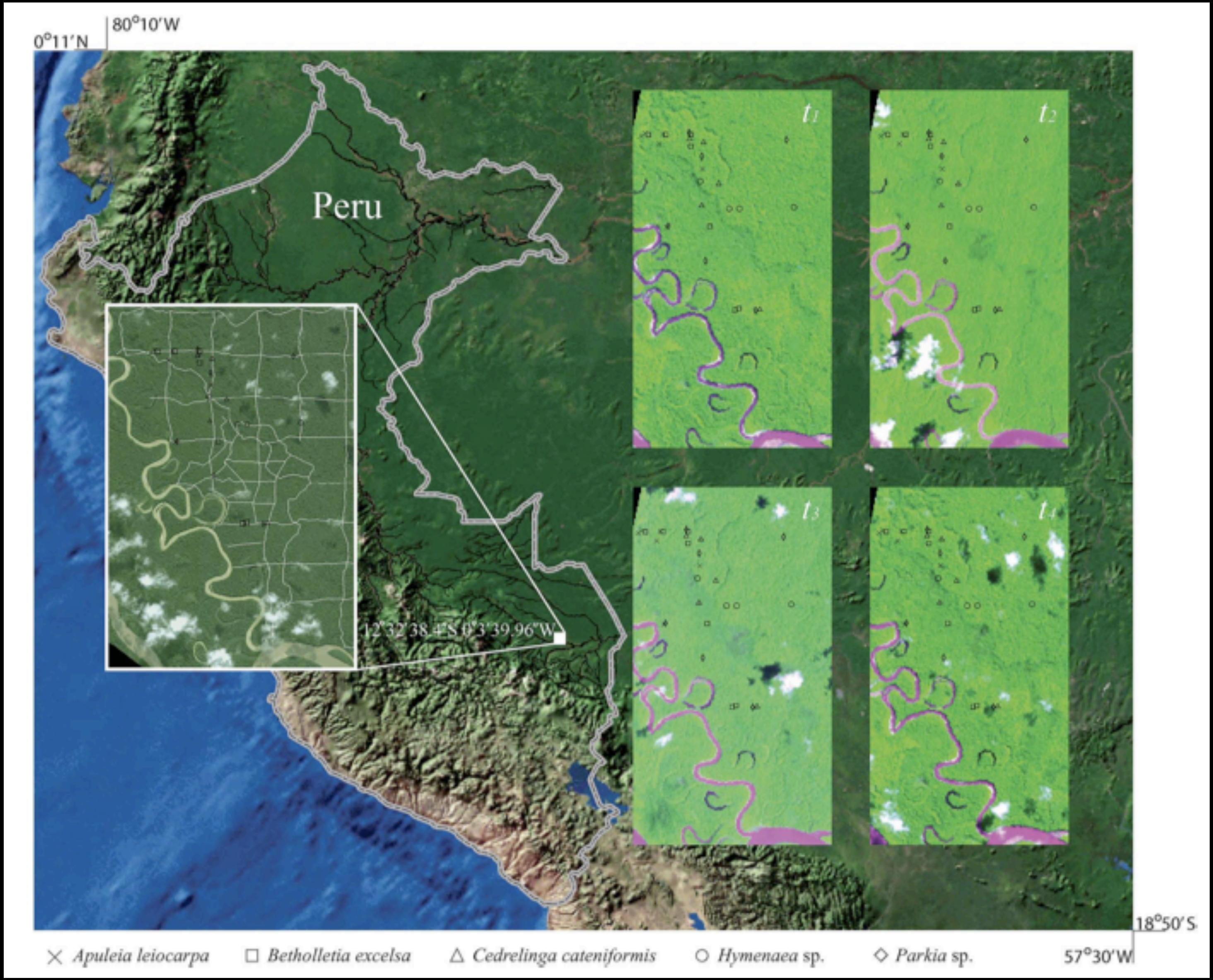

Papes, et al. JSTARS 2013

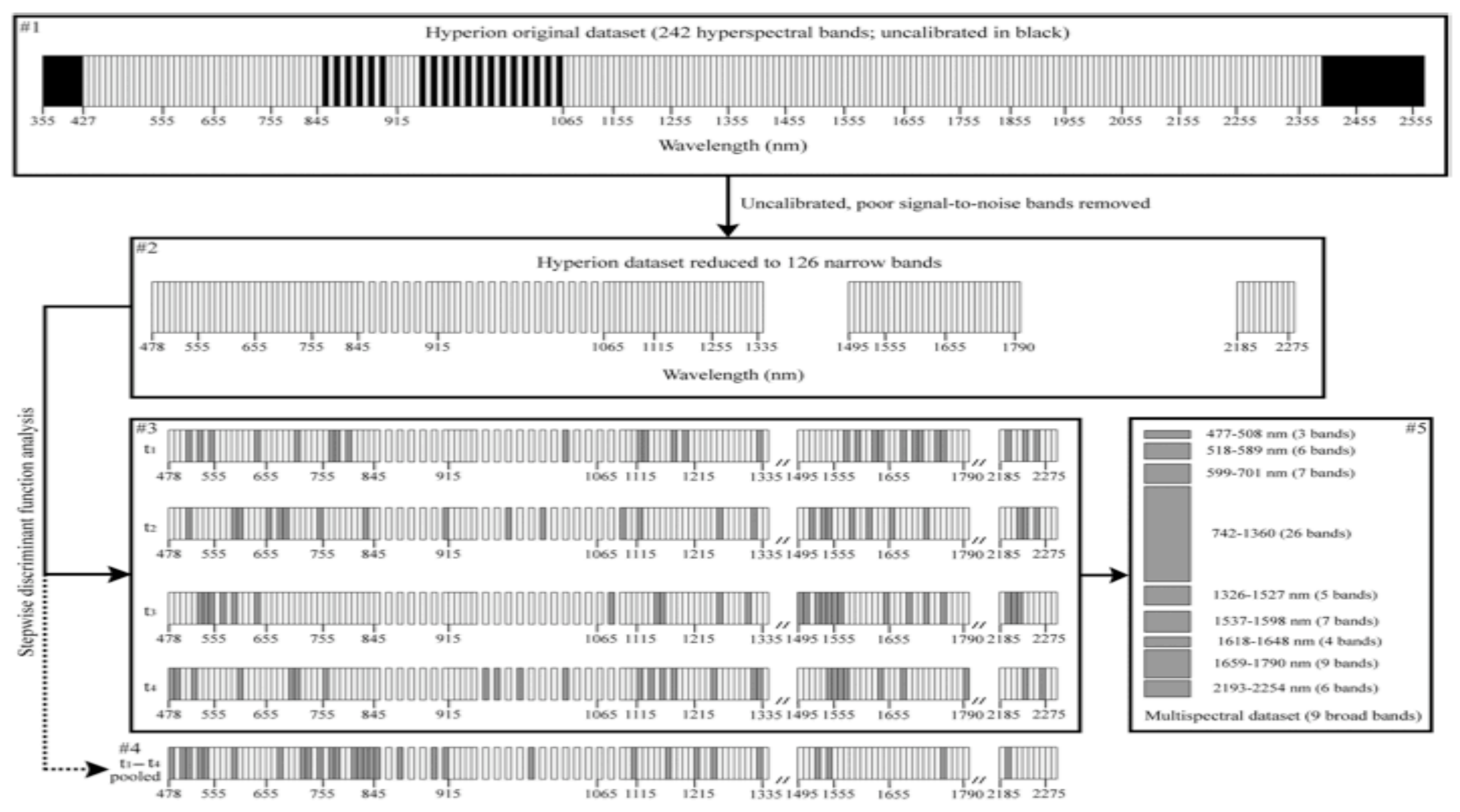

Summary of selection of Hyperion narrow bands, with bands removed from analyses in black and bands retained in gray (panel 1: original Hyperion dataset). Panel 2 shows 126 narrow bands remaining after removal of uncalibrated bands. Panel 3 shows the channels used in separate linear discriminant analyses for each season (t1 - t4). Selection of narrow bands when t1 - t4 datasets are pooled is shown in panel 4. Panel 5 presents the combination of channels used to simulate 9 multispectral bands.

Papes, et al. JSTARS 2013

Temporal spectral variation observed in canonical variable space: (A) representation of t1 - t4 datasets and all (28) individual trees, showing separation through time, not by taxon (symbols as in Fig. 3); (B) a random sample of Hyperion pixels falling in forested areas (see Fig. 1), also grouped by time.

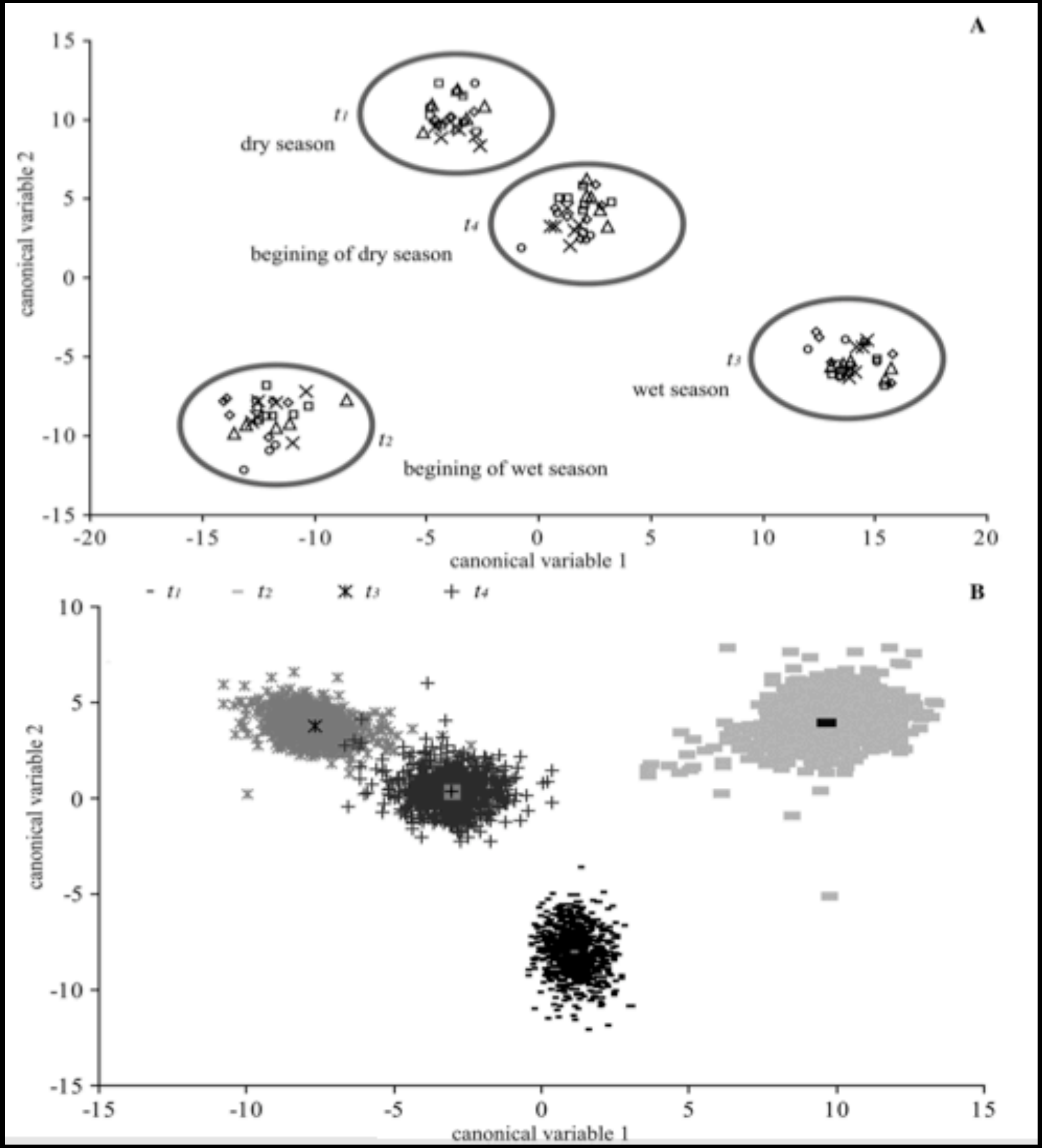

Papes, et al. JSTARS 2013

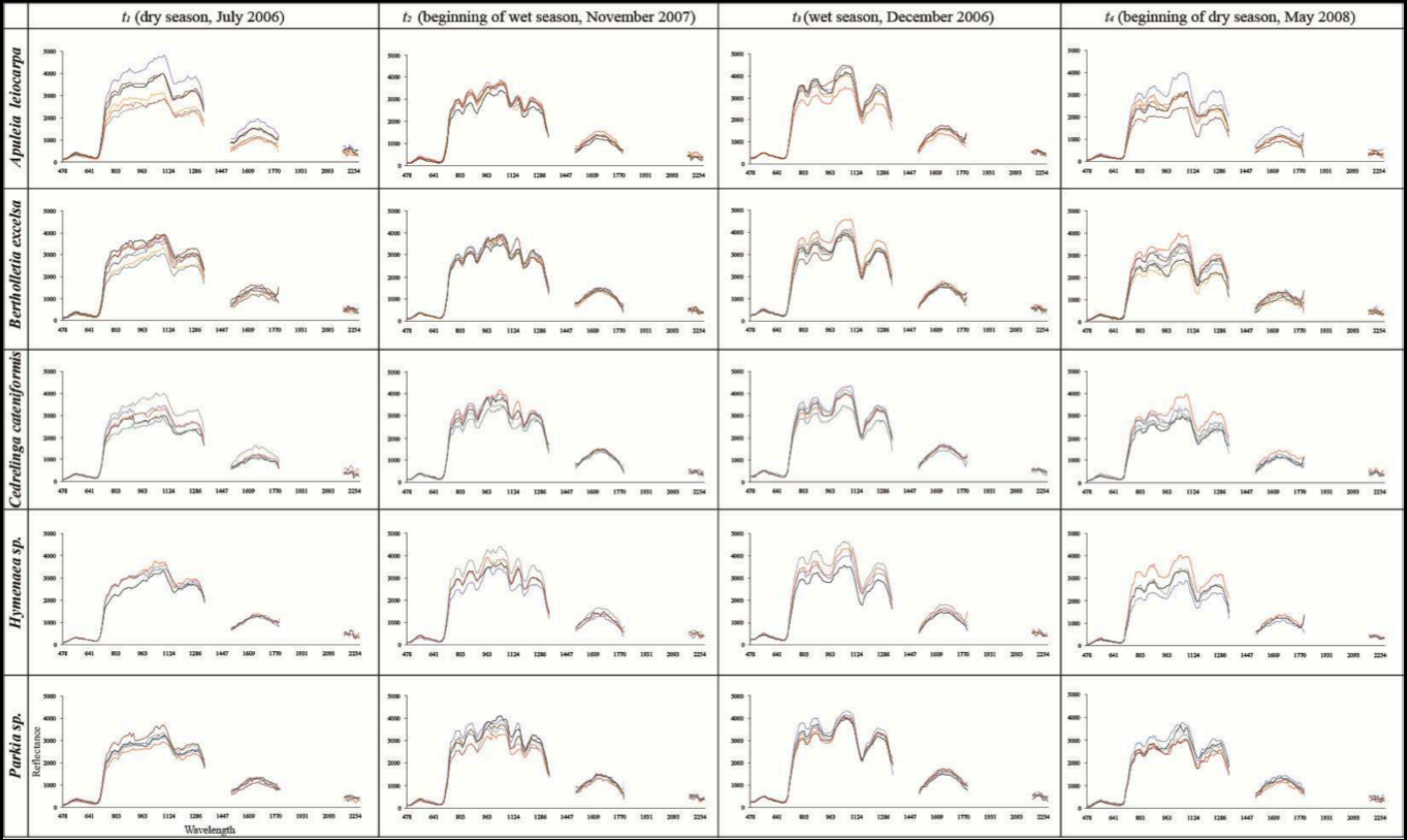

Spectra of tree crowns of the 5 Peruvian tree taxa studied (screened dataset shown only) at the 4 times examined (t1 - t4), with uncalibrated Hyperion bands removed; colors represent different individuals of the same taxon. Apparent reflectance values were scaled from floating point into integer values using a 10,000 scale factor.

JSTARS EO-1 Special Issue

Invasive Species Mapping in Hawaiian Rainforests Using Multi-Temporal Hyperion Spaceborne Imaging Spectroscopy

Ben Somers and Gregory P. Asner

Abstract — We evaluated the potential of multi-temporal Multiple Endmember Spectral Mixture Analysis (MESMA) of Earth Observing-1 Hyperion data for detection of invasive tree species in the montane rainforest area of the Hawaii Volcanoes National Park, Island of Hawaii. We observed a clear seasonal trend in invasive species detection success when unmixing results were cross-referenced to ground observations; with Kappa coefficients (indicating detection success, 0–1) ranging between 0.66 (summer) and 0.69 (winter) and 0.51–0.53 during seasonal transition periods. An increase of Kappa to 0.80 was observed when spectral features extracted from September, August and January were integrated into MESMA. Multi-temporal unmixing improved the detection success of invasive species because spectral information acquired over different portions of the growing season allowed us to capture species-specific phenology, thereby reducing spectral similarity among species.

JSTARS EO-1 Special Issue

Invasive Species Mapping in Hawaiian Rainforests Using Multi-Temporal Hyperion Spaceborne Imaging Spectroscopy

Ben Somers and Gregory P. Asner

Abstract — We evaluated the potential of multi-temporal Multiple Endmember Spectral Mixture Analysis (MESMA) of Earth Observing-1 Hyperion data for detection of invasive tree species in the montane rainforest area of the Hawaii Volcanoes National Park, Island of Hawaii. We observed a clear seasonal trend in invasive species detection success when unmixing results were cross-referenced to ground observations; with Kappa coefficients (indicating detection success, 0–1) ranging between 0.66 (summer) and 0.69 (winter) and 0.51–0.53 during seasonal transition periods. An increase of Kappa to 0.80 was observed when spectral features extracted from September, August and January were integrated into MESMA. **Multi-temporal unmixing improved the detection success of invasive species because spectral information acquired over different portions of the growing season allowed us to capture species-specific phenology, thereby reducing spectral similarity among species.**

Somers, et al. JSTARS 2013

(Top) Overview of the Hawaii Volcanoes National Park on the Island of Hawaii (imagery from the Carnegie Airborne Observatory);

(Bottom) Detail of the native ohia (Metrosideros) forests. Although most of this area is under protection by the U.S. National Park Service, it has experienced a number of biological invasions, predominantly by Morella faya.

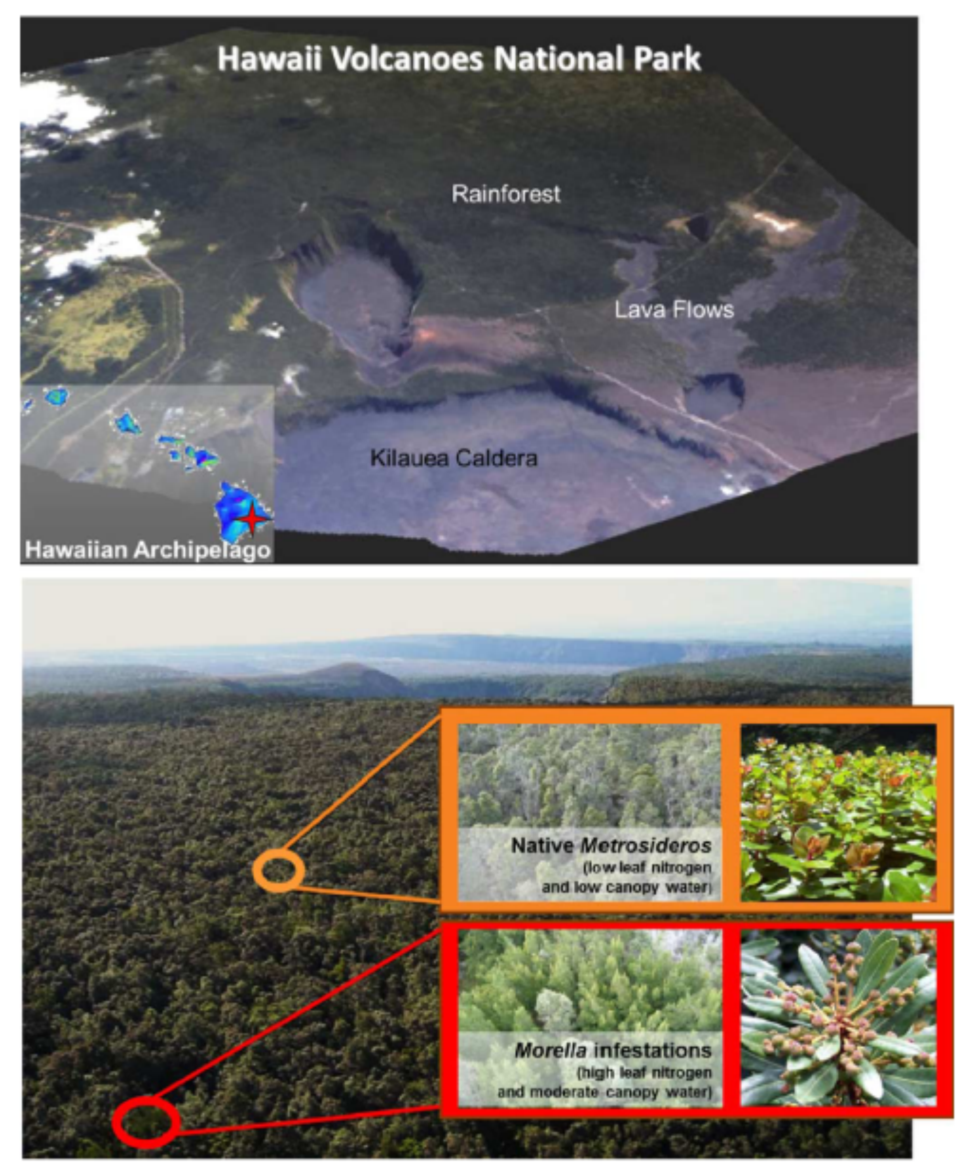

Somers, et al. JSTARS 2013

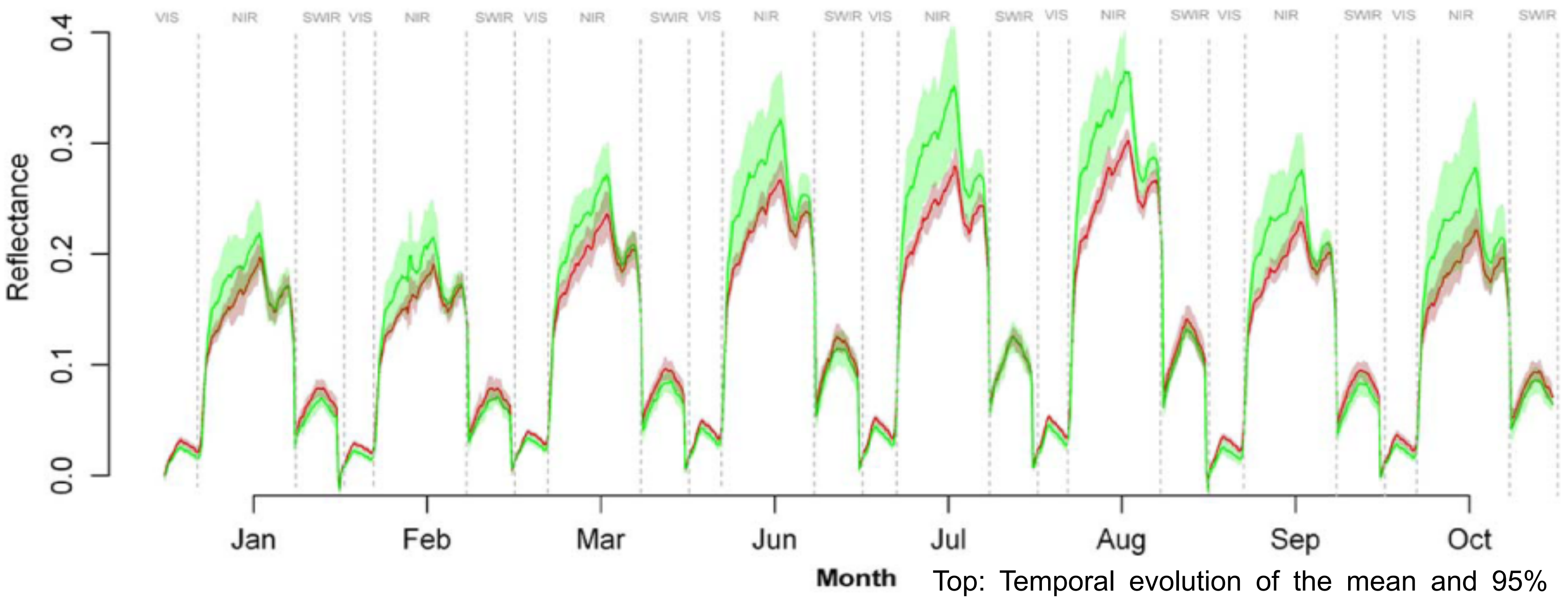

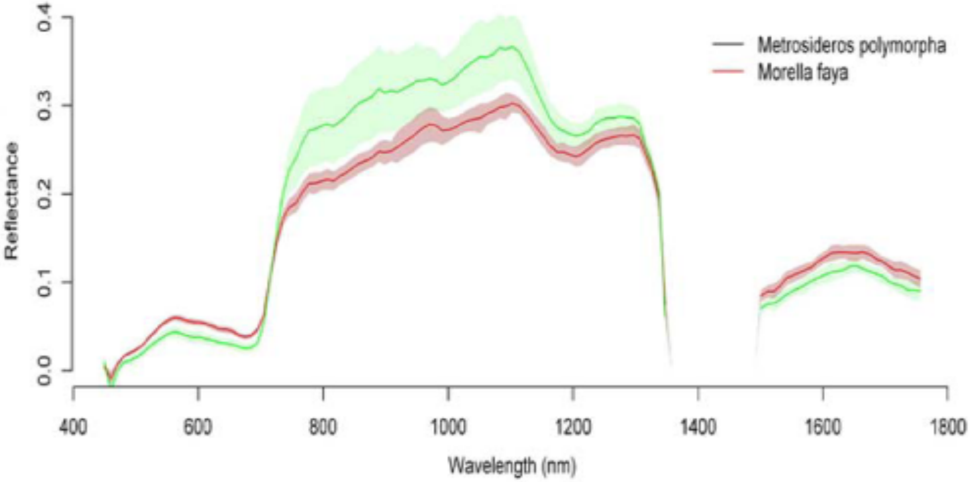

Top: Temporal evolution of the mean and 95% confidence interval of the native Metrosideros (darker line and shading) and invader Morella (lighter line and shading) endmember libraries. Spectra are shown for eight months, each of which display the VIS, NIR, and SWIR1 wavelengths (400–1800 nm).

Bottom: Composite spectral profile showing maximum separability between both endmember classes. The composite spectrum is composed of spectral information from September (VIS), August (NIR1, NIR2) and January (SWIR1), all of which had the lowest InStability Index (ISI) per spectral region and month.

Somers, et al. JSTARS 2013

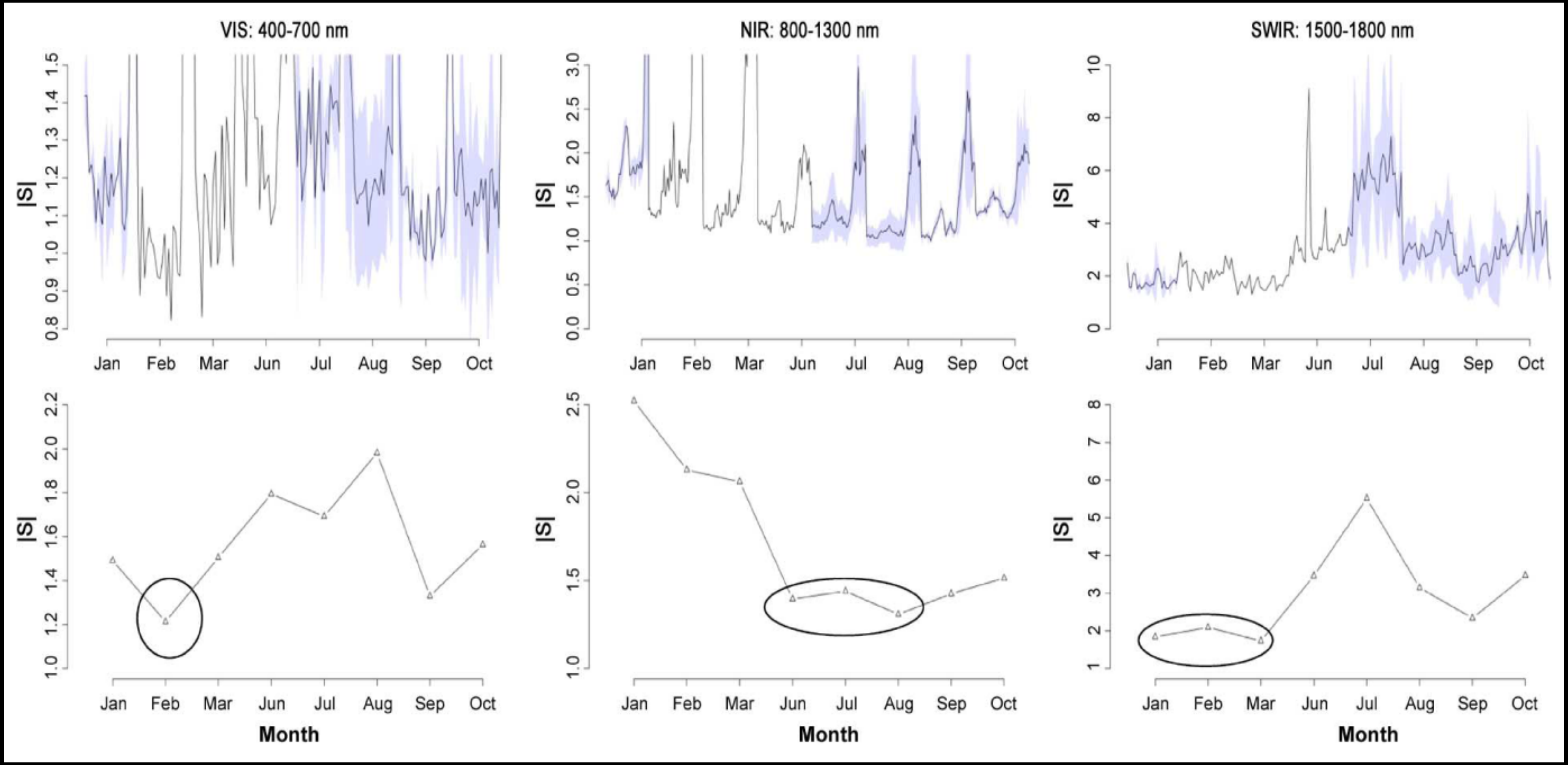

Temporal evolution of ISI for VIS, NIR and SWIR1. Results are compiled from the time series of species specific endmember libraries as extracted from the 18 cloud-free images. While the top panels show the wavelength specific monthly means and 95% confidence interval, the bottom panels show the overall monthly means for the entire VIS (left), NIR (middle) and SWIR1 (right) domains. The months having the lowest InStability Index (ISI) (i.e., best discrimination) are circled.

Somers, et al. JSTARS 2013

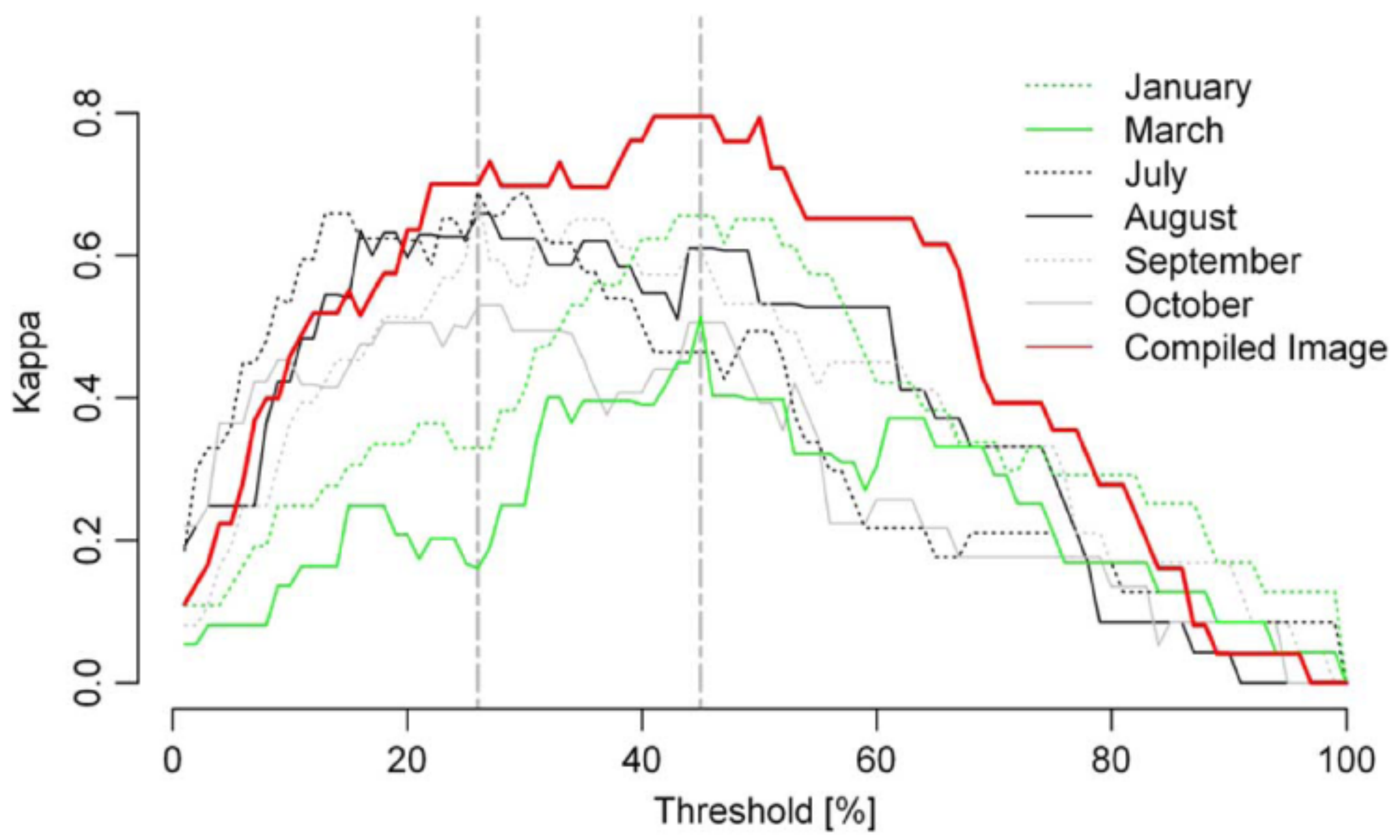

The seasonal trends in the success of detecting Morella invasion, expressed as the Cohen's Kappa coefficient, as a function of the MESMA classification threshold, are shown for each month, as well as for the composite image from September (VIS), August (NIR1, NIR2) and January (SWIR1). The vertical dotted lines indicate the maximum Kappa values for thresholds of 45% (obtained in January/March) and 25% (obtained in July/August/September/October).

Somers, et al. JSTARS 2013

InStability Index (ISI) spectra for the VIS, NIR1, NIR2, and SWIR1.

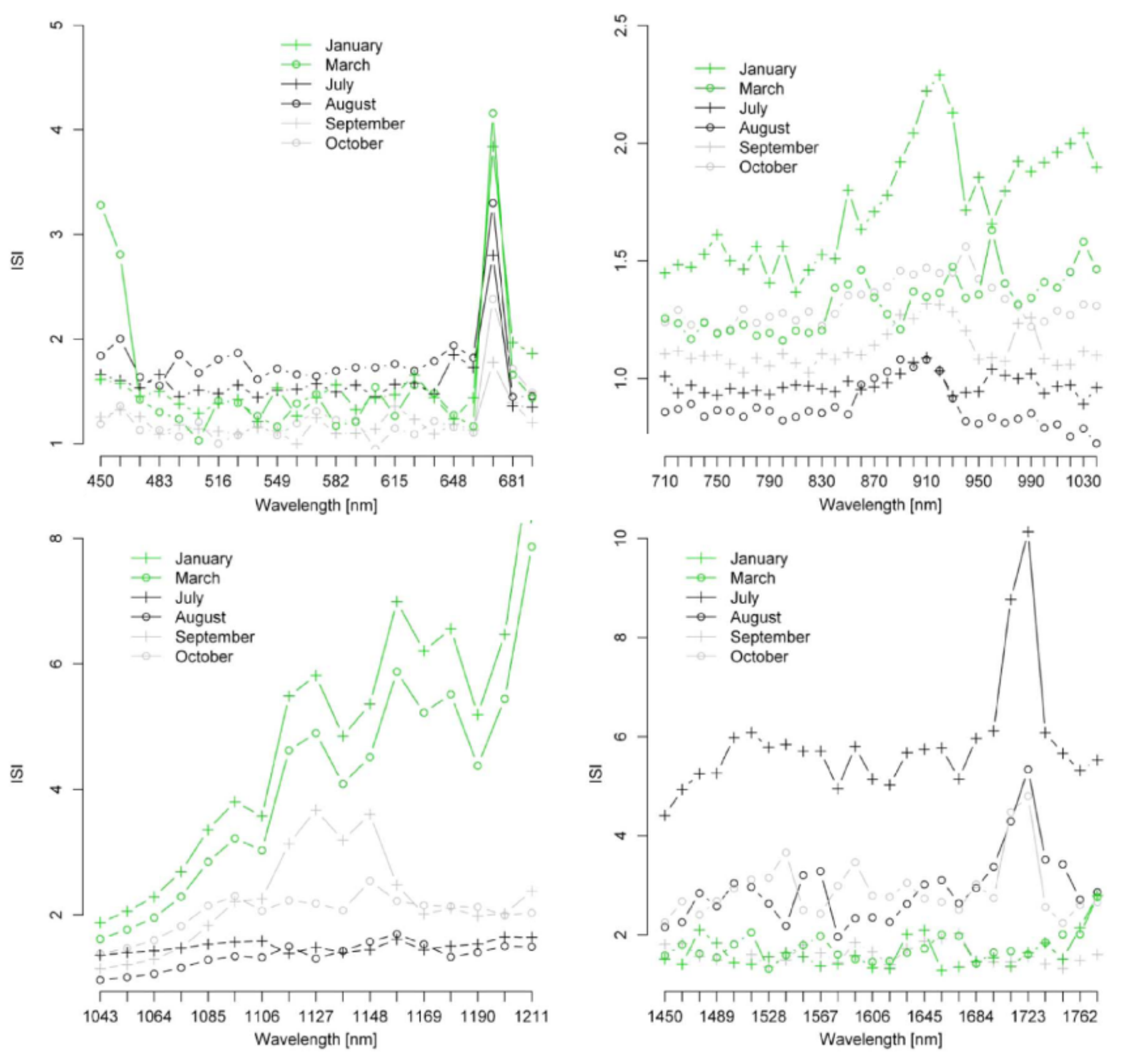

JSTARS EO-1 Special Issue

Leveraging EO-1 to Evaluate Capability of New Generation of Landsat Sensors for Coastal/Inland Water Studies

Nima Pahlevan and John R. Schott

Abstract — Monitoring coastal and inland waters, recognized as case II waters, using the existing Landsat technology is somewhat restricted because of its low signal-to-noise ratio (SNR) and its relatively poor radiometric resolution. The new generation of Landsat, Landsat Data Continuity Mission (LDCM) carrying the Operational Land Imager (OLI), has enhanced features allowing for a more lucid characterization of water constituents in either coastal or inland waters with respect to Landsat-7 (ETM+). This paper applies a physics-based approach to fully examine the potential of OLI in terms of its enhanced features in a water constituent retrieval framework. An EO-1 dataset, including Hyperion and the Advanced Land Imager (ALI), together with nearly coincident ETM+ imagery were atmospherically corrected using a data-driven approach. An in-water radiative transfer model, i.e., Hydrolight, was applied to generate a Look-Up-Table (LUT) of simulated surface reflectances for various combinations of water constituents. Using the Hyperion-derived concentration maps as validation sources, it was found that the simulated OLI imagery is superior to ETM+ on the order of 40%, 20%, and 28% when retrieving the concentrations of chlorophyll-a and total suspended solids (TSS), as well as the absorption of the colored dissolved organic matter (CDOM), respectively. It was also demonstrated that the simulated OLI imagery outperforms the simulated ALI and the recorded ALI datasets in the retrieval of chlorophyll-a and CDOM absorption. It is concluded that the new generation of Landsat enables mapping and monitoring of case II waters with accuracies not achieved with the previous Landsat satellite series.

Pahlevan, et al. JSTARS 2013

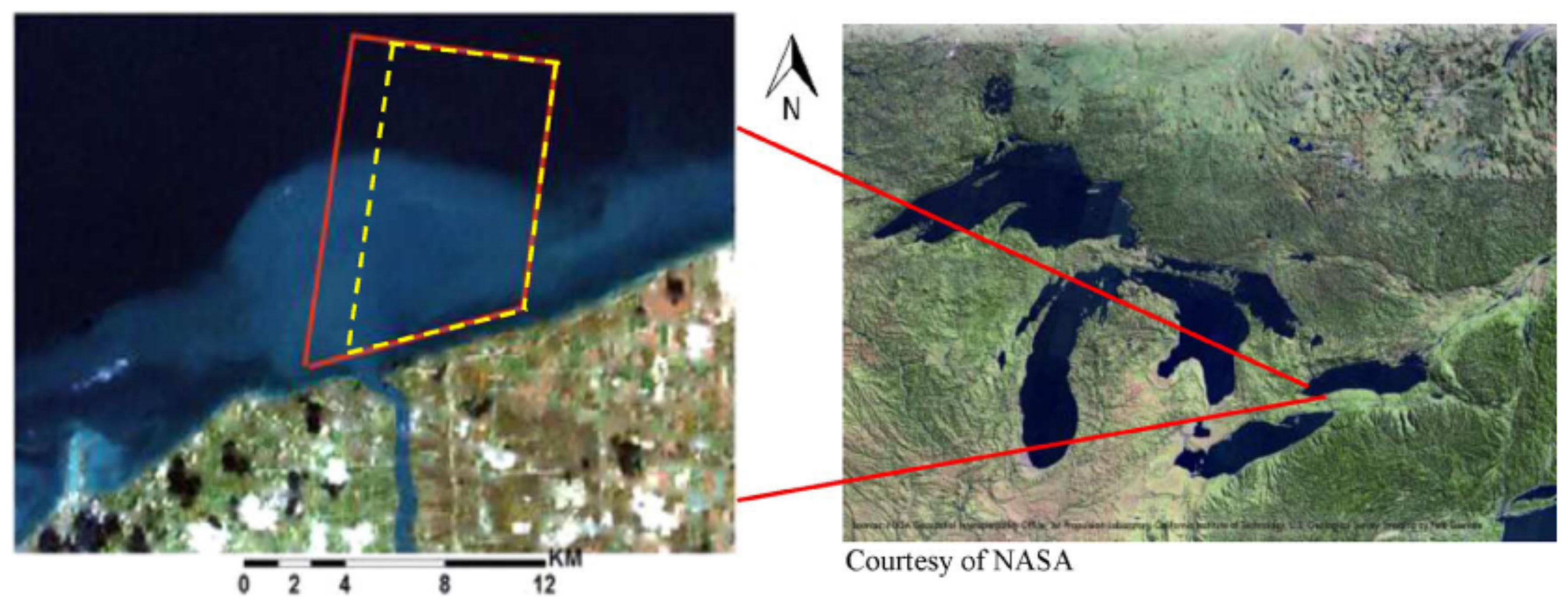

Courtesy of NASA

Study area covering the Niagara River plume (left) discharging into the western basin of Lake Ontario. The red box (≈100 km2) indicates the ROI.

Pahlevan, et al. JSTARS 2013

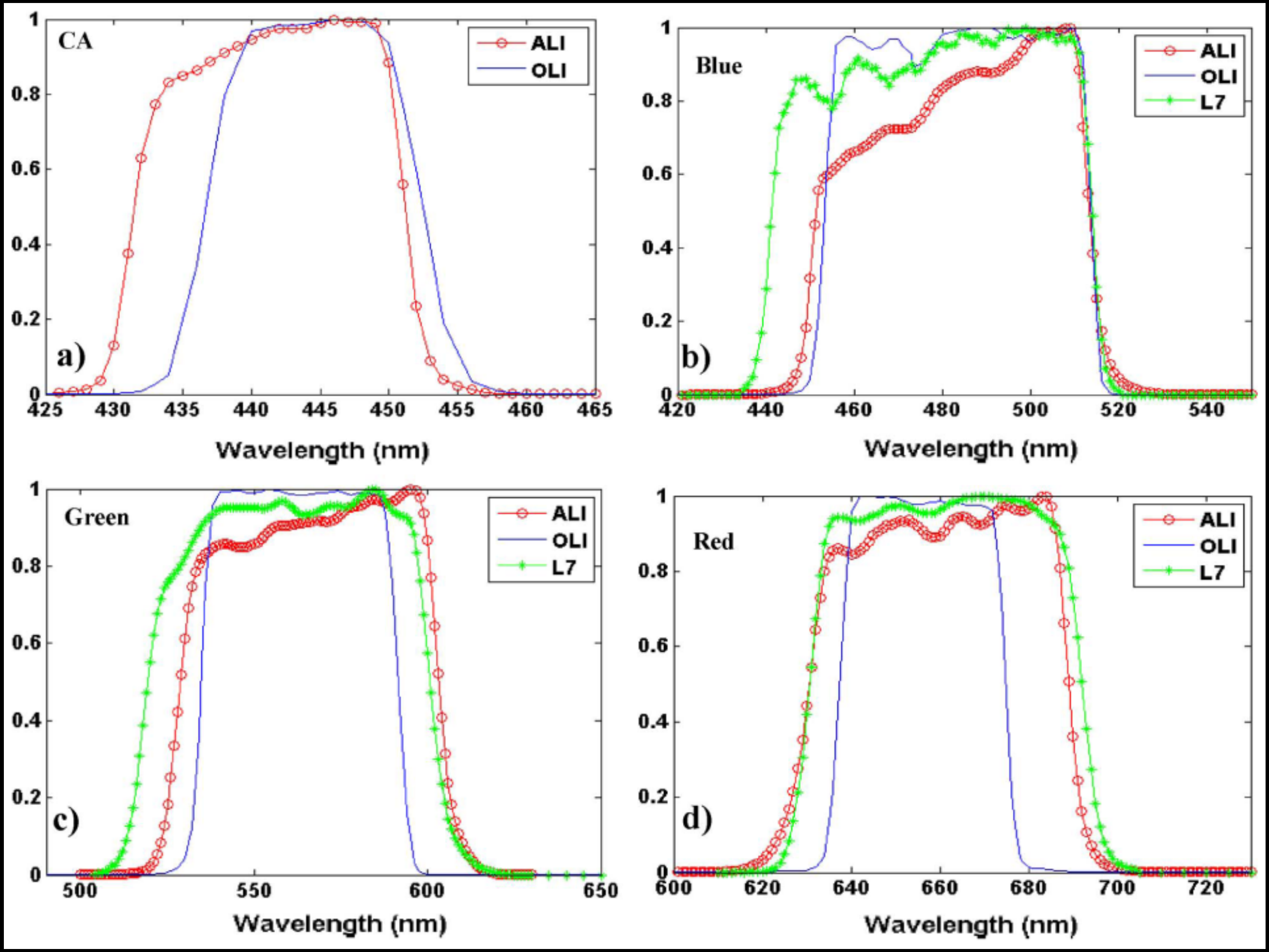

The band-specific, normalized BSR (a)–(d) associated with ETM , OLI, and ALI shown for different parts of the spectrum. Note that ETM does not have the new CA band designed for OLI.

Pahlevan, et al. JSTARS 2013

The spectral scene-derived SNRs shown for different instruments. The ALI sensor has the highest SNR whereas the ETM -derived SNR is the lowest.

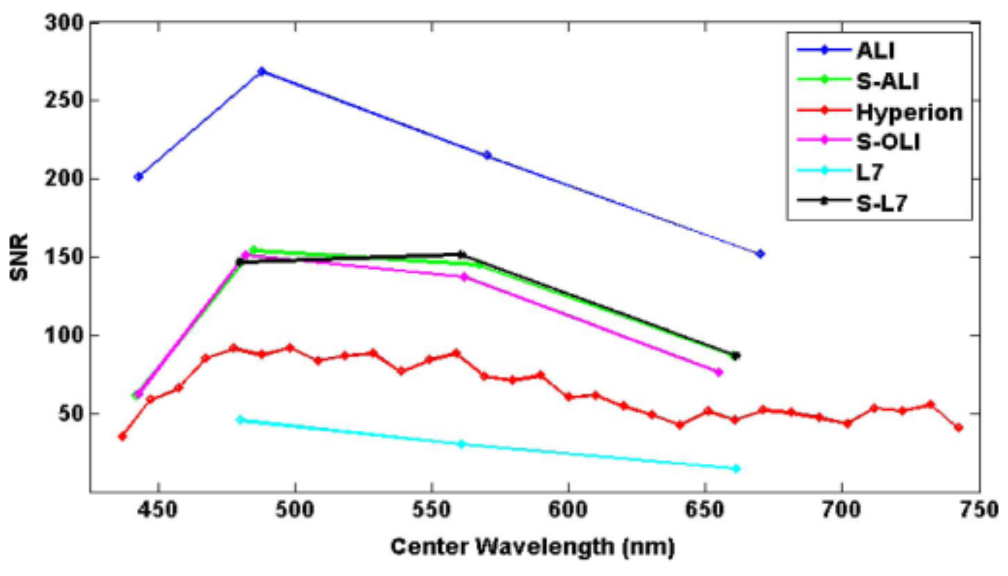

The Hyperion-derived TOA curve shown with that obtained from the MODTRAN simulations.

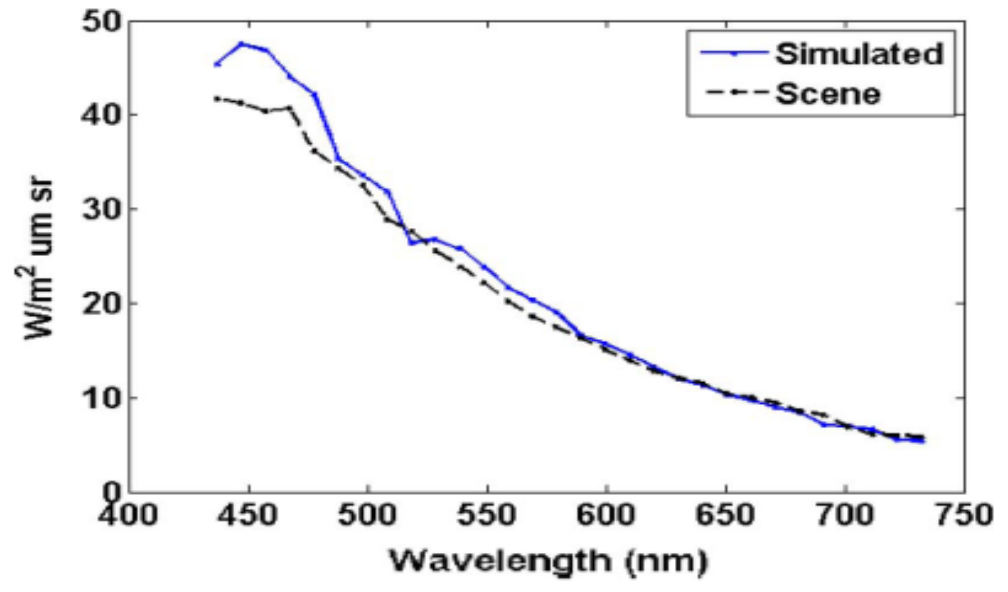

Pahlevan, et al. JSTARS 2013

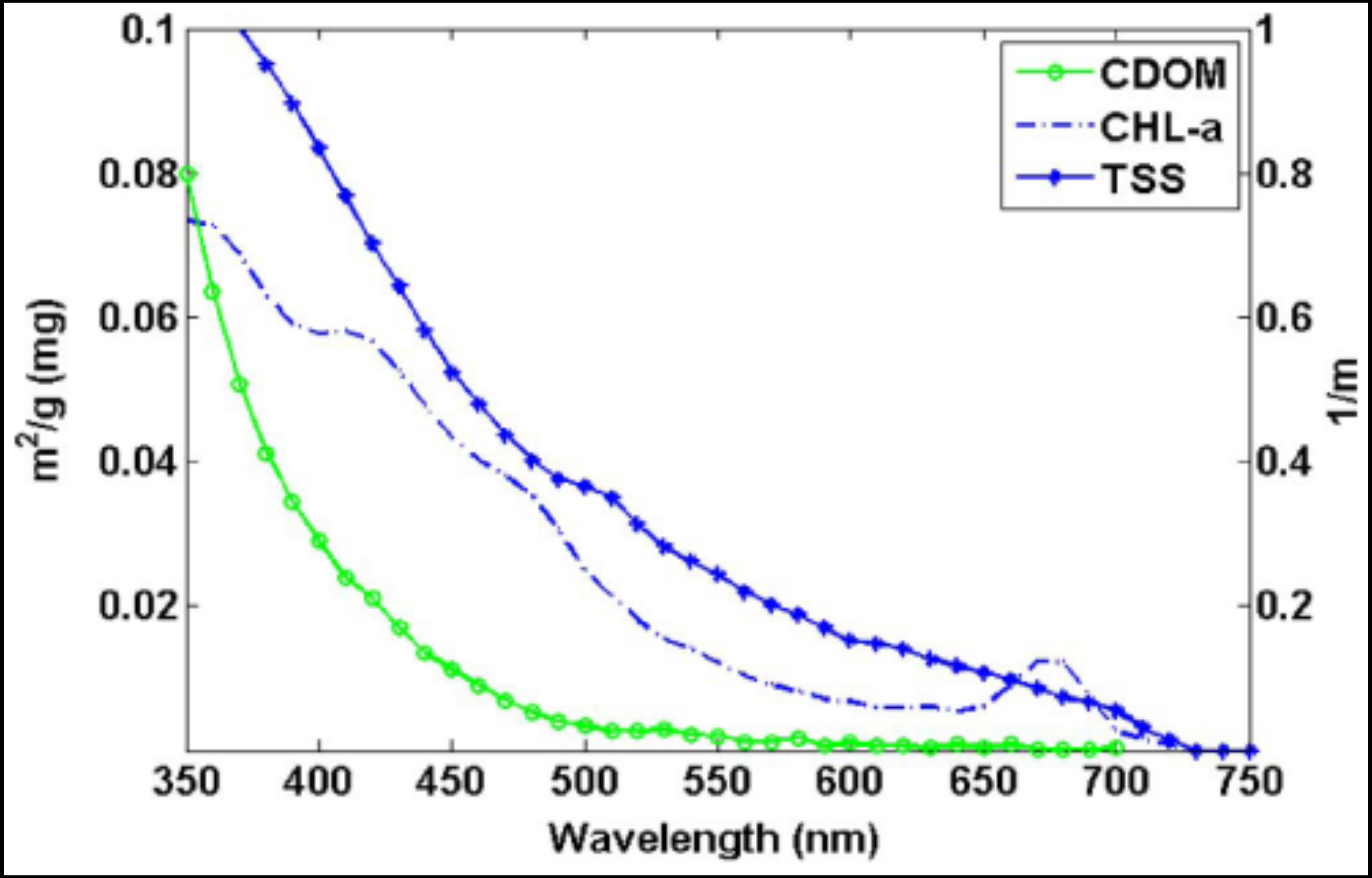

The average absorption of CDOM shown with the specific absorption of CHL and TSS. The large magnitudes below 443 nm found in the CHL absorption spectrum are due to the presence of moderate concentration of dissolved organic matter.

Pahlevan, et al. JSTARS 2013

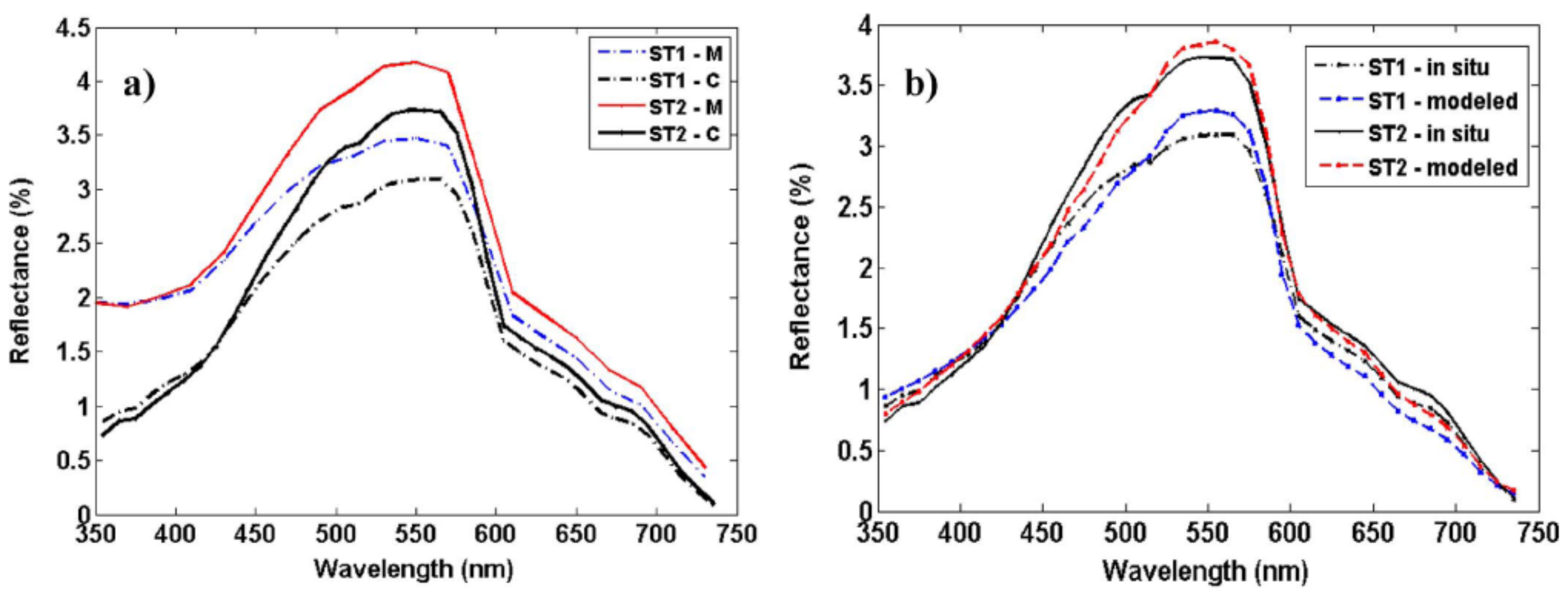

The in situ measured reflectance spectra corrected for sky glint (a). The optical closure shown for the corrected measured spectra versus the best-modeled spectra (b). The matched spectra shown in (b) have resulted from 82% and 75% of the spectra published in [1] and [2], respectively.

[1] R. P. Bukata, et al., Optical Properties and Remote Sensing of Inland and Coastal Waters. New York: CRC Press, 1995.
[2] H. Loisel and A. Morel, "Light scattering and chlorophyll concentration in case 1 waters: Areexamination," Limnol. Oceanogr. ,vol.43, pp. 847–858, Jul. 1998.

Pahlevan, et al. JSTARS 2013

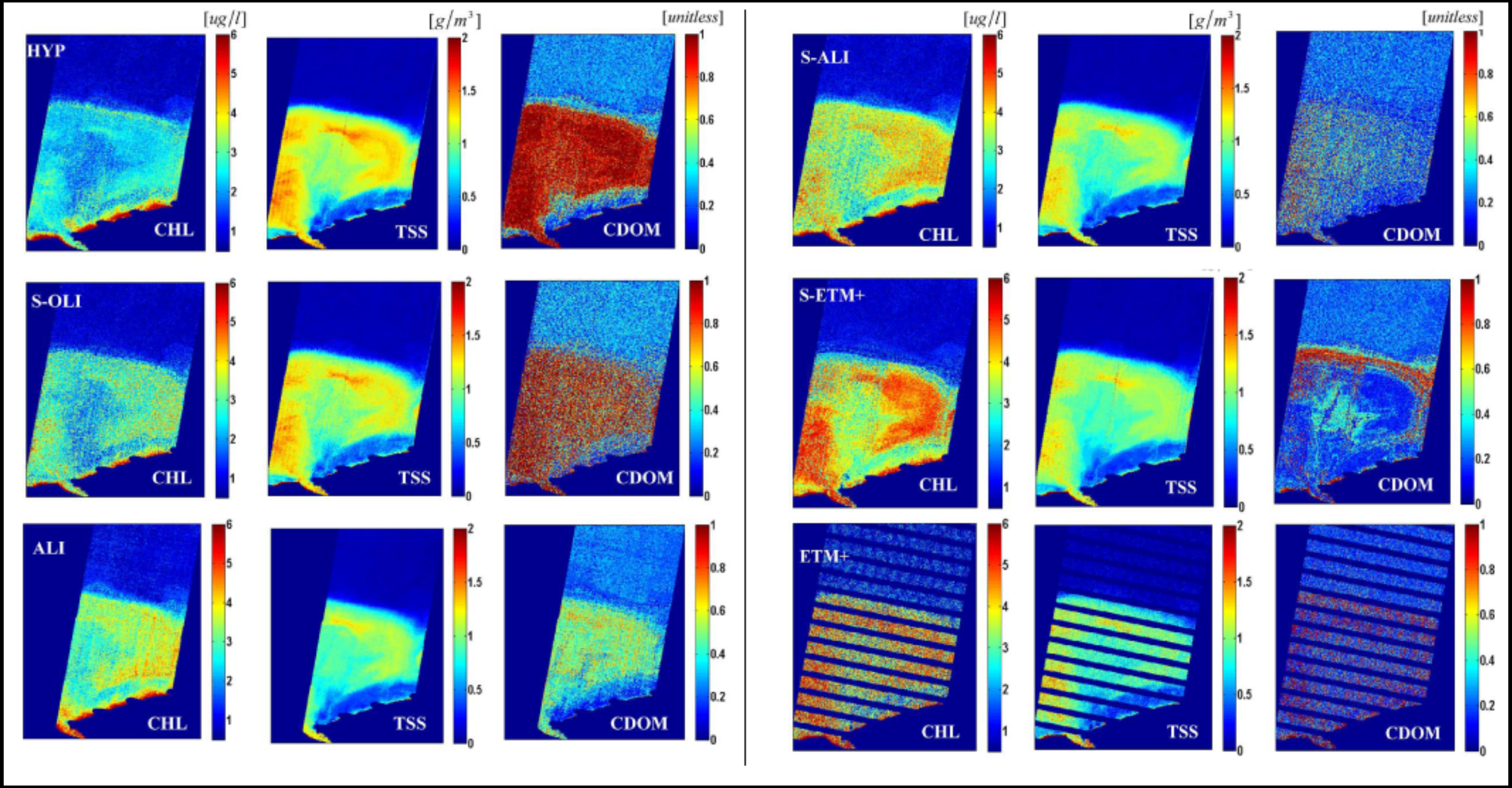

The concentration maps derived from Hyperion (HYP), S-OLI, ALI, S-ALI, S-ETM+, and ETM+. Each group of 3 images corresponds to concentration maps from a dataset. Columns 1 & 4 are the concentrations of CHL (ug/l), columns 2 & 5 are TSS (g/m3), and columns 3 & 6 are CDOM indices [unitless].

Pahlevan, et al. JSTARS 2013

This table includes the basic statistics, including the mean and the CV (the standard deviation over the mean) expressed in [%]. The CV gives an indication of the spatial variability, which is mainly driven by a dataset's SNR and its radiometric resolution. Note that the statistics were derived from 27,000 pixels over the plume and 20,000 pixels in the offshore areas covered by all of the datasets.

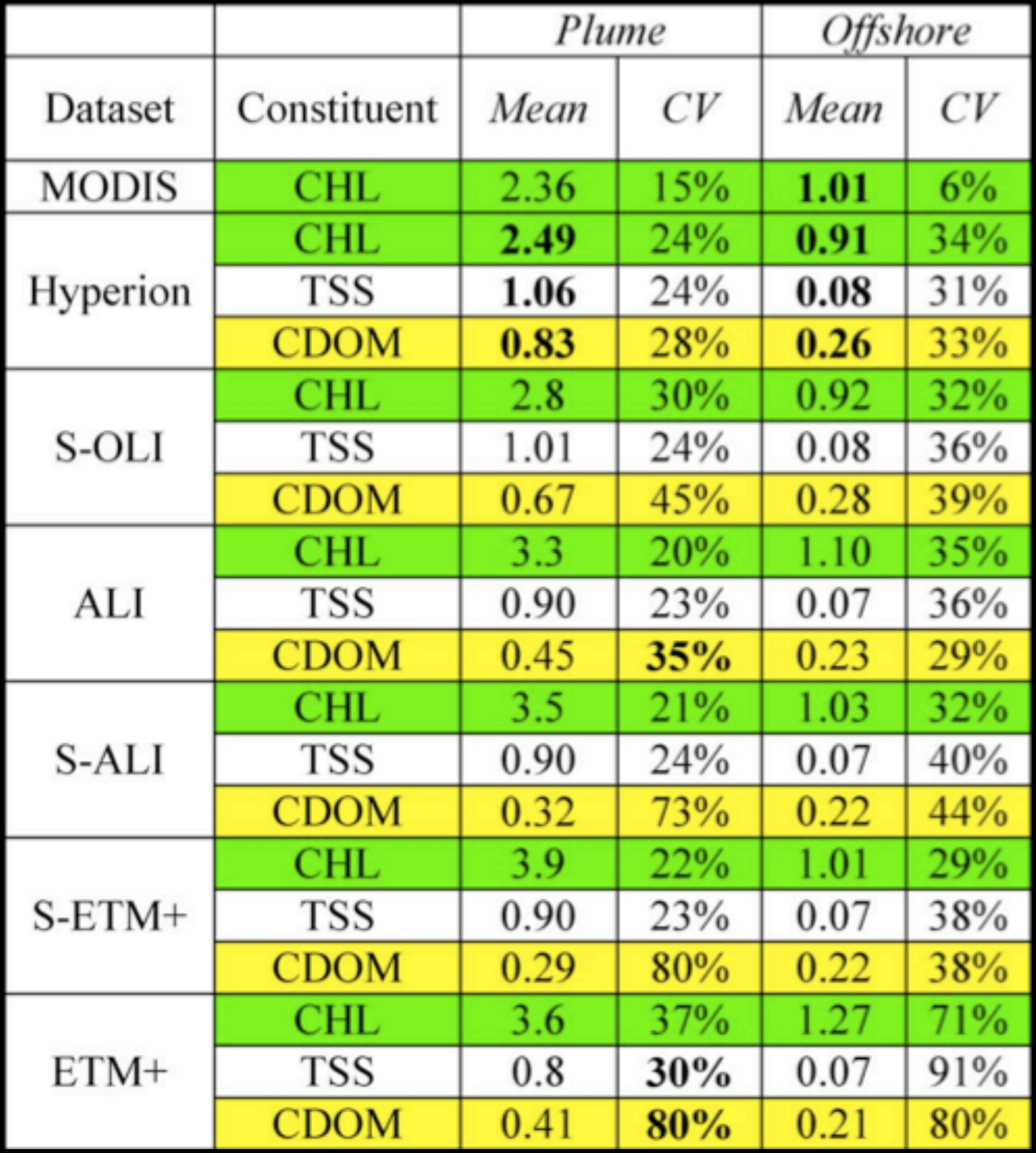

		Plume		*Offshore*	
Dataset	Constituent	*Mean*	*CV*	*Mean*	*CV*
MODIS	CHL	2.36	15%	**1.01**	6%
Hyperion	CHL	**2.49**	24%	**0.91**	34%
	TSS	**1.06**	24%	**0.08**	31%
	CDOM	**0.83**	28%	**0.26**	33%
S-OLI	CHL	2.8	30%	0.92	32%
	TSS	1.01	24%	0.08	36%
	CDOM	0.67	45%	0.28	39%
ALI	CHL	3.3	20%	1.10	35%
	TSS	0.90	23%	0.07	36%
	CDOM	0.45	**35%**	0.23	29%
S-ALI	CHL	3.5	21%	1.03	32%
	TSS	0.90	24%	0.07	40%
	CDOM	0.32	73%	0.22	44%
S-ETM+	CHL	3.9	22%	1.01	29%
	TSS	0.90	23%	0.07	38%
	CDOM	0.29	80%	0.22	38%
ETM+	CHL	3.6	37%	1.27	71%
	TSS	0.8	**30%**	0.07	91%
	CDOM	0.41	**80%**	0.21	80%

JSTARS EO-1 Special Issue

Using EO-1 Hyperion Data as HyspIRI Preparatory Data Sets for Volcanology Applied to Mt Etna, Italy

Michael Abrams, Dave Pieri, Vince Realmuto, and Robert Wright

Abstract — One of the main goals of the Hyperspectral and Infrared Imager (HyspIRI) mission is to provide global observations of surface attributes at local and landscape spatial scales (tens of meters to hundreds of kilometers) to map volcanic gases and surface temperatures, which are identified as indicators of impending volcanic hazards, as well as plume ejecta which pose risks to aircraft and people and property downwind. Our project has created precursor HyspIRI data sets for volcanological analyses, using existing data over Mt. Etna, Italy. We have identified 28 EO-1 Hyperion data acquisitions, and 12 near-coincident ASTER data acquisitions, covering six eruptive periods between 2001 and 2010. These data sets provide us with 30 m hyperspectral VSWIR data and 90 m multispectral TIR data (satellite). They allowed us to examine temporal sequences of several Etnaean eruptions. We addressed the following critical questions, directly related to understanding eruption hazards: 1) What do changes in SO emissions tell us about a volcano's activity? How well do these measurements compare with ground-based COSPEC measurements? 2) How do we use measurements of lava flow temperature and volume to predict advances of the flow front? 3) What do changes in lava lake temperatures and energy emissions tell us about possible eruptive behavior?

Abrams, et al. JSTARS 2013

Location map of Mt. Etna volcano in Sicily, Italy, and an aerial view of Mt. Etna during simultaneous summit and flank eruptions (plume on right). Image taken from the International Space Station on October 30, 2002.

Abrams, et al. JSTARS 2013

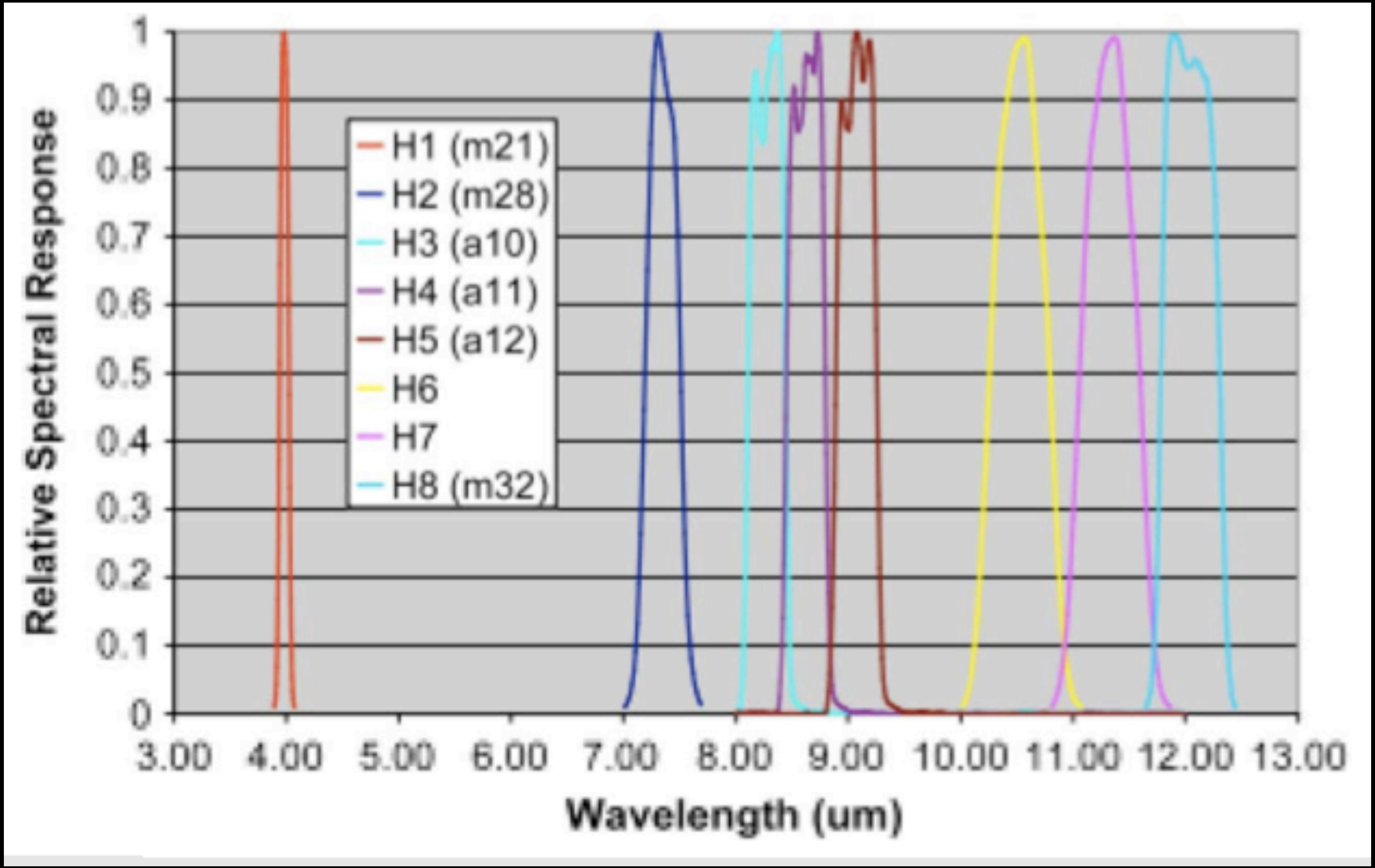

Proposed HyspIRI TIR bandpass placements for eight channels.

Abrams, et al. JSTARS 2013

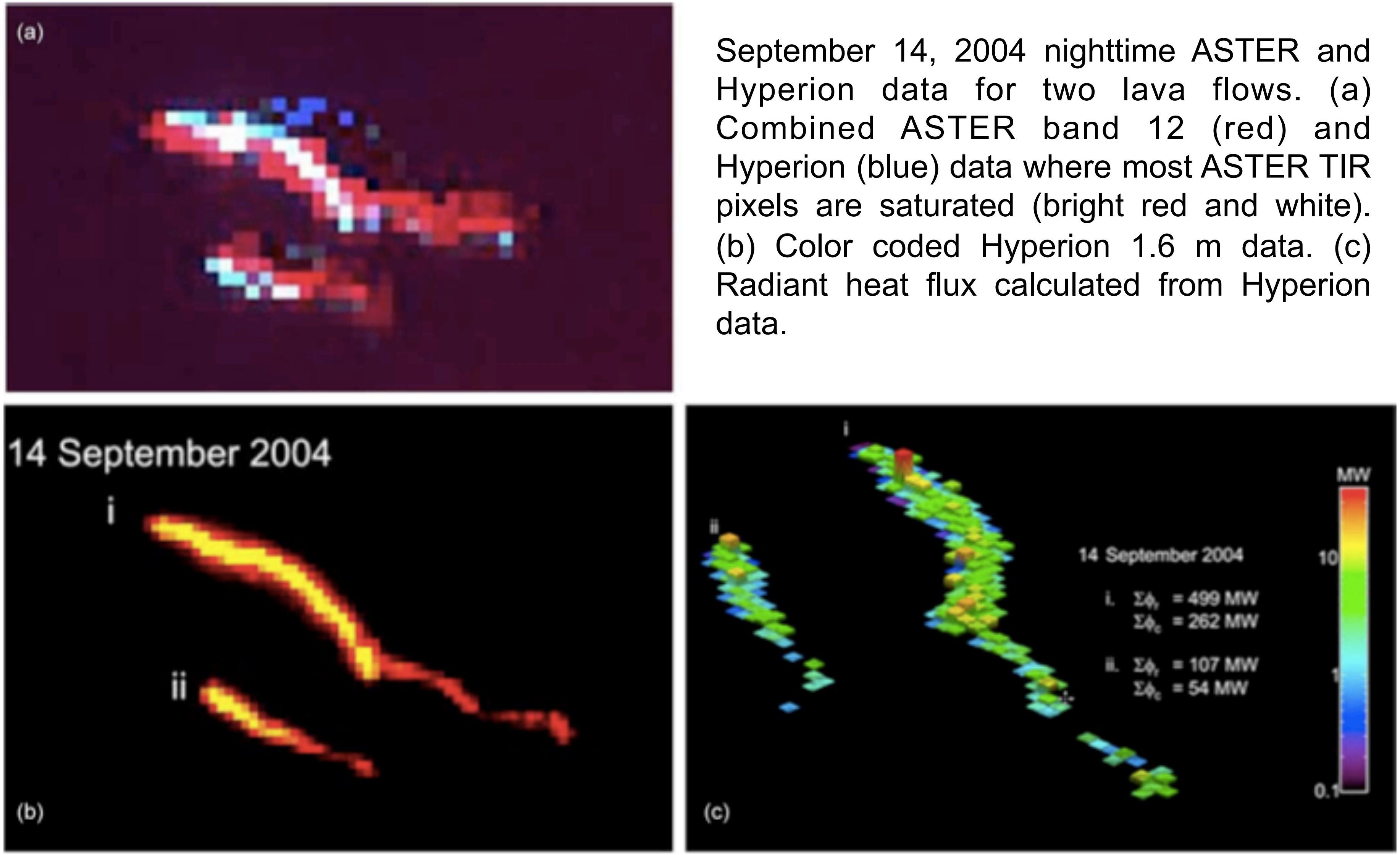

September 14, 2004 nighttime ASTER and Hyperion data for two lava flows. (a) Combined ASTER band 12 (red) and Hyperion (blue) data where most ASTER TIR pixels are saturated (bright red and white). (b) Color coded Hyperion 1.6 m data. (c) Radiant heat flux calculated from Hyperion data.

Abrams, et al. JSTARS 2013

January 15, 2003 Hyperion daytime data. Bands 27 (0.620 m), 57 (0.925 m), and 84 (1.194 m) are in RGB. The plots show radiance at the sensor as a function of wavelength for lava pixels at three different temperatures.

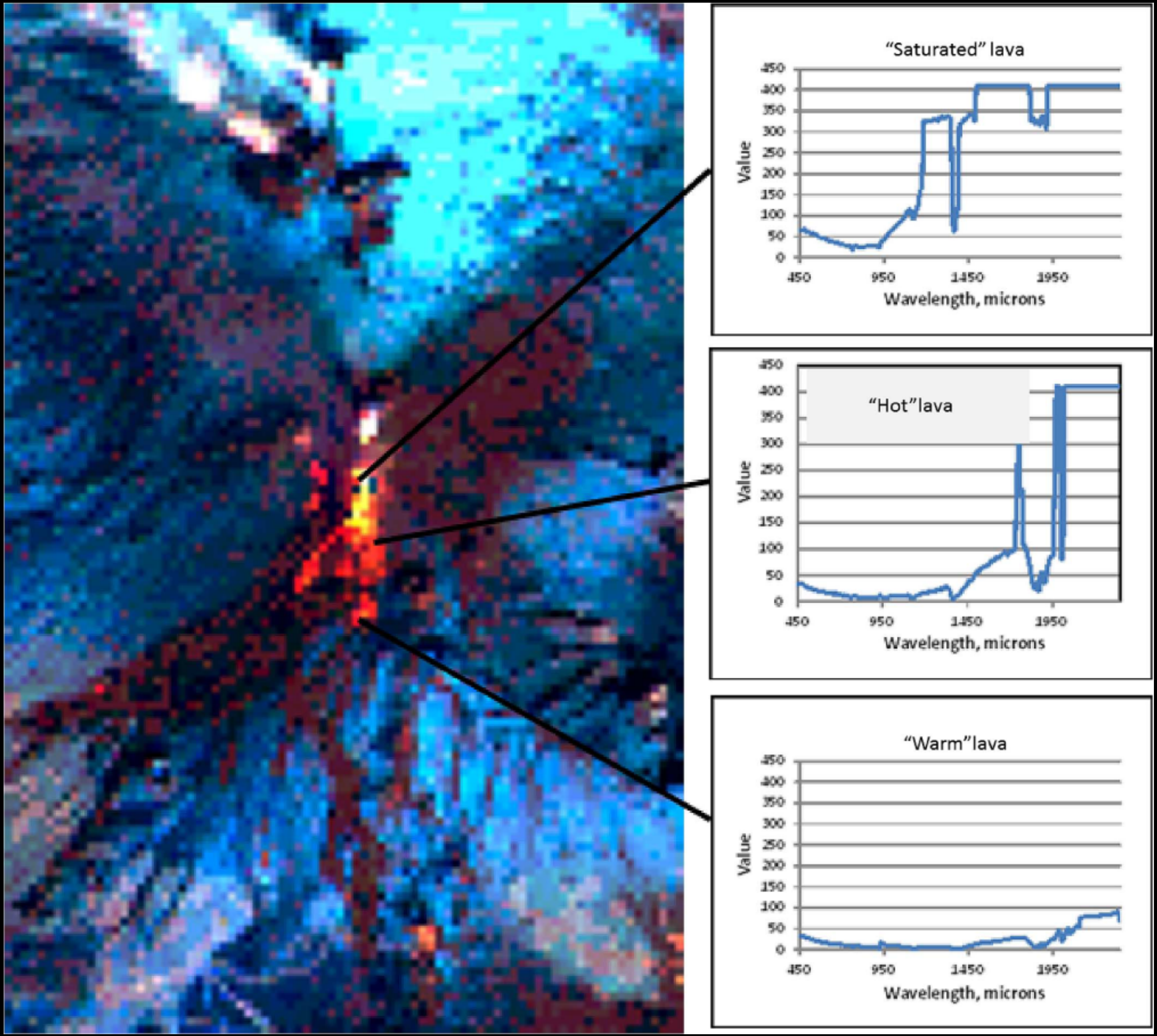

Abrams, et al. JSTARS 2013

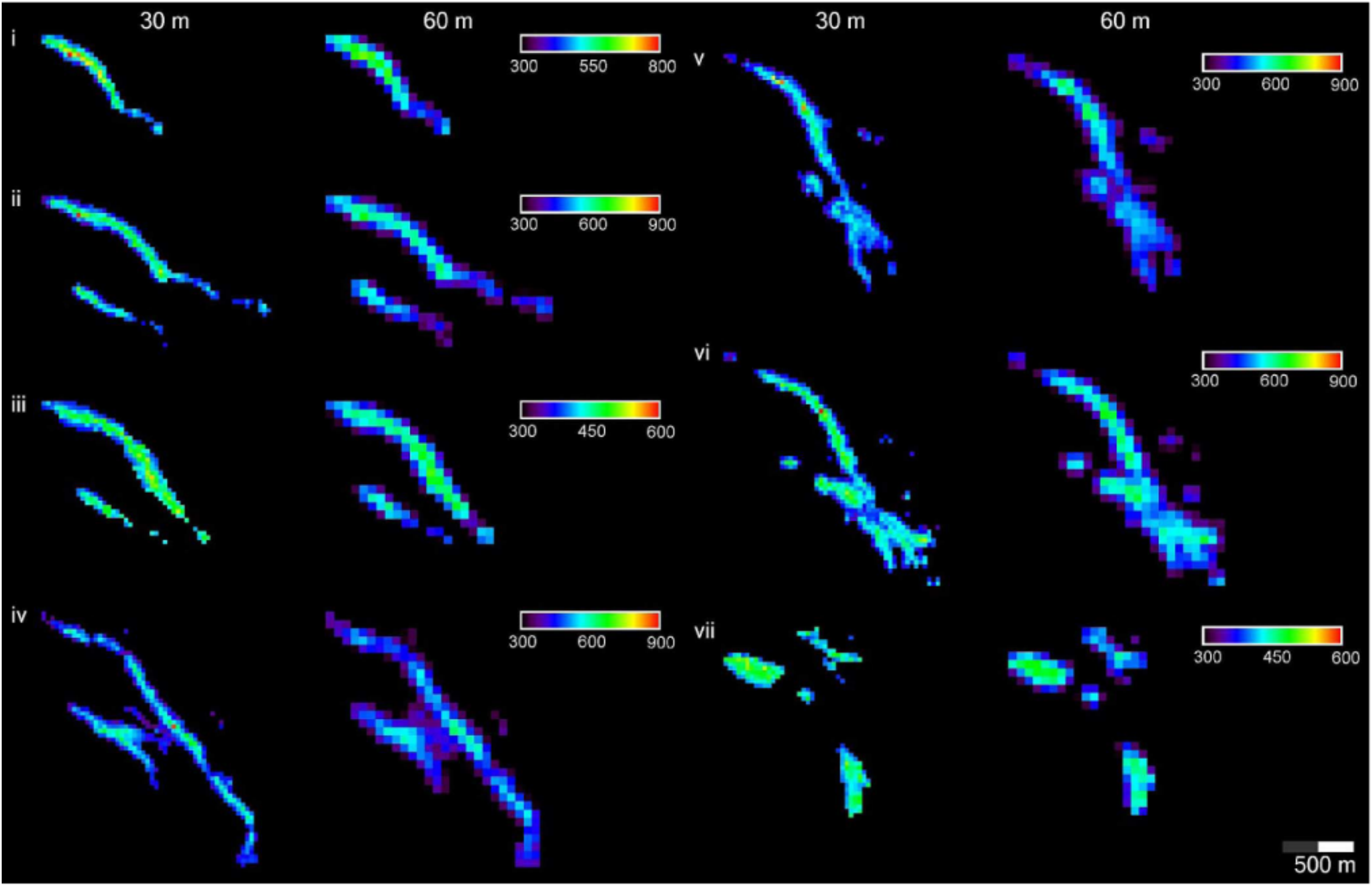

The development of a lava flow at Mt. Etna, Sicily is shown in a time sequence of seven Hyperion images (i)–(vii) using the 4-μm band. These are shown on the left for native 30-m Hyperion resolution, paired (on the right) with simulated HyspIRI TIR 4-μm images, both spatially (60 m) and spectrally. Hyperion images used to generate these results were acquired on (i) Sept 12, 2004, (ii) Sept 14, 2004, (iii) Sept 16, 2004, (iv) Sept 23, 2004, (v) Oct 7, 2004, (vi) Oct 9, 2004, and (vii) Dec 3, 2004.

Abrams, et al. JSTARS 2013

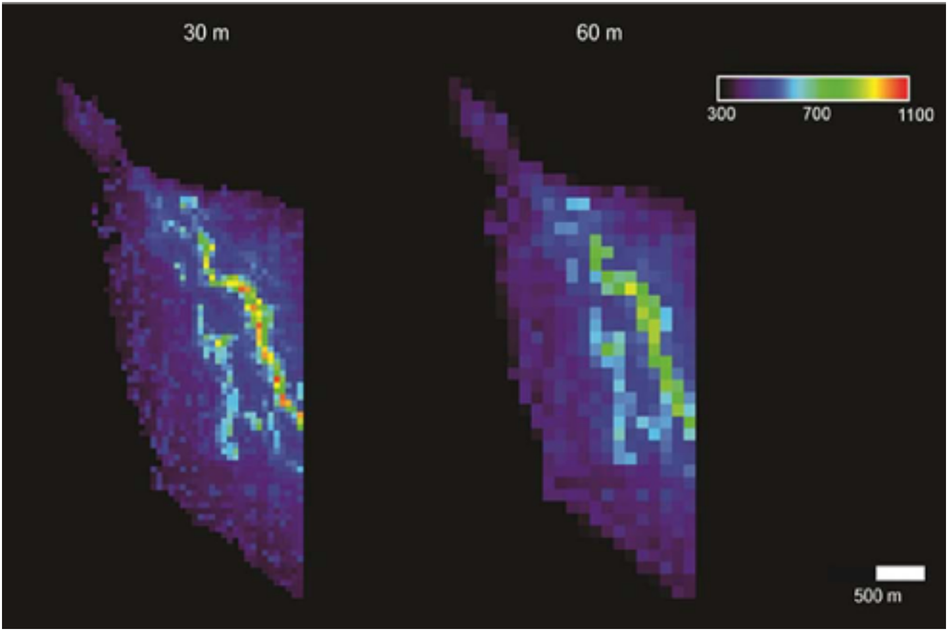

Simulated HyspIRI 4-m image of a lava flow at Nyamuragira volcano, Democratic Republic of Congo. Color bar gives the 4-µm brightness temperature for each pixel (in Kelvin). On the left is the 4-µm brightness temperature estimated from Hyperion data. On the right, the same data resampled spatially and spectrally to match the proposed specifications of HyspIRI. The Hyperion image used to generate this result was acquired on May 20, 2004.

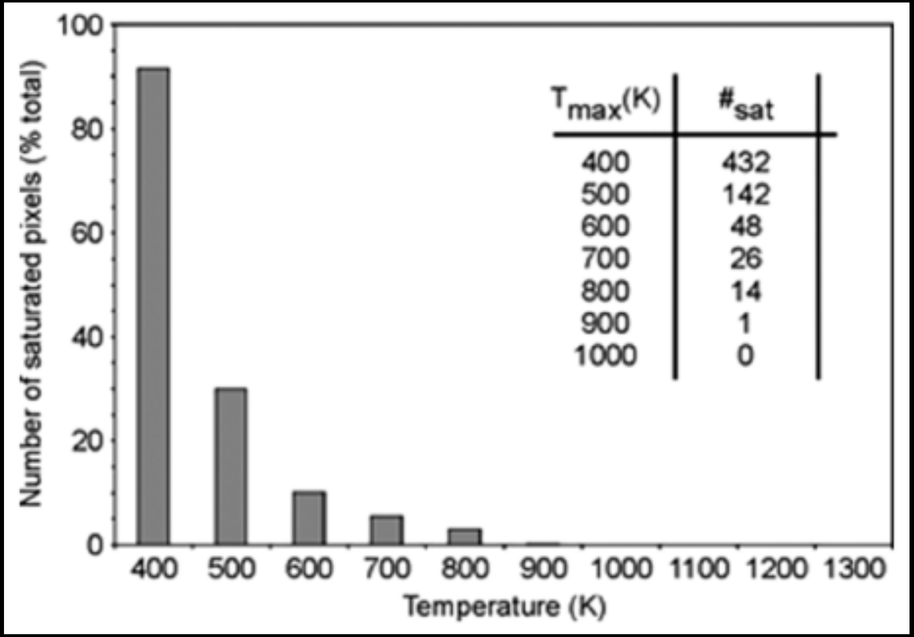

T_{max}(K)	$\#_{sat}$
400	432
500	142
600	48
700	26
800	14
900	1
1000	0

Histogram showing the number of lava flow pixels predicted to saturate HyspIRI's 4-µm band as a function of Tmax, for the Nyamuragira example depicted in the previous slide.

Abrams, et al. JSTARS 2013

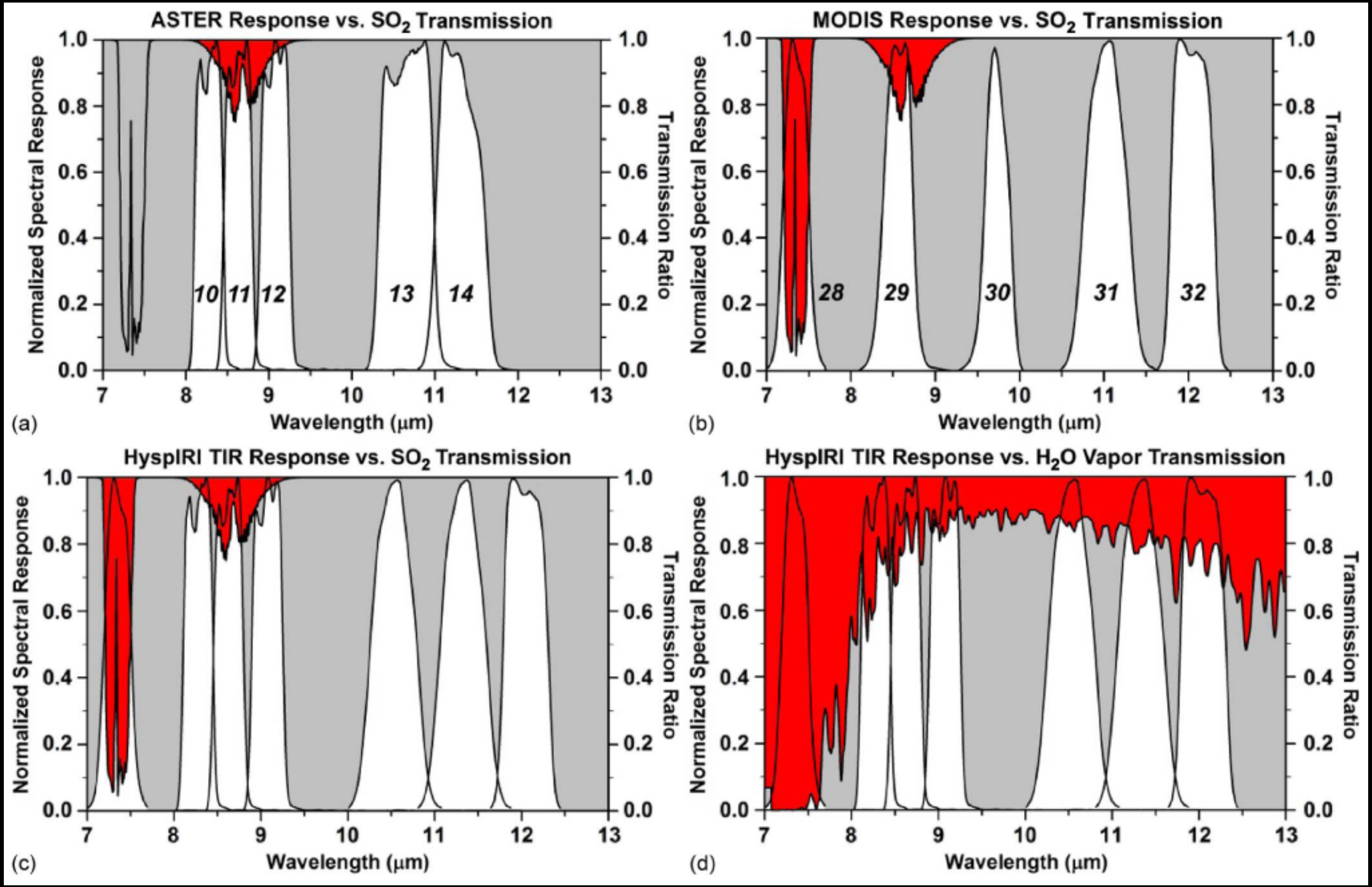

Comparison of the TIR spectral response of ASTER, MODIS, and the HyspIRI TIR to the transmission spectra of SO_2 and water vapor H_2O. (a) ASTER vs. SO_2, (b) MODIS vs. SO_2, (c) Notional HyspIRI vs. SO_2, and (d) Notional HyspIRI vs. H_2O.

JSTARS EO-1 Special Issue

Vicarious Calibration of EO-1 Hyperion

Joel McCorkel, Kurtis Thome, and Lawrence Ong

Abstract — The Hyperion imaging spectrometer on the Earth Observing-1 satellite is the first high-spatial resolution imaging spectrometer to routinely acquire science-grade data from orbit. Data gathered with this instrument needs to be quantitative and accurate in order to derive meaningful information about ecosystem properties and processes. Also, comprehensive and long-term ecological studies require these data to be comparable over time, between coexisting sensors and between generations of follow-on sensors. One method to assess the radiometric calibration is the reflectance-based approach, a common technique used for several other earth science sensors covering similar spectral regions. This work presents results of radiometric calibration of Hyperion based on the reflectance-based approach of vicarious calibration implemented by University of Arizona during 2001–2005. These results show repeatability to the 2% level and accuracy on the 3–5% level for spectral regions not affected by strong atmospheric absorption. Knowledge of the stability of the Hyperion calibration from moon observations allows for an average absolute calibration based on the reflectance-based results to be determined and applicable for the lifetime of Hyperion.

McCorkel, et al. JSTARS 2013

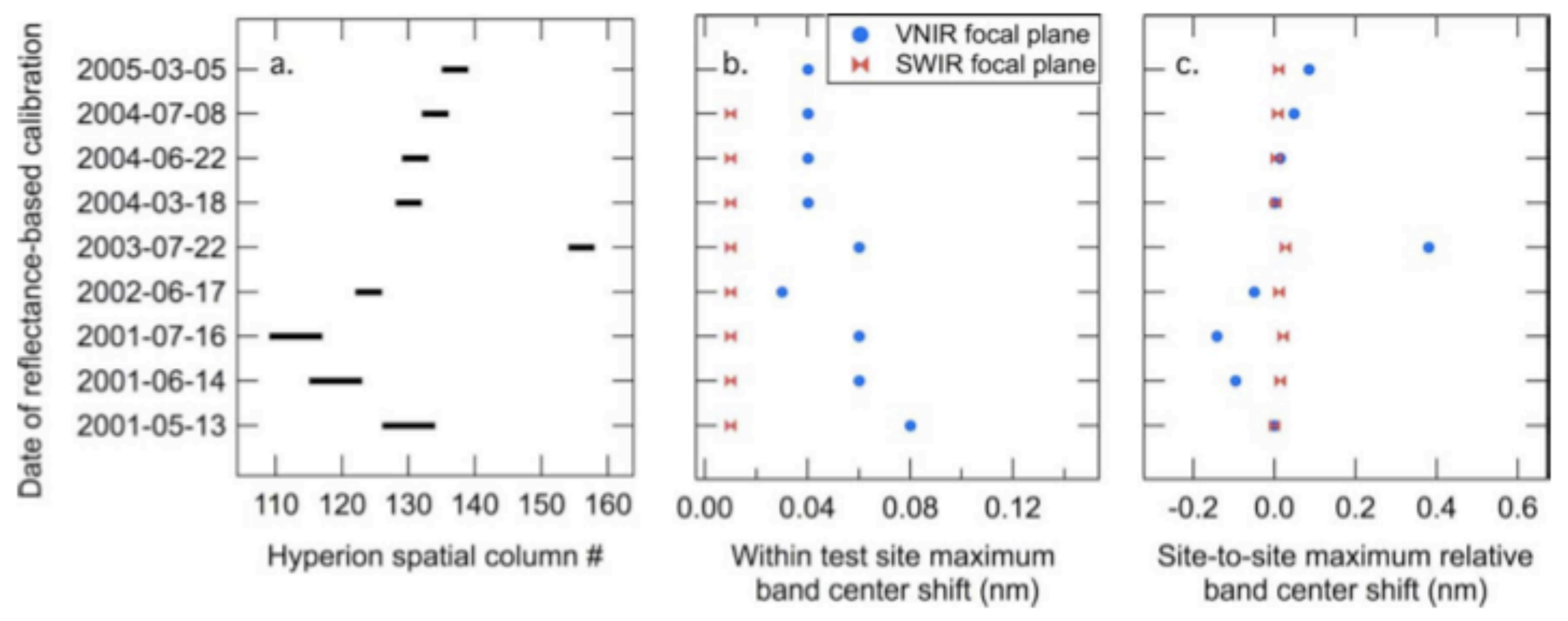

Spatial and spectral attributes for each calibration data point including (a) Hyperion spatial columns covered by RVPN test site for each data set, (b) maximum spectral offset of band center values within data sets, and (c) maximum spectral offset of band center values amongst data sets relative to the first.

McCorkel, et al. JSTARS 2013

Mean of nine data sets in the form of percent disagreement between at-sensor radiance prediction and Hyperion-measured radiance.

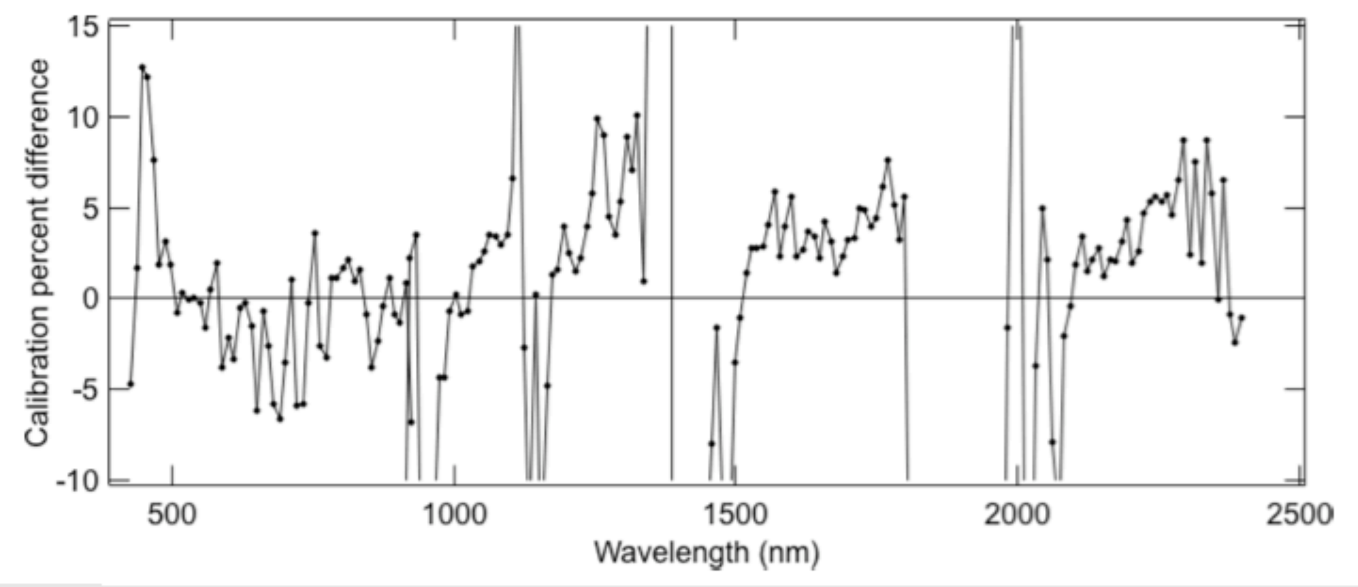

Percent standard deviation of the mean disagreement between at-sensor radiance prediction and Hyperion-measured radiance.

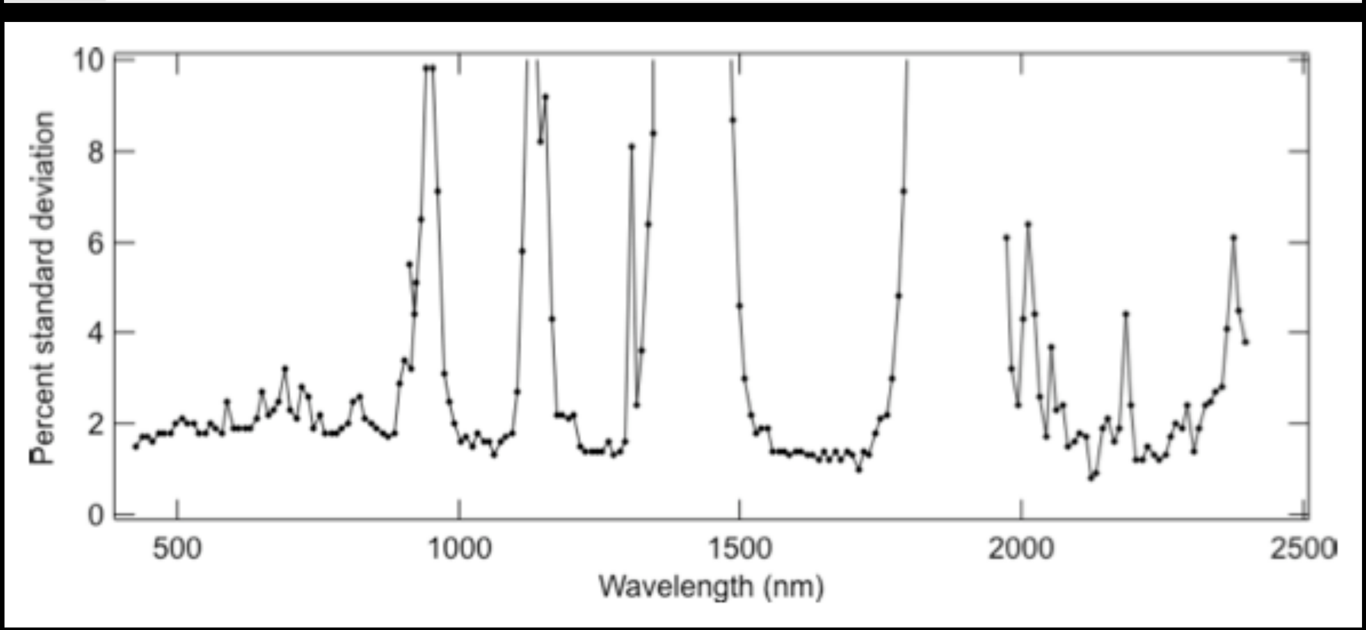

McCorkel, et al. JSTARS 2013

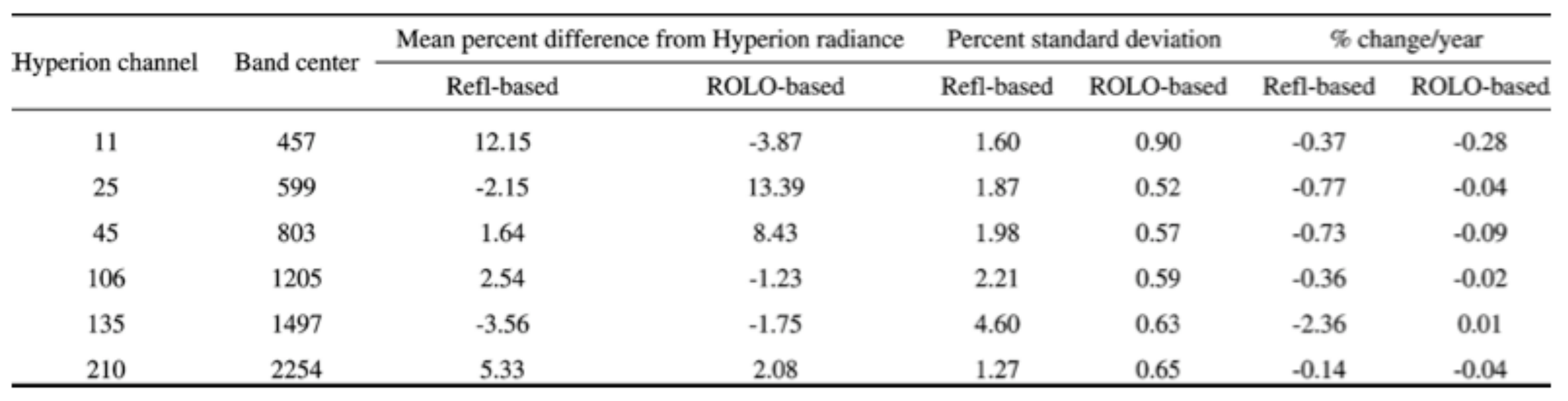

Hyperion channel	Band center	Mean percent difference from Hyperion radiance		Percent standard deviation		% change/year	
		Refl-based	ROLO-based	Refl-based	ROLO-based	Refl-based	ROLO-based
11	457	12.15	-3.87	1.60	0.90	-0.37	-0.28
25	599	-2.15	13.39	1.87	0.52	-0.77	-0.04
45	803	1.64	8.43	1.98	0.57	-0.73	-0.09
106	1205	2.54	-1.23	2.21	0.59	-0.36	-0.02
135	1497	-3.56	-1.75	4.60	0.63	-2.36	0.01
210	2254	5.33	2.08	1.27	0.65	-0.14	-0.04

Summary of ROLO model-based comparison to Hyperion with associated reflectance-based results

McCorkel, et al. JSTARS 2013

Hyperion percent difference from the ROLO model (small filled circles) and reflectance-based results (large open circles) for three spectral channels each of Hyperion's focal planes. The 60 lunar-based data points have less than 1% variability and show that Hyperion is stable over its lifetime, although impaired by 5–10% absolute uncertainty explaining the large discrepancy between the data sets. The reflectance-based results provide less than 3% absolute uncertainty, but only exist for the first four years of operation. Thus, the combination of the reflectance-based approach results lunar-based data set provides an accurate absolute radiometric scale for the lifetime of the Hyperion.

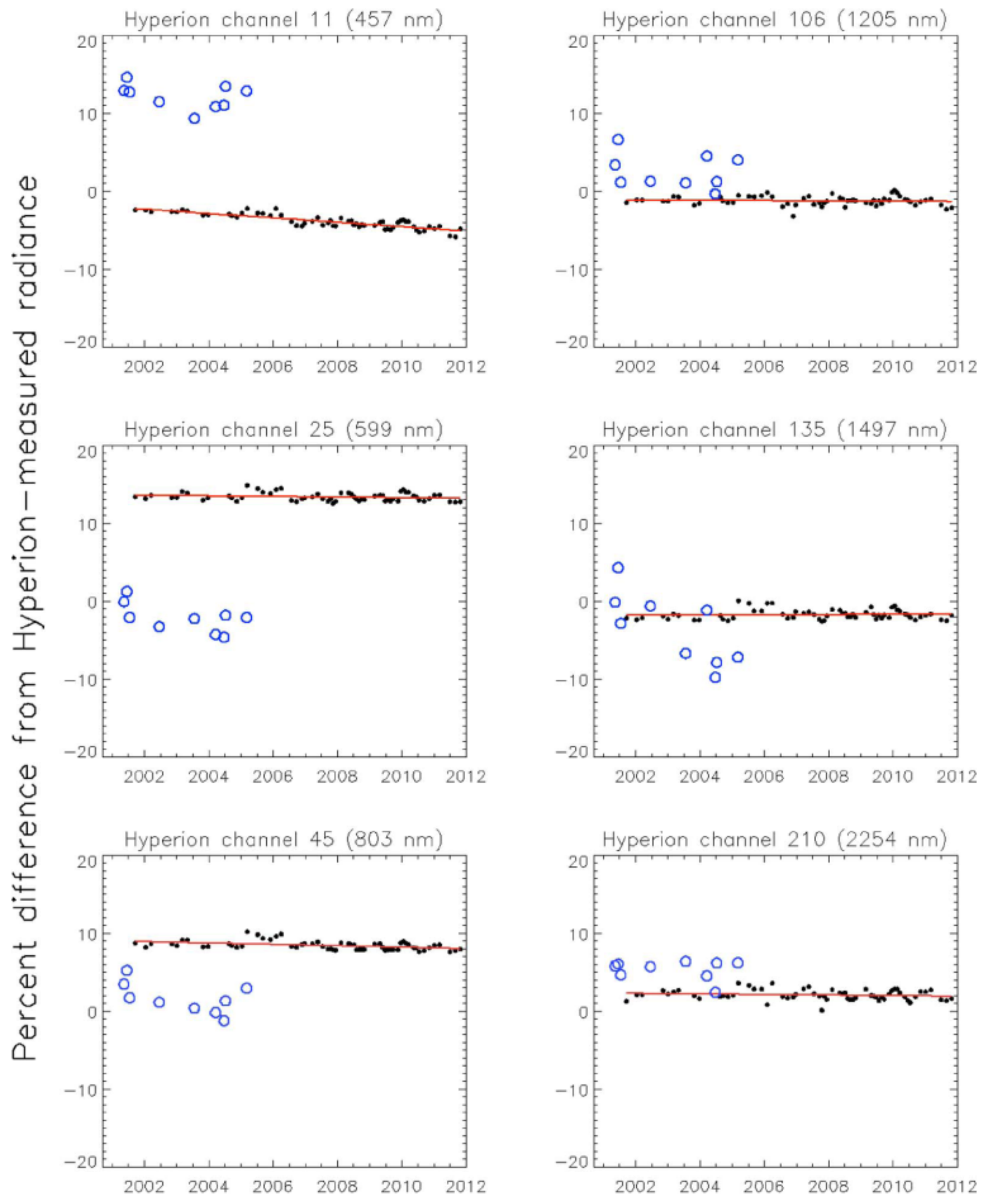

JSTARS EO-1 Special Issue

Cloud Implementation of a Full Hyperspectral Unmixing Chain Within the NASA Web Coverage Processing Service for EO-1

Pat Cappelaere, Sergio Sánchez, Sergio Bernabé, Antonio Scuri, Daniel Mandl, and Antonio Plaza

Abstract — The launch of the NASA Earth Observing 1 (EO-1) platform in November 2000 marked the establishment of spaceborne hyperspectral technology for land imaging. The Hyperion sensor onboard EO-1 operates in the 0.4–2.5 micrometer spectral range, with 10 nanometer spectral resolution and 30-meter spatial resolution. Spectral unmixing has been one of the most successful approaches to analyze Hyperion data since its launch. It estimates the abundance of spectrally pure constituents (end- members) in each observation collected by the sensor. Due to the high spectral dimensionality of Hyperion data, unmixing is a very time-consuming operation. In this paper, we develop a cloud implementation of a full hyperspectral unmixing chain made up of the following steps: 1) dimensionality reduction; 2) automatic endmember identification; and 3) fully constrained abundance estimation. The unmixing chain will be available online within the Web Coverage Processing Service (WCPS), an image processing framework that can run on the cloud, as part of the NASA SensorWeb suite of web services. The proposed implementation has been demonstrated using the EO-1 Hyperion imagery. Our experimental results with a hyperspectral scene collected over the Okavango Basin in Botswana suggest the (present and future) potential of spectral unmixing for improved exploitation of spaceborne hyperspectral data. The integration of the unmixing chain in the WCPS framework as part of the NASA SensorWeb suite of web services is just the start of an international collaboration in which many more processing algorithms will be made available to the community through this service. This paper is not so much focused on the theory and results of unmixing (widely demonstrated in other contributions) but about the process and added value of the proposed contribution for ground processing on the cloud and onboard migration of those algorithms to support the generation of low-latency products for new airborne/spaceborne missions.

Cappelaere, et al. JSTARS 2013

Cloud implementation of the Web Coverage Processing System (WPCS). To leverage the availability of virtual machines that can be instantiated on the fly, the WCPS is broken down into workers waiting on a software bus for imaging tasks generated by end-users. The front-end web service is clustered behind a load balancer (called HAProxy) and high performance HTTP Server and reverse proxy (called NGINX).

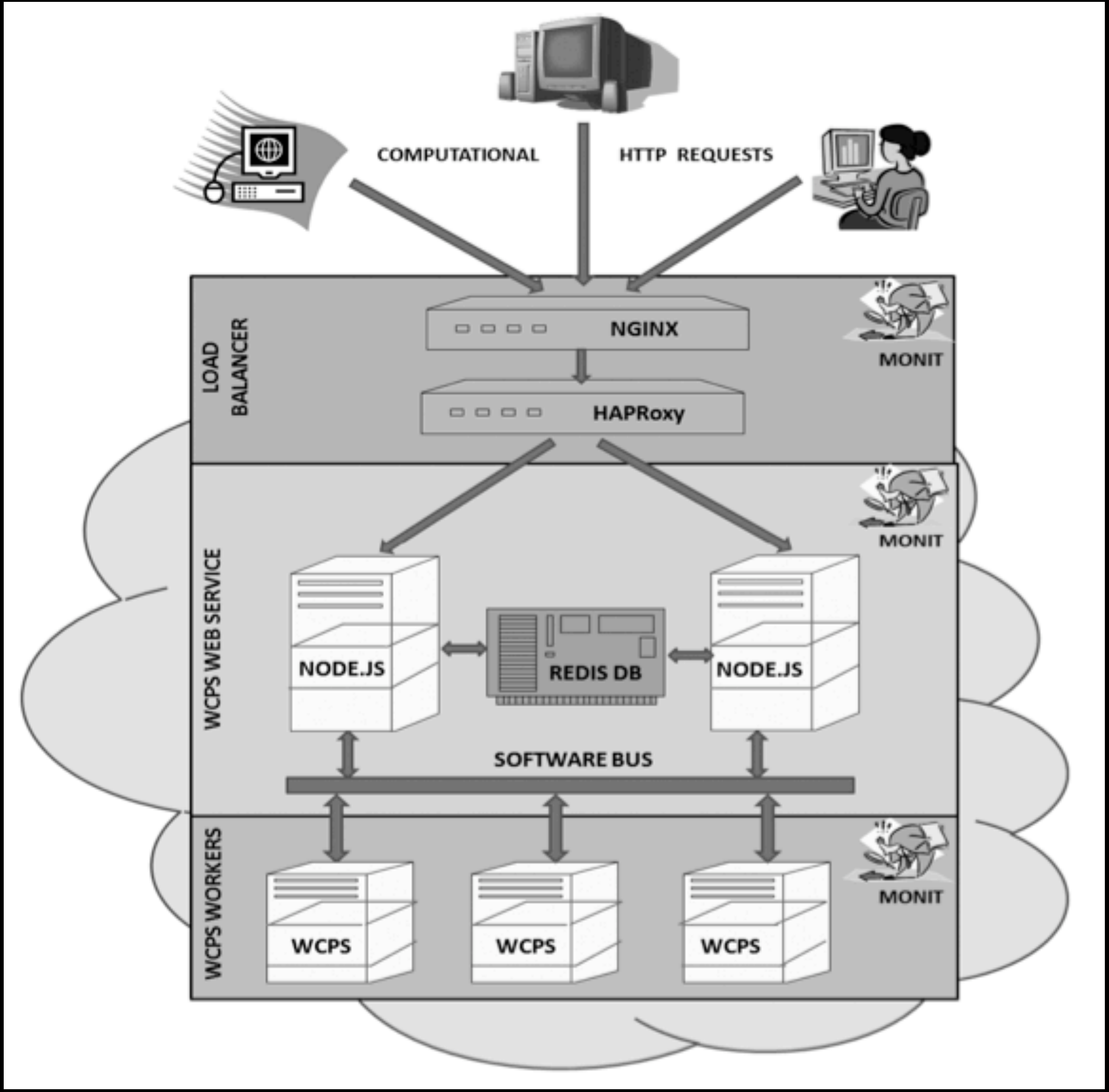

Cappelaere, et al. JSTARS 2013

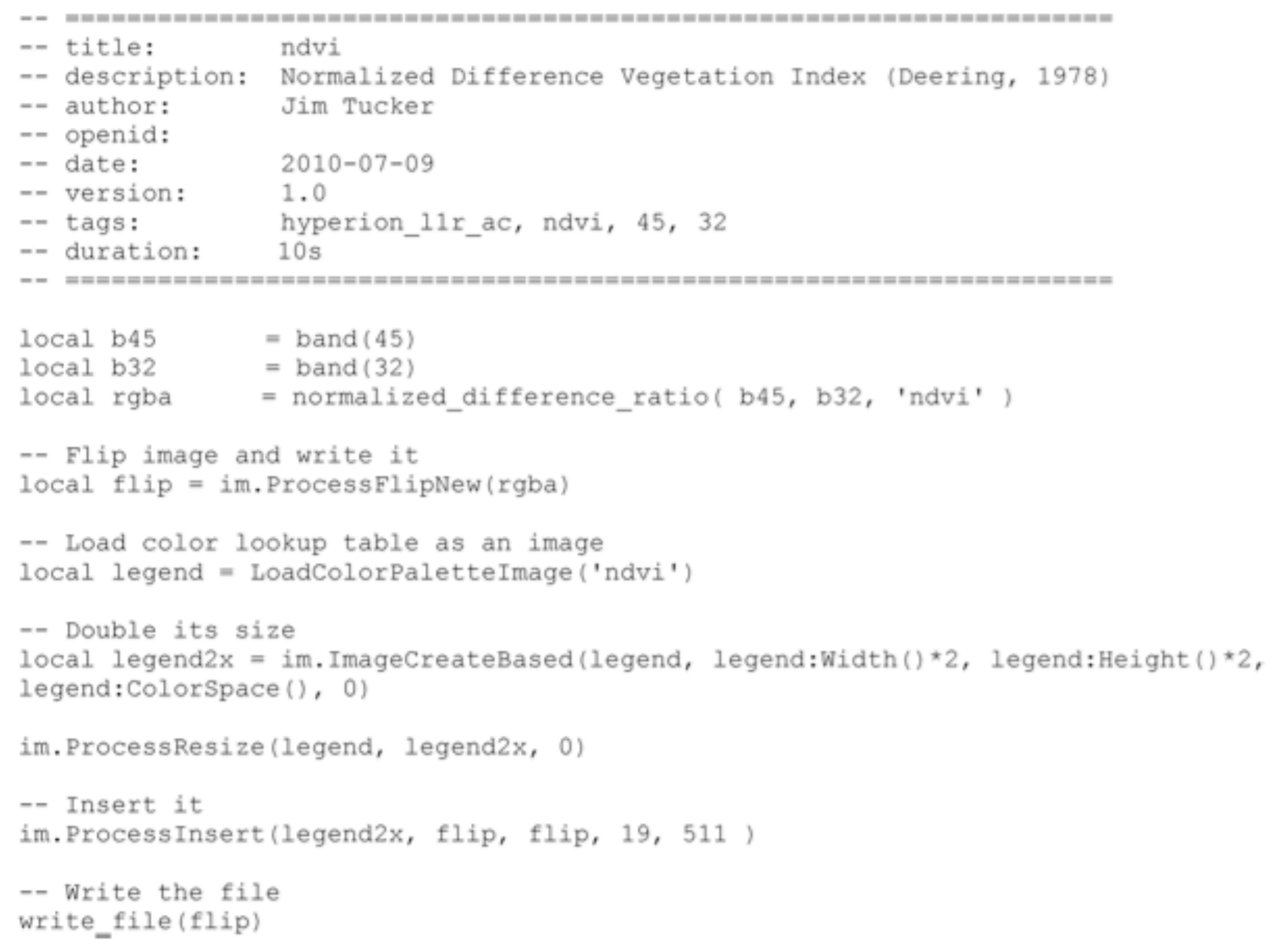

```
-- ======================================================================
-- title:        ndvi
-- description:  Normalized Difference Vegetation Index (Deering, 1978)
-- author:       Jim Tucker
-- openid:
-- date:         2010-07-09
-- version:      1.0
-- tags:         hyperion_l1r_ac, ndvi, 45, 32
-- duration:     10s
-- ======================================================================

local b45       = band(45)
local b32       = band(32)
local rgba      = normalized_difference_ratio( b45, b32, 'ndvi' )

-- Flip image and write it
local flip = im.ProcessFlipNew(rgba)

-- Load color lookup table as an image
local legend = LoadColorPaletteImage('ndvi')

-- Double its size
local legend2x = im.ImageCreateBased(legend, legend:Width()*2, legend:Height()*2,
legend:ColorSpace(), 0)

im.ProcessResize(legend, legend2x, 0)

-- Insert it
im.ProcessInsert(legend2x, flip, flip, 19, 511 )

-- Write the file
write_file(flip)
```

Example of a WCPS script intended to compute the normalized NDVI.

Cappelaere, et al. JSTARS 2013

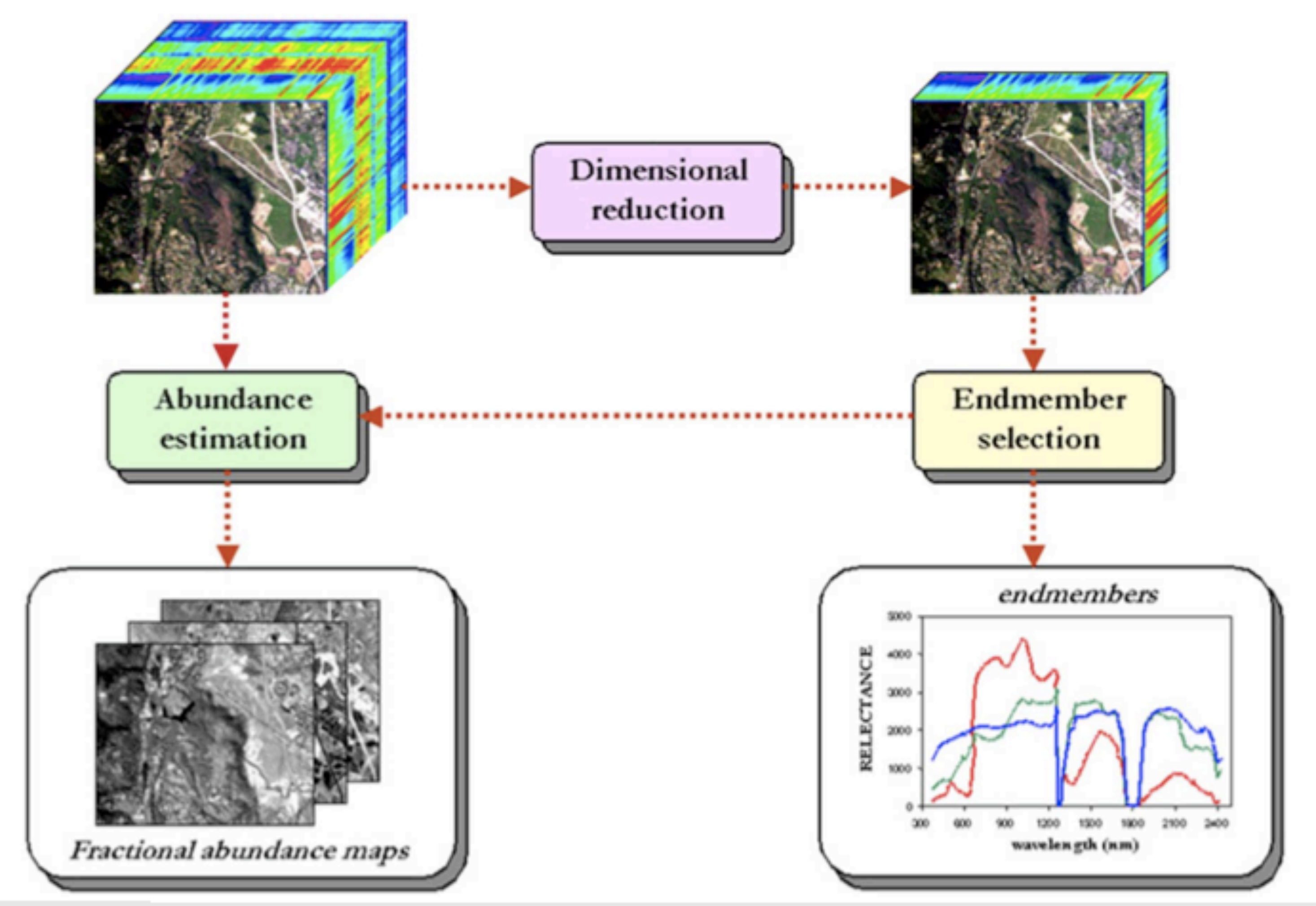

Spectral unmixing chain implemented in this work in WCPS.

Cappelaere, et al. JSTARS 2013

Example of a WCPS script to compute a fully constrained spectral unmixing chain. (a) Pseudo-RGB color image of the Hyperion Botswana scene. (b–f) Some of the abundance maps estimated by the WCPS implementation of the full spectral unmixing chain represented using the color map in (g). (a) RGB; (b) Water; (c) Soils; (d) Fire scar; (e) Woodlands; (f) Floodplain; (g) Color map used for the representation of abundances.

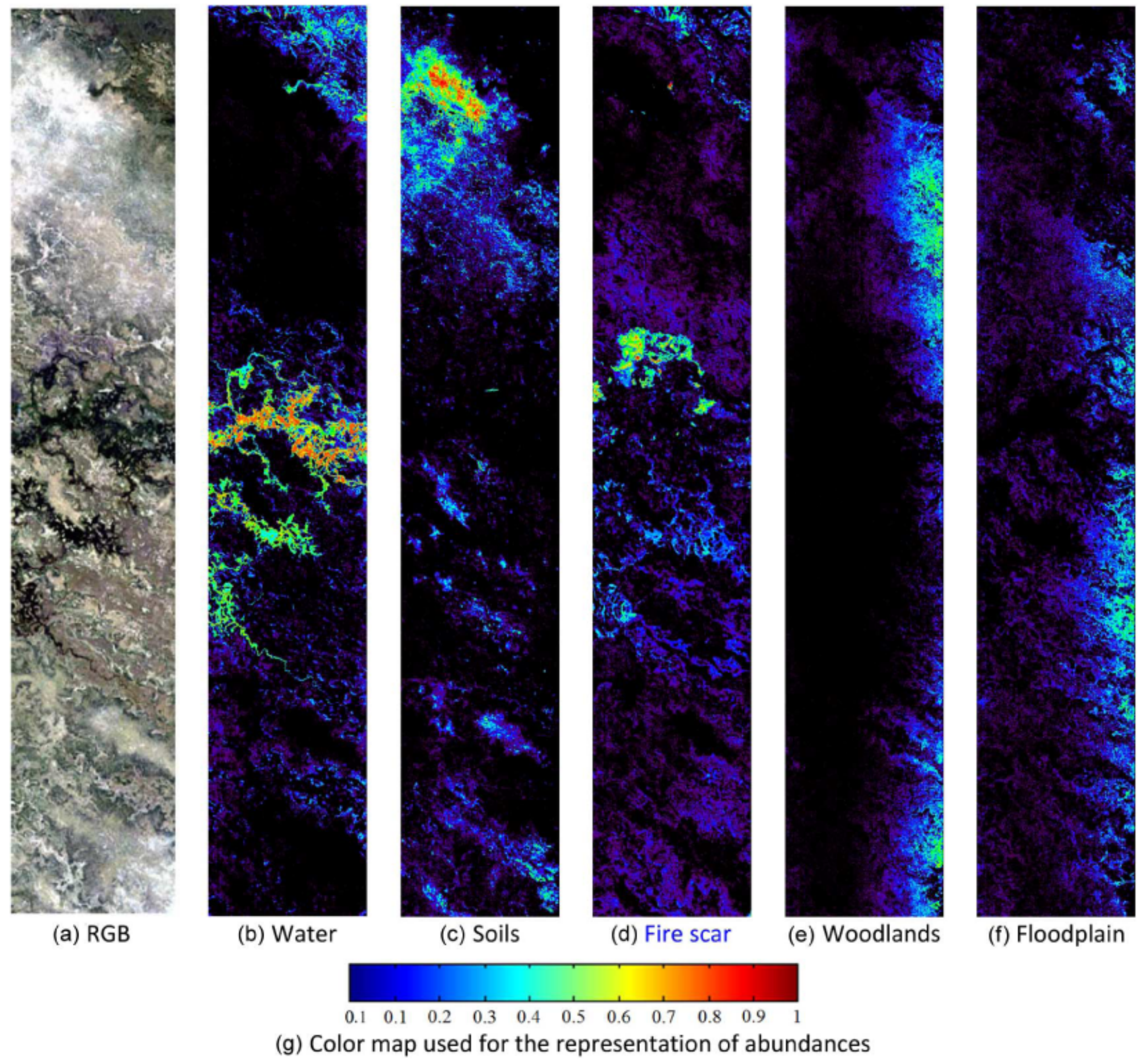

JSTARS EO-1 Special Issue

Cross-Calibration for Data Fusion of EO-1/Hyperion and Terra/ ASTER

Naoto Yokoya, Norimasa Mayumi, and Akira Iwasaki

Abstract — The data fusion of low spatial-resolution hyperspectral and high spatial-resolution multispectral images enables the production of high spatial-resolution hyperspectral data with small spectral distortion. EO-1/Hyperion is the world's first hyperspectral sensor. It was launched in 2001 and has a similar orbit to Terra/ASTER. In this work, we apply hyperspectral and multi-spectral data fusion to EO-1/Hyperion and Terra/ ASTER datasets by the preprocessing of datasets and the onboard cross-calibration of sensor characteristics. The relationship of the spectral response function is determined by convex optimization by comparing hyperspectral and multispectral images over the same spectral range. After accurate image registration, the relationship of the point spread function is obtained by estimating a matrix that acts as Gaussian blur filter between two images. Two pan-sharpening-based methods and one unmixing-based method are adopted for hyperspectral and multispectral data fusion and their properties are investigated.

Yokoya, et al. JSTARS 2013

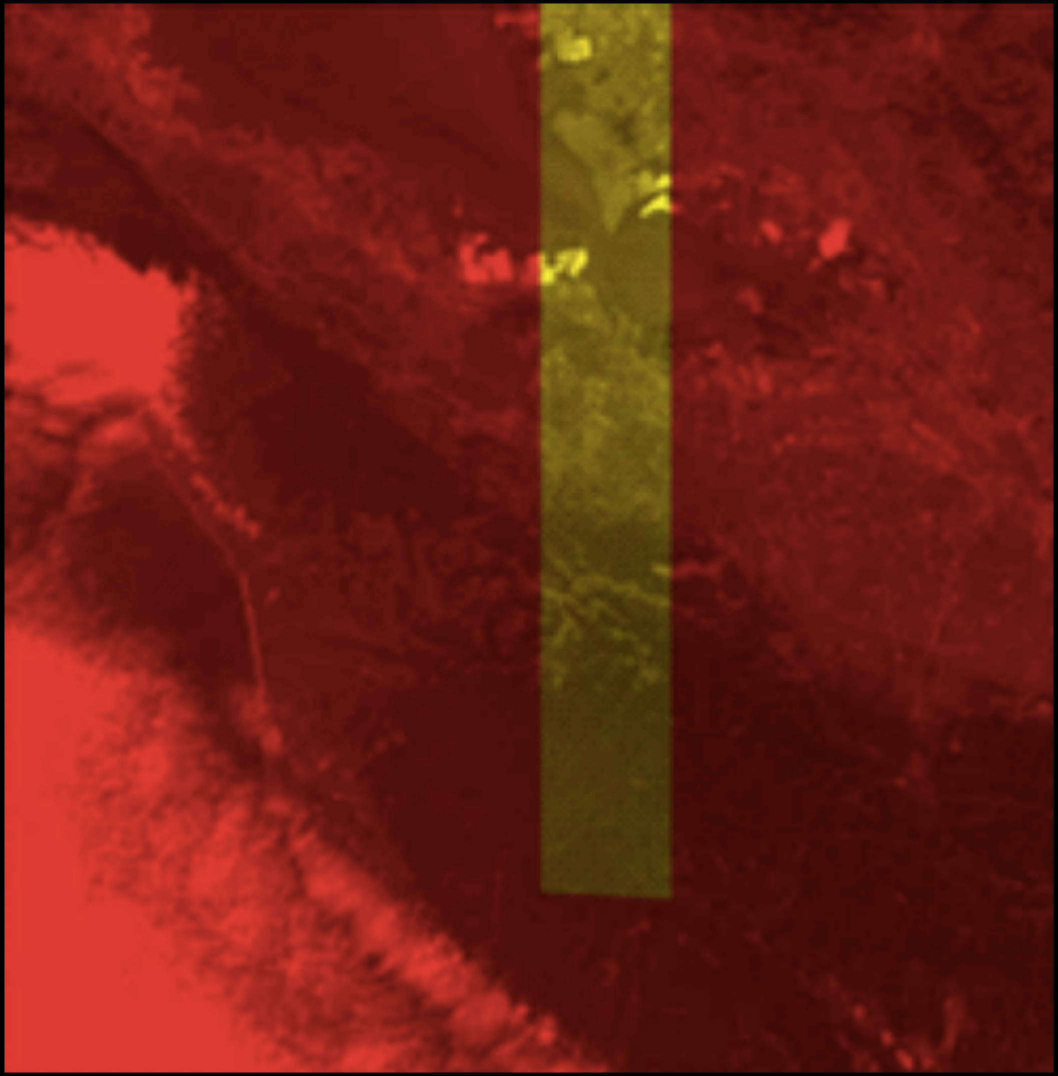

Registered Hyperion (yellow) and ASTER (red) images.

Yokoya, et al. JSTARS 2013

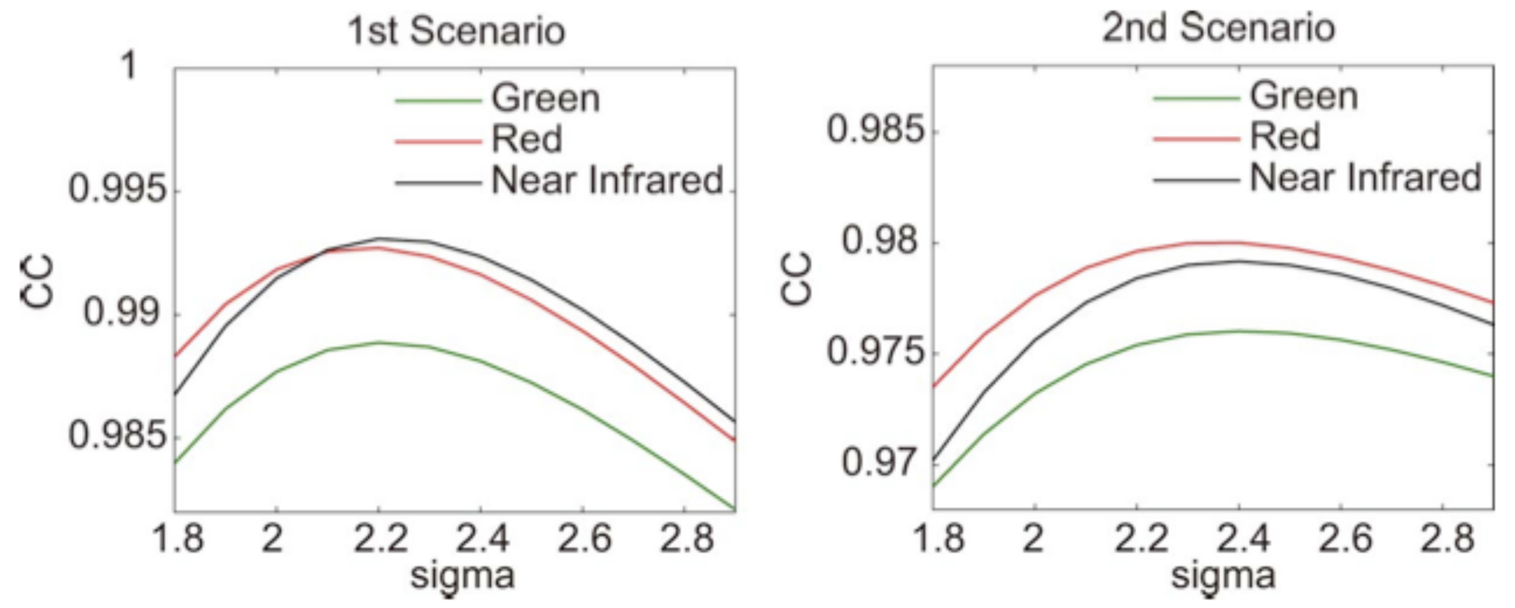

Correlation coefficient of sharpness between two low spatial-resolution multispectral images generated from Hyperion and ASTER data.

Yokoya, et al. JSTARS 2013

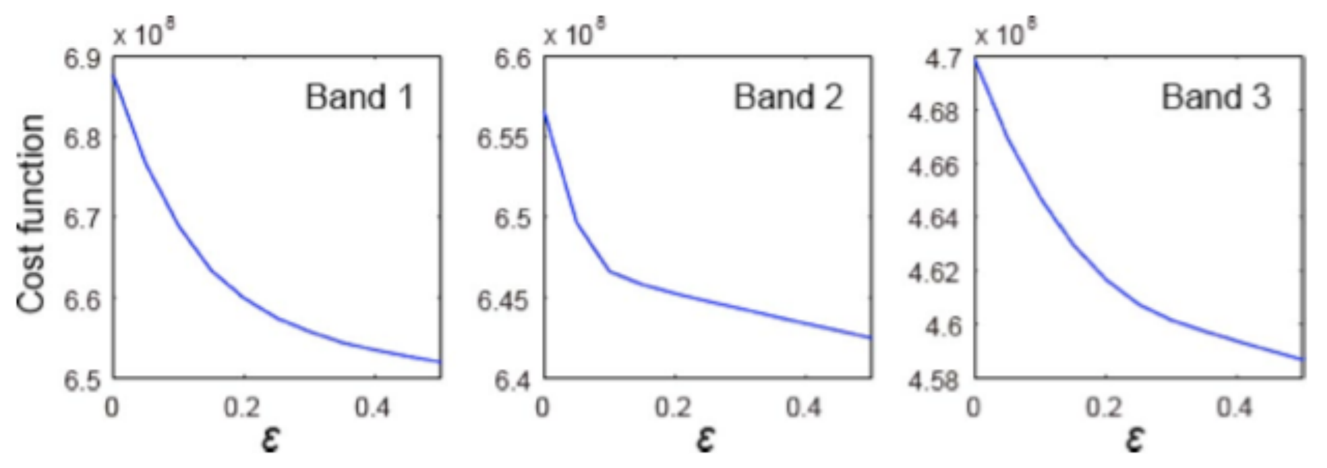

Effect of relative change in onboard spectral response transform matrix on cost function.

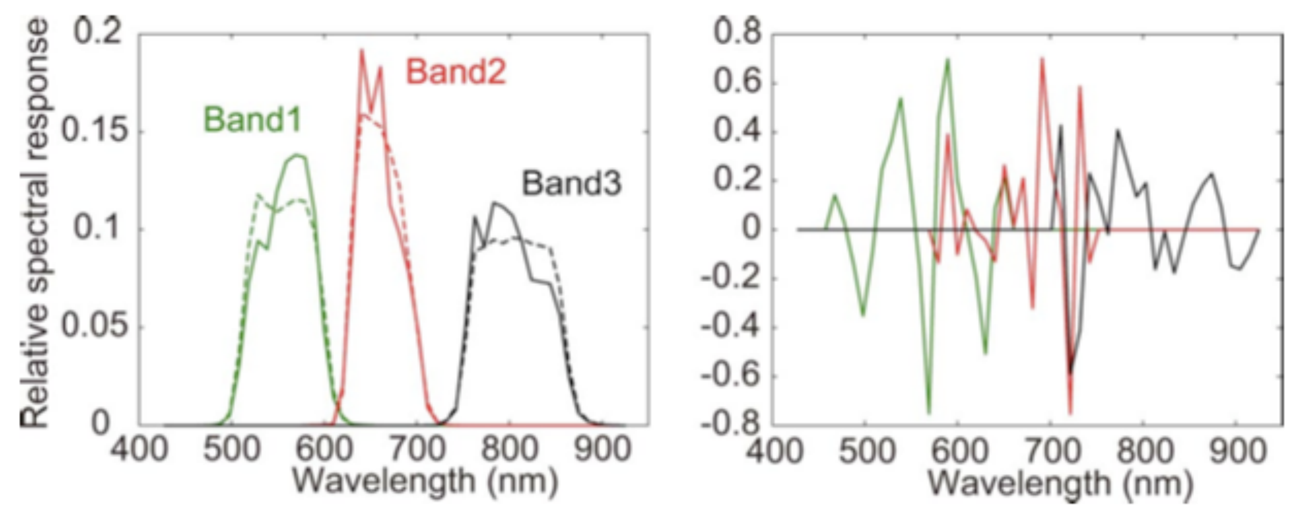

Result of estimating relative spectral response function between ASTER and Hyperion. Prelaunch (dashed line on left), convex optimization (solid line on left) and least-squares (right).

Yokoya, et al. JSTARS 2013

RGB color images of the original Hyperion (top) and CNMF fused data (bottom) using bands 13 (467.5 nm), 23 (569.3 nm), and 33 (671.0 nm) for blue, green, and red, respectively. As can be seen from the enlarged figure, the image becomes clear, meaning that roads and buildings become easier to discern.

JSTARS EO-1 Special Issue

Selection of Hyperspectral Narrowbands (HNBs) and Composition of Hyperspectral Twoband Vegetation Indices (HVIs) for Biophysical Characterization and Discrimination of Crop Types Using Field Reflectance and Hyperion/EO-1 Data

Prasad S. Thenkabail, Isabella Mariotto, Murali Krishna Gumma, Elizabeth M. Middleton, David R. Landis, and K. Fred Huemmrich

Abstract — The goal of this study was to establish optimal hyperspectral vegetation indices (HVIs) and hyperspectral narrowbands (HNBs) that best characterize, classify, model, and map the world's main agricultural crops. The primary objectives were: (1) crop biophysical modeling through HNBs and HVIs, (2) accuracy assessment of crop type discrimination using Wilks' Lambda through a discriminant model, and (3) meta-analysis to select optimal HNBs and HVIs for applications related to agriculture. The study was conducted using two EO-1 Hyperion scenes and other surface hyperspectral data for the eight leading worldwide crops from multiple study areas in various agroecosystems. Data were collected for eight crop types in six distinct growth stages. These included (a) field spectroradiometer measurements (350–2500 nm) sampled at 1-nm discrete bandwidths, and (b) field biophysical variables (e.g., biomass, leaf area index) acquired to correspond with spectroradiometer measurements. The eight crops were described and classified using 20 HNBs. The accuracy of classifying these 8 crops using HNBs was around 95%, which was 25% better than the multi-spectral results possible from Landsat-7's Enhanced Thematic Mapper+ or EO-1's Advanced Land Imager. Further, based on this research and meta-analysis involving over 100 papers, the study established 33 optimal HNBs and an equal number of specific two-band normalized difference HVIs to best model and study specific biophysical and biochemical quantities of major agricultural crops of the world. Redundant bands identified in this study will help overcome the Hughes Phenomenon in hyperspectral data for a particular application. The findings of this study will make a significant contribution to future hyperspectral missions such as NASA's HyspIRI.

Thenkabail, et al. JSTARS 2013

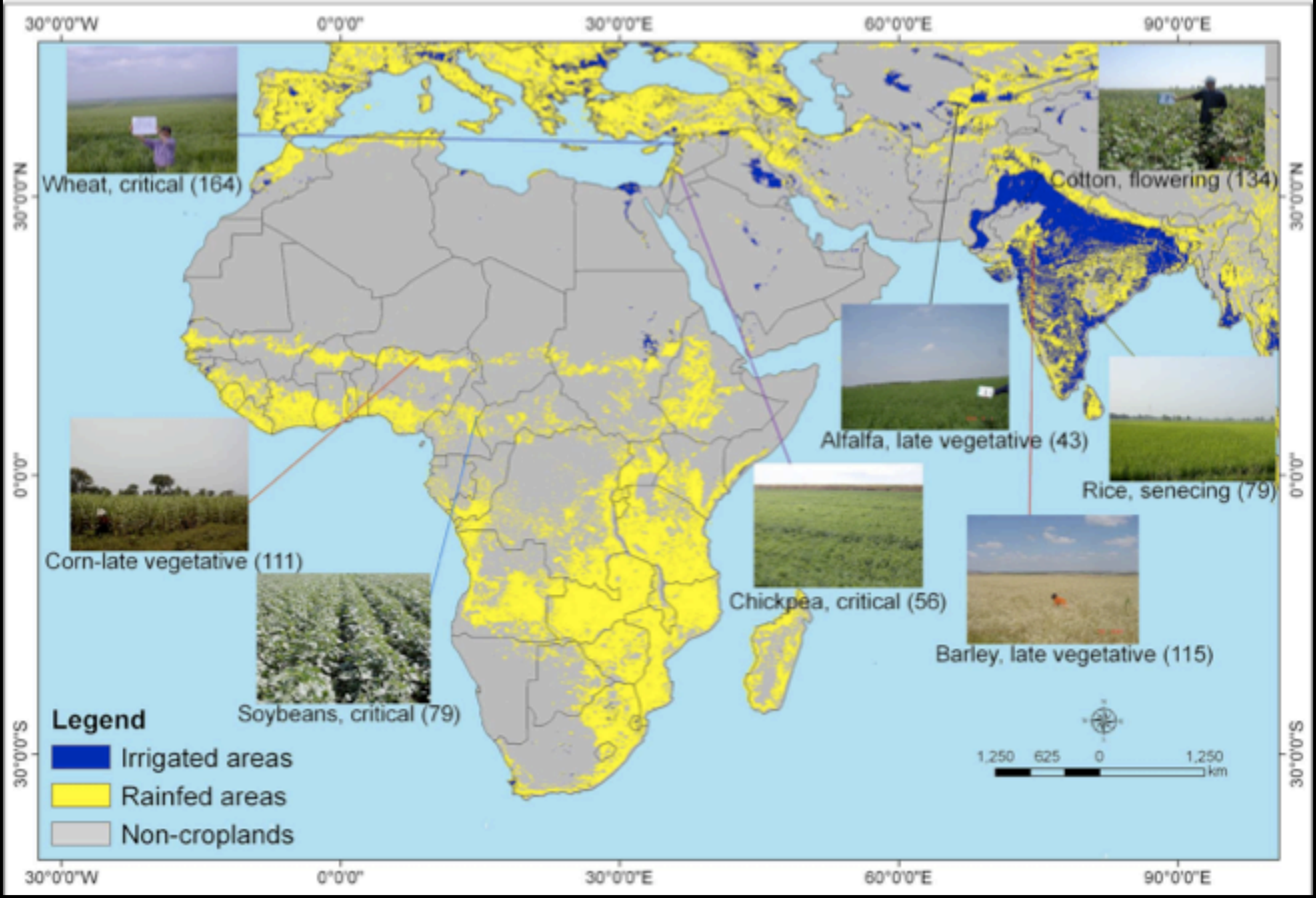

Study areas from where hyperspectral data from spectroradiometer and Hyperion were gathered. The irrigated and rainfed cropland study areas of eight major world crops in distinct agroecosystems for which hyperspectral data from spectroradiometer and Hyperion were collected from four study areas.

Thenkabail, et al. JSTARS 2013

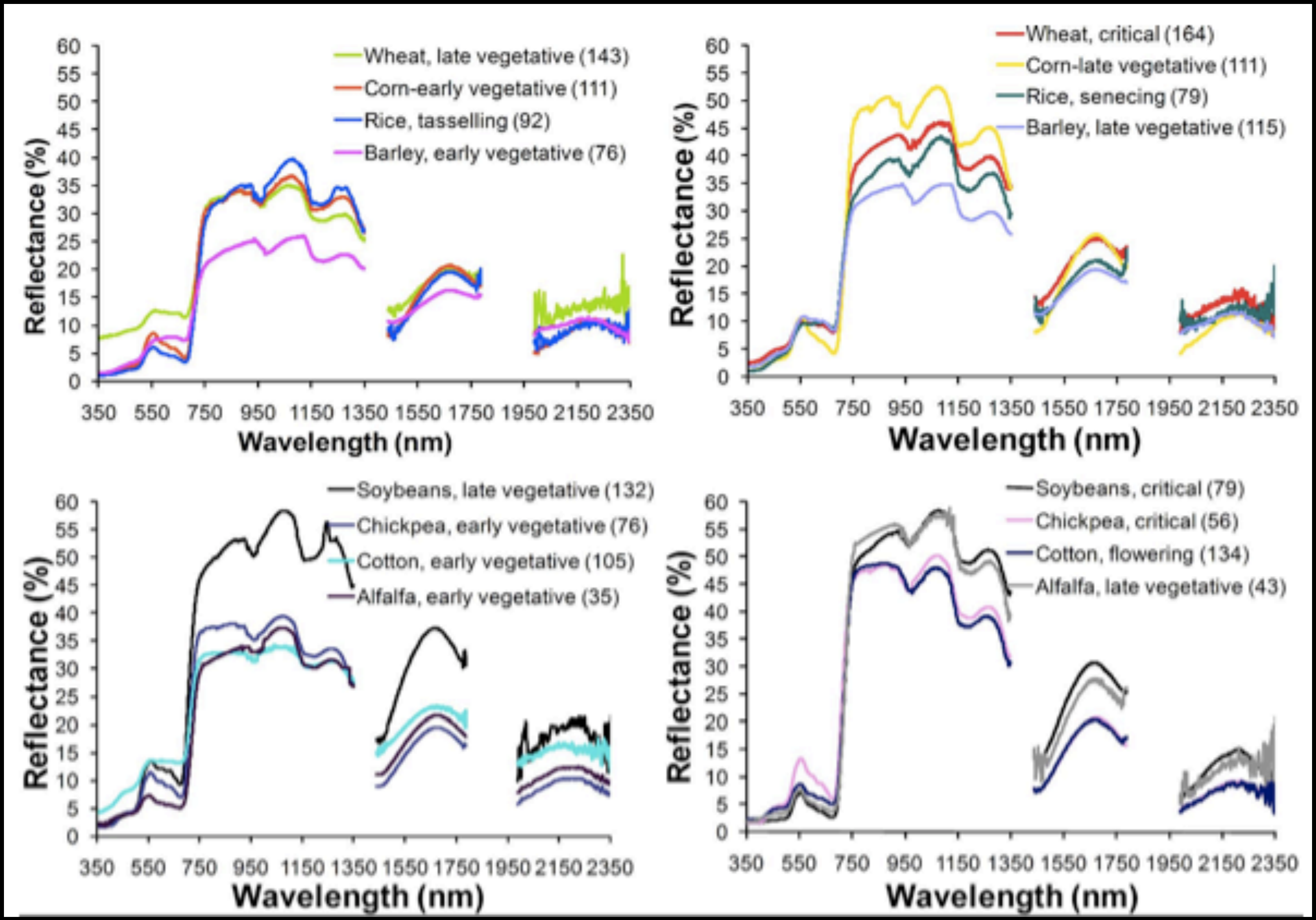

Cross-site hyperspectral spectroradiometer data. Cross-site mean (regardless of which study site) spectral plots of eight leading world crops in various growth stages. (A) Four crops at different growth stages; (B) same four crops as in A but in different growth stages; (C) four more crops at early growth stages; and (D) same four crops as C, but at different growth stages. Note: numbers in bracket are sample sizes.

Thenkabail, et al. JSTARS 2013

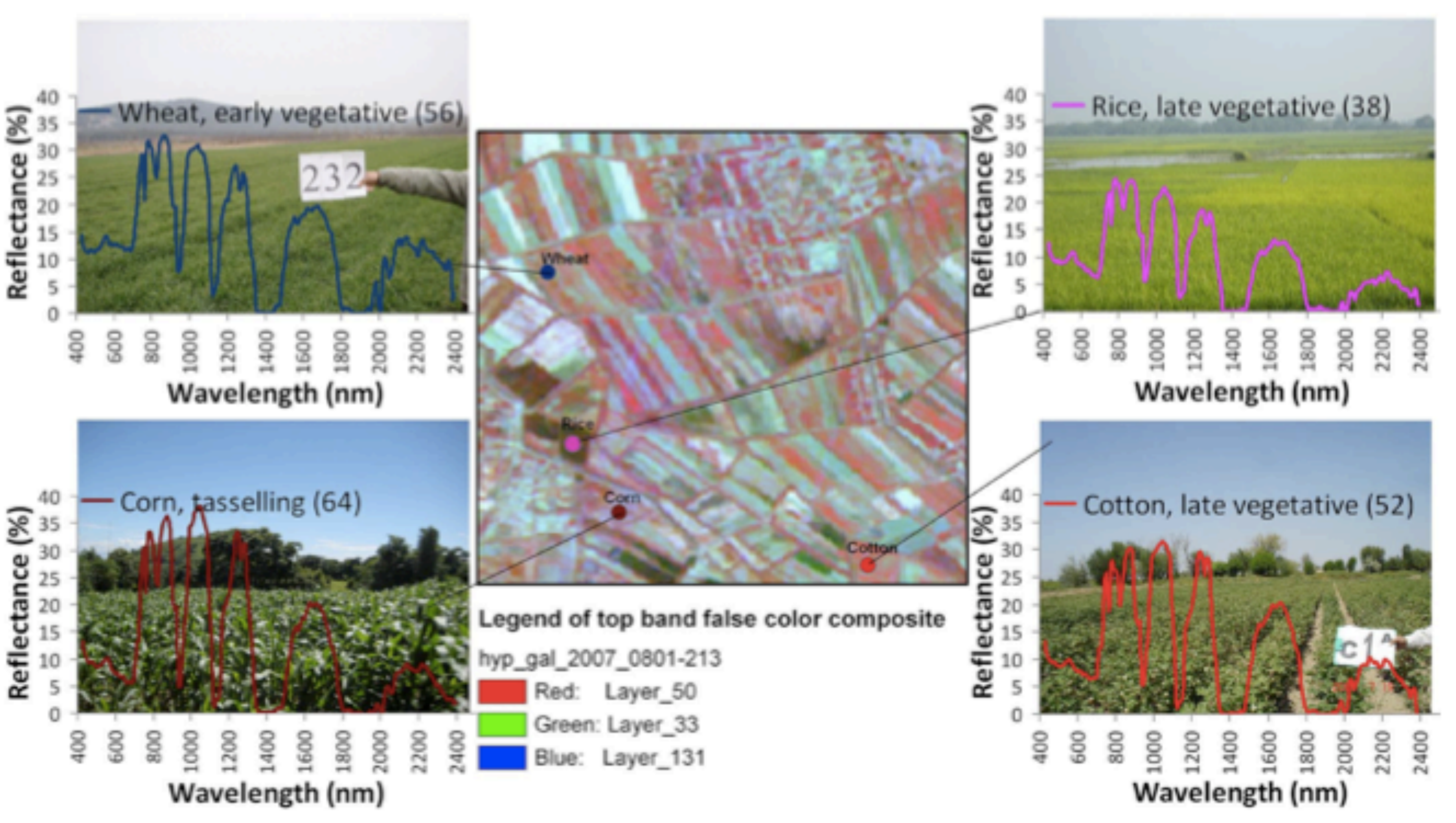

Hyperion data of crops illustrated for typical growth stages in the Uzbekistan study area. The Hyperion data cube shown here is from a small portion of one of the two Hyperion images. The Hyperion spectra of crops are gathered from different farm fields in the two images and their average spectra illustrated here along with the sample sizes indicated within the bracket. The field data was collected within two days of the image acquisition.

Thenkabail, et al. JSTARS 2013

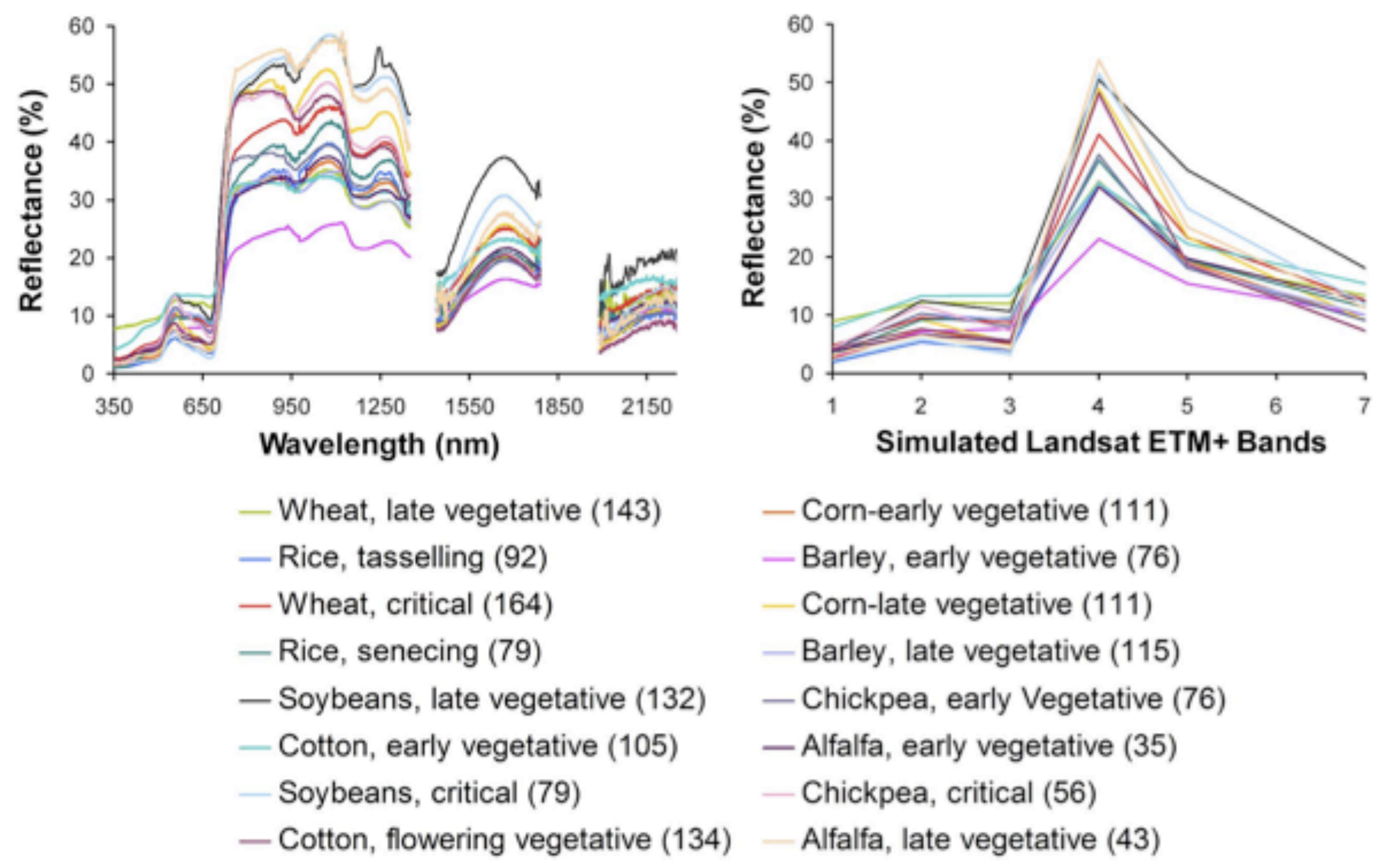

Original narrowband versus simulated broadband reflectance field spectra of leading world crops. The hyperspectral reflectance field spectra of eight leading crops, each at two distinct growth stages, are shown for narrowbands (left) and simulated for Landsat ETM+ broadbands (right). Note: sample size within brackets.

Thenkabail, et al. JSTARS 2013

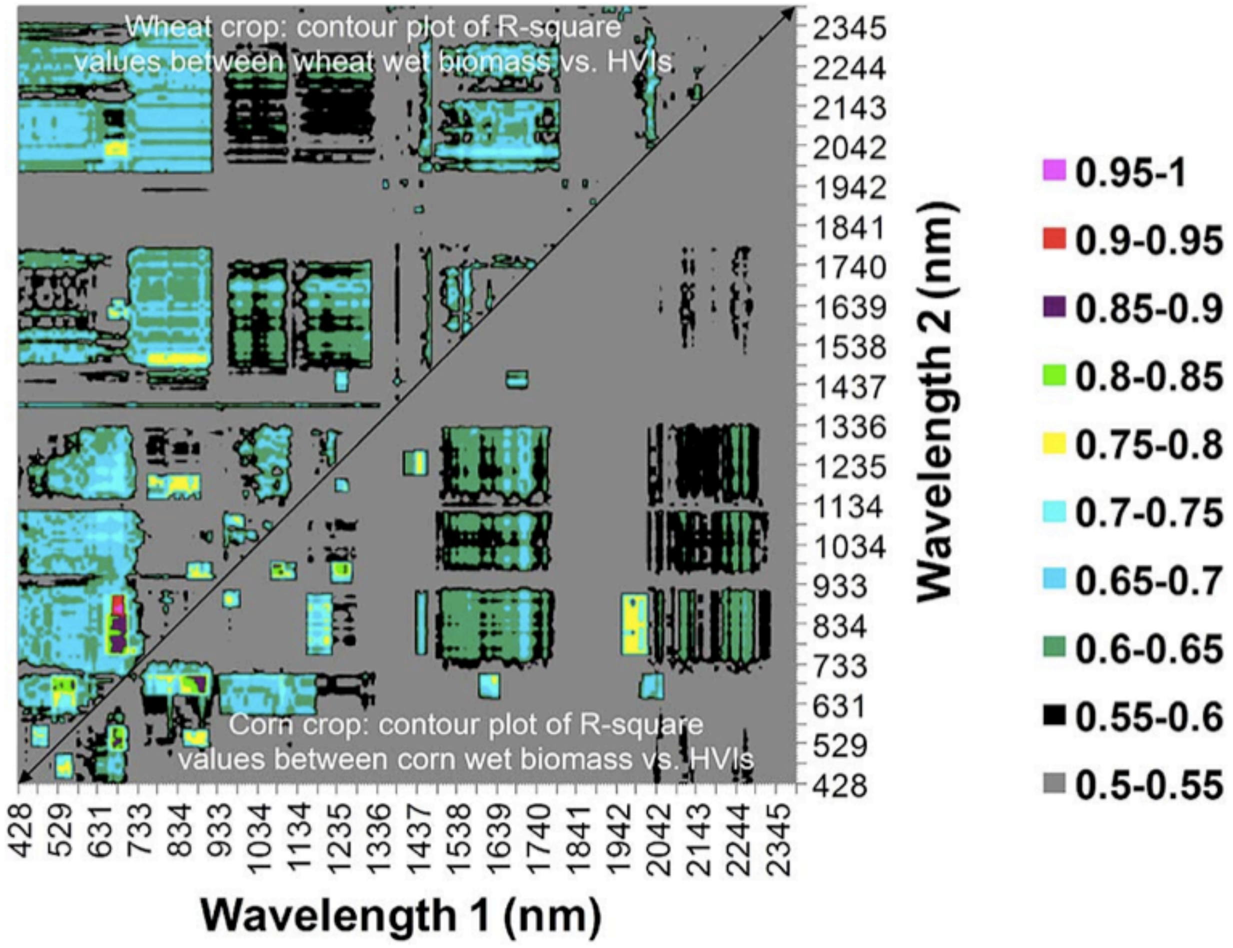

Contour plot of lambda versus lambda R^2 values for wavelength bands between two-band hyperspectral vegetation indices (HVIs) and wet biomass of wheat crop (above diagonal) and corn crop (below diagonal). The 242 Hyperion bands were reduced to 157 bands after eliminating uncalibrated bands and the bands in atmospheric window. HVIs were then computed using the 157 bands leading to 12 246 unique two-band normalized difference HVIs each of which were then related to biomass to obtain R^2 values. These R^2 values were then plotted in a lambda versus lambda R^2 contour plot as shown above.

Thenkabail, et al. JSTARS 2013

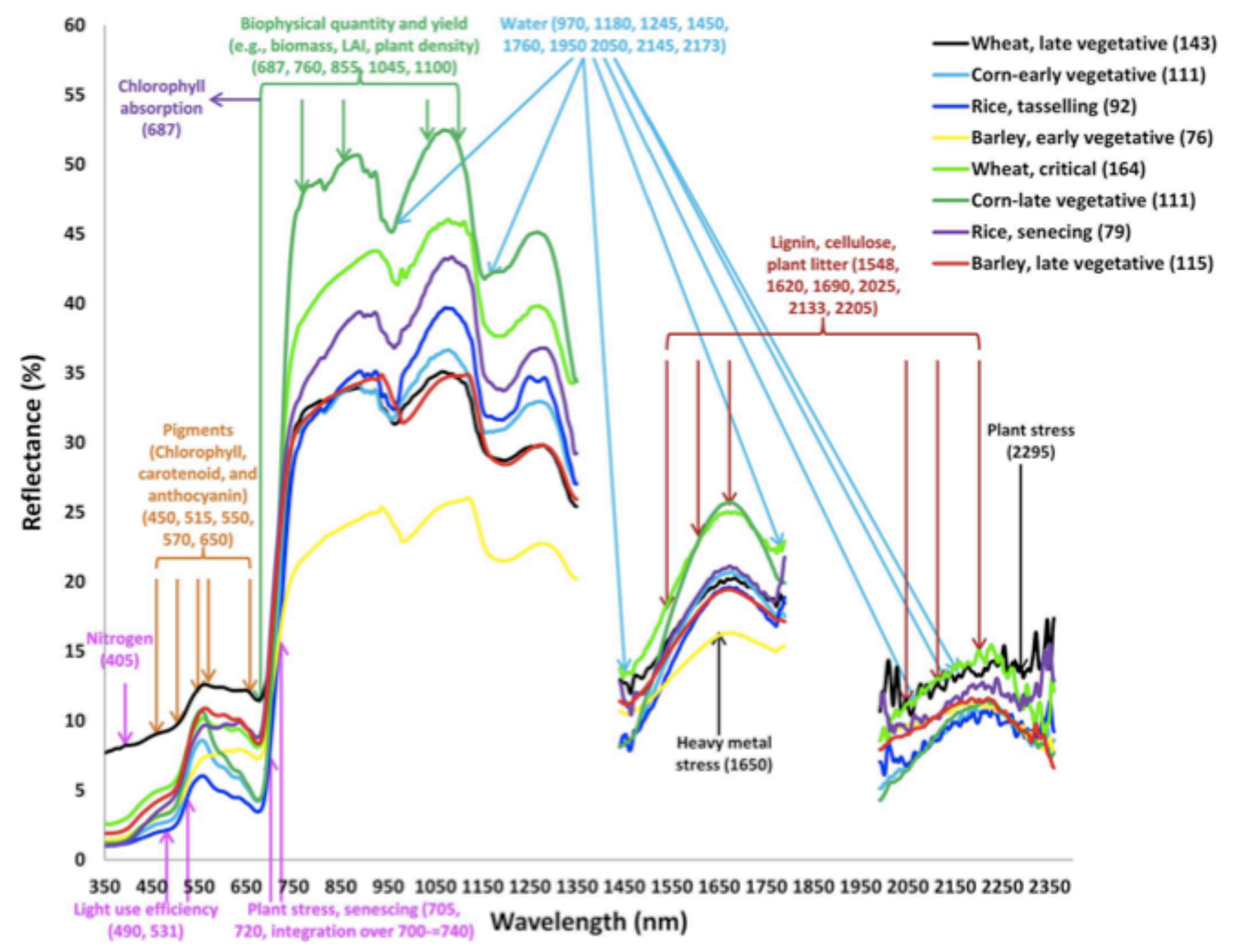

Studies on wide array of biophysical and biochemical variables, species types, crop types have established: (a) optimal HNBs band centers and band widths for vegetation/crop characterization, (b) targeted HVIs for specific modeling, mapping, and classifying species and parameters such as biomass, LAI, plant water, plant stress, nitrogen, lignin, and pigments, and (c) redundant bands, leading to overcoming the Hughes Phenomenon. These studies support hyperspectral data characterization for missions such as HyspIRI.

JSTARS EO-1 Special Issue

Crop Residue Modeling and Mapping Using Landsat, ALI, Hyperion and Airborne Remote Sensing Data

Magda S. Galloza, Melba M. Crawford and Gary C. Heathman

Abstract — Various studies have demonstrated that spectral indices derived from remotely sensed data can be used to quantify crop residue cover, if adequately calibrated using in situ data. This study evaluates the capability of the Normalized Difference Tillage Index (NDTI) derived from Advance Land Imager (ALI) relative to that of Landsat Thematic Mapper (TM) and the performance of the Cellulose Absorption Index (CAI) derived from Hyperion and airborne hyperspectral data acquired over central Indiana watersheds. A framework based on Cumulative Distribution Function (CDF) matching is also proposed to leverage the superior predictive capability of hyperspectral based indices to improve predictions of multispectral based indices over extended regions. ALI data consistently yielded crop residue models with lower root mean square error (RMSE) values than those developed using Landsat TM data. Hyperspectral based indices were generally superior in predictive capability to the NDTI based predictions. Observation operators derived from the CDF matching method were successful in scaling multiple data sets to achieve models with lower RMSE and improved predictive capability over the entire range of index values.

Galloza, et al. JSTARS 2013

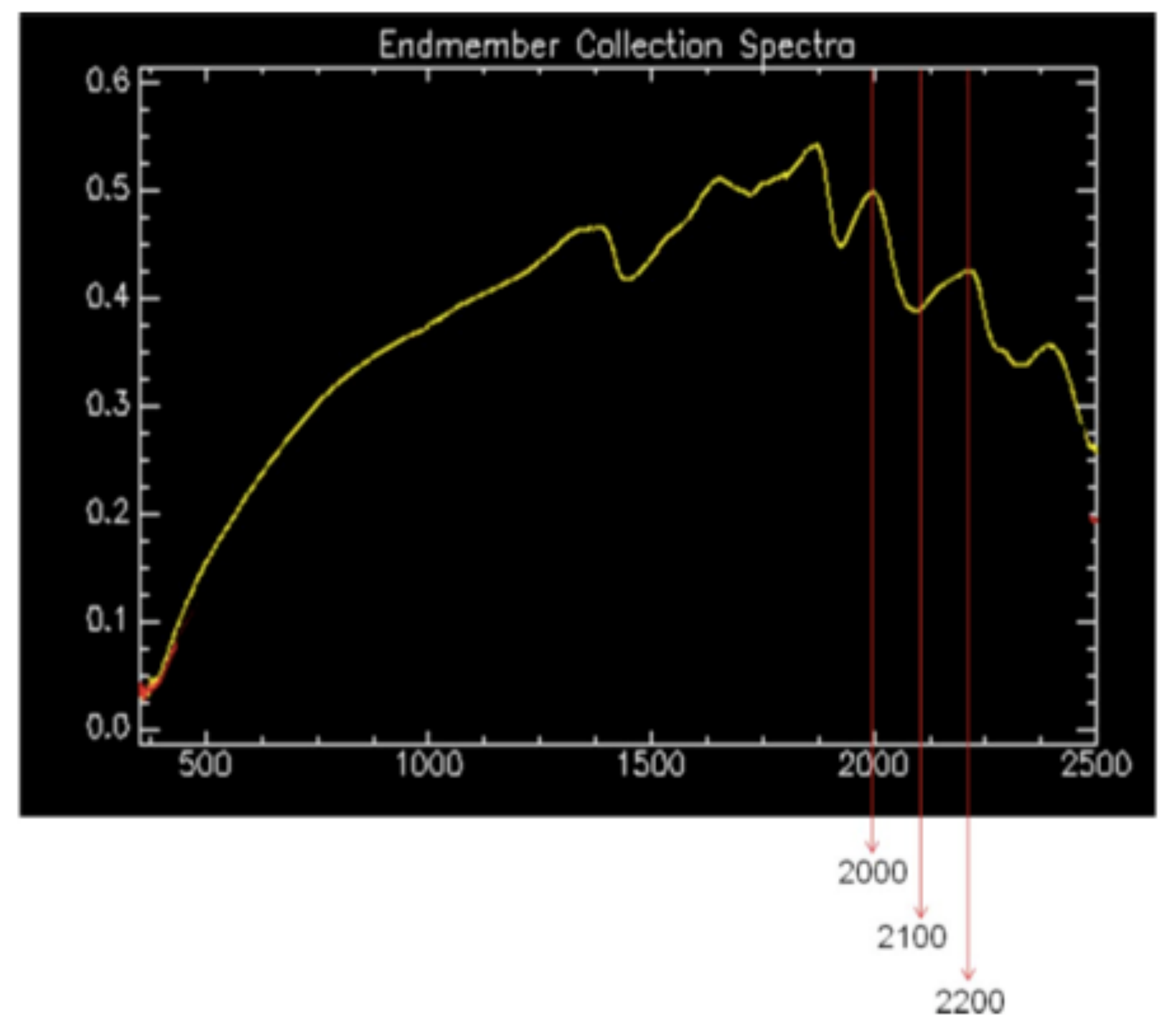

Broad absorption feature near 2100 nm associated with compounds having alcohol -OH groups.

Galloza, et al. JSTARS 2013

Data Available	Spring 2008	Fall 2008	Spring 2009	Fall 2009	Spring 2010	Fall 2010
EO-1 ALI/Hyperion	May 6	Nov 1	No Data	Oct 11	May 23	Nov 2
Landsat TM	June 11	Nov 2	May 29	Oct 20	April 22	Nov 8
SpecTIR Airborne	No Data	Nov 3	June 5	No Data	May 24	No Data

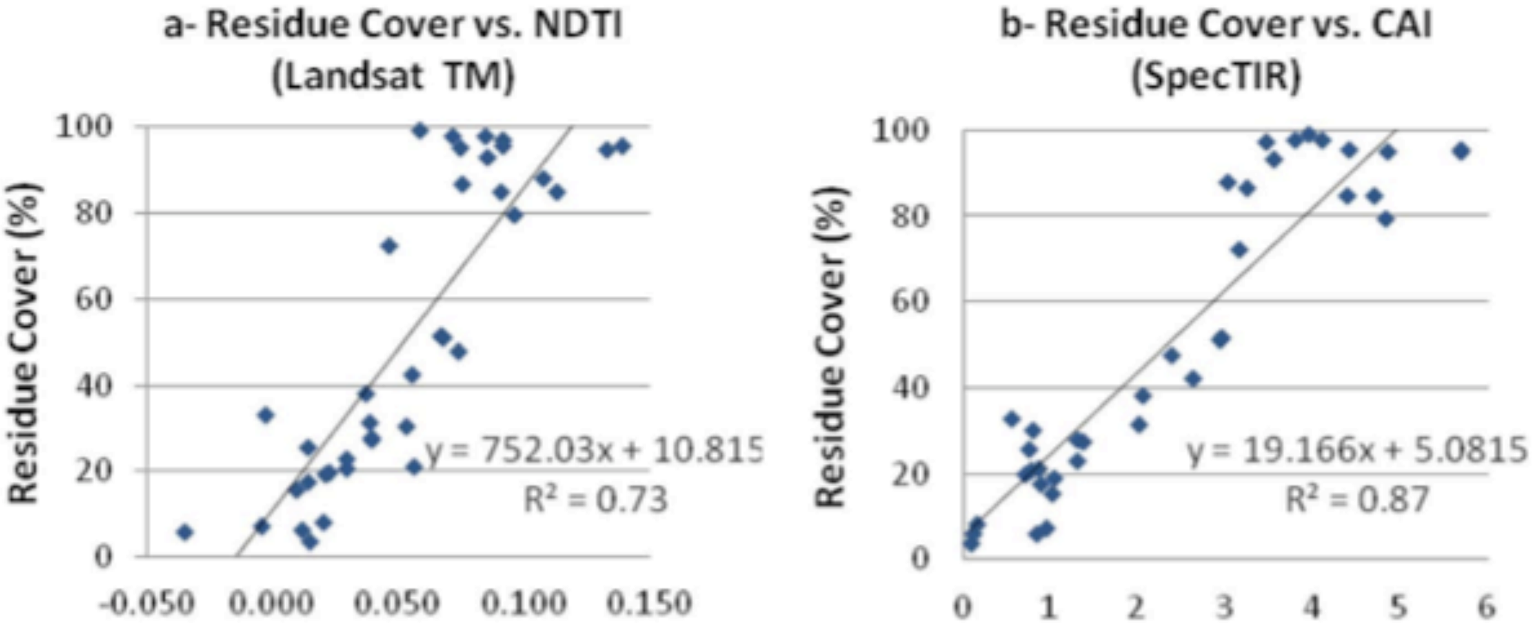

Fall 2008 a) Residue Cover vs. NDTI index (Landsat TM data) and b) Residue Cover vs. CAI (SpecTIR data).

Galloza, et al. JSTARS 2013

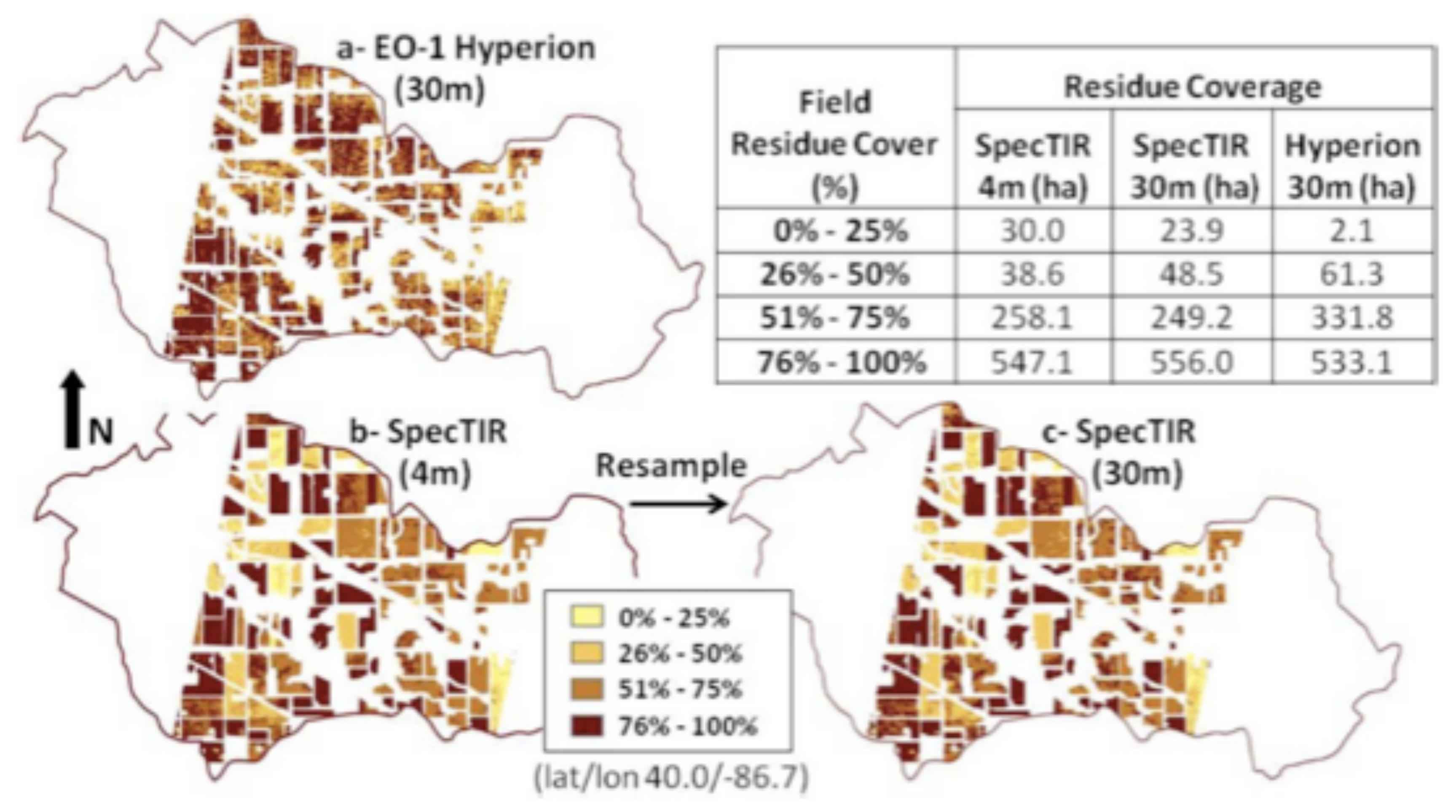

Field Residue Cover (%)	Residue Coverage		
	SpecTIR 4m (ha)	SpecTIR 30m (ha)	Hyperion 30m (ha)
0% - 25%	30.0	23.9	2.1
26% - 50%	38.6	48.5	61.3
51% - 75%	258.1	249.2	331.8
76% - 100%	547.1	556.0	533.1

Residue Cover maps (overlap region) generated in the Mace Watershed using a) Hyperion, b) SpecTIR data (4 m), and c) SpecTIR (30 m) data using the (CAI Model) -- Fall 2008.

Galloza, et al. JSTARS 2013

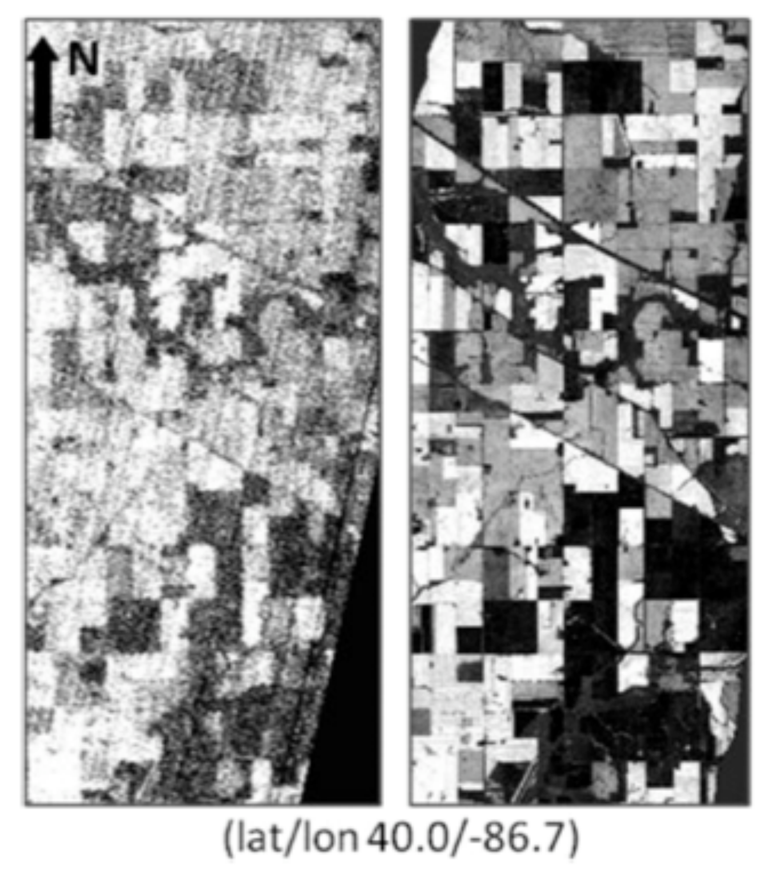

SpecTIR CAI index (Right) vs. Hyperion CAI index (Left) showing striping artifacts.

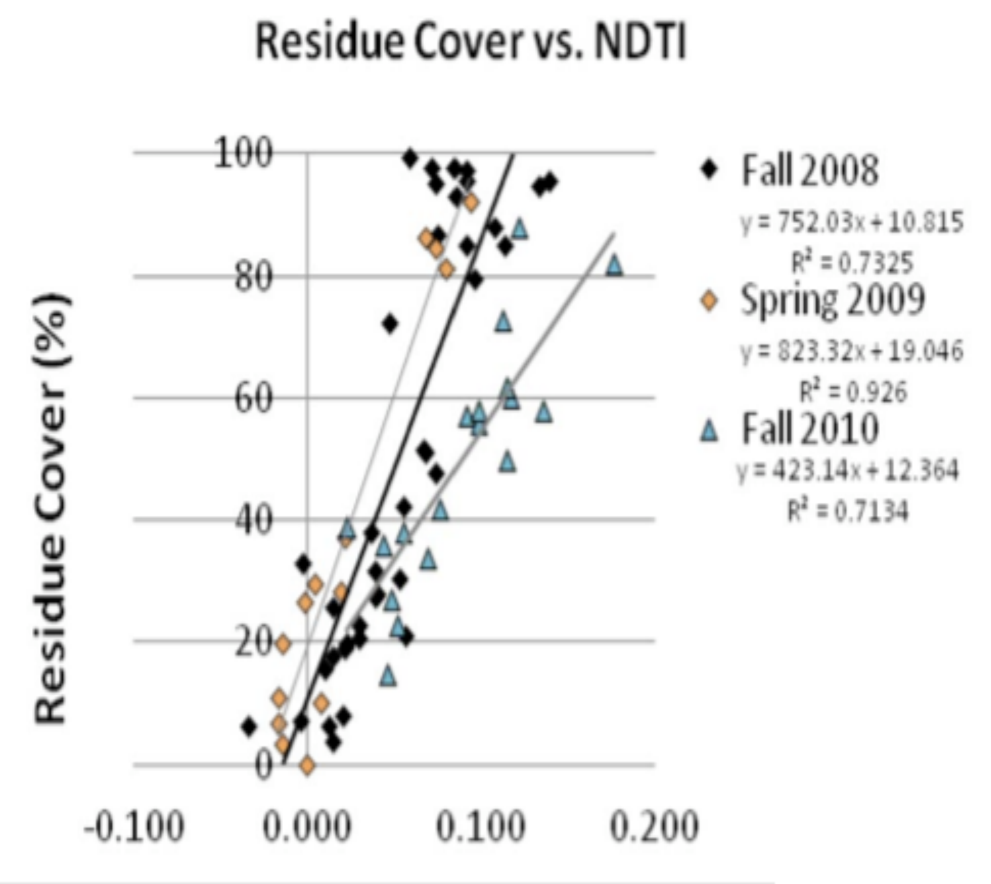

Residue cover vs. NDTI for fall 2008, spring 2009 and fall 2010 in MFOW region.